

Alma Mater Studiorum – Università di Bologna

DOTTORATO DI RICERCA IN

FISICA

Ciclo XXXI

Settore Concorsuale: 02/D1

Settore Scientifico Disciplinare: FIS/07

The FAMU experiment.
Towards the measurement of the hyperfine splitting of muonic
hydrogen.

Presentata da: Rignanese Luigi Pio

Coordinatore Dottorato

Prof.ssa Arcelli Silvia

Supervisore

Prof. Giuseppe Baldazzi

Esame finale anno 2019

The FAMU experiment

**Towards the measurement of the hyperfine splitting
of the muonic hydrogen**

Luigi Pio Rignanese

Dipartimento di fisica ed astronomia
Università di Bologna

February 2019

Voglio dedicare questo lavoro di tesi a tutte le persone che mi hanno supportato, a livello personale e professionale. In particolare la mia famiglia che non ha mai dubitato delle mie capacità. I miei amici sempre presenti e pronta valvola di sfogo. Il mio supervisore per la grande opportunità. Le persone che, qui in Italia e nella mia breve esperienza Inglese hanno contribuito professionalmente a quello che sono ora.

Grazie a Tutti.

Acknowledgements

I would like to acknowledge all the people that resolved my doubts about the multiple arguments in the following pages. In particular Emiliano Mocchiutti for the overall comments; Humberto Cabrera Morales for the interesting discussions on the laser system; Dimitar Bakalov and Andrzej Adamczak for the theoretical part; Elena Furlanetto for some precious graphs, Riccardo Travaglini and all the support of the Bologna INFN section electronics division.

Abstract

In the last few years, muon beams demonstrate that they are a powerful and reliable instrument for both applied or material science and nuclear physics. Some of the muon properties measurements, carried out by using muons beams, are central for the definition of quantum electrodynamics (QED).

The proton charge distribution radius is a nuclear physics related observable. QED calculations involve its value. It depends on the Lamb shift and hyperfine splitting which experimentally measured, are considered tests of QED, involving the Rydberg and the fine structure constant.

In 2009, at PSI, the CREMA collaboration measured the proton radius by using muonic hydrogen spectroscopy. Muon, which is ≈ 200 times heavier than the electron, orbits close to the nucleus offering a unique probe for the proton structure. They obtained a very precise measurement of the proton radius but 5% (or 7σ) smaller than the one resulting from hydrogen spectroscopy and electron-proton scattering.

This discrepancy is called "the proton radius puzzle" and is still an unanswered problem in physics. If the answer can not be found amongst the current theories, it will open a new high-precision, low energy, beyond the standard model physics.

There is another proton observable, related to both the charge and magnetic distribution, called the Zemach radius. This is dependent on QED and is strictly related to the hyperfine splitting. Different methods for measuring the Zemach radius are not in agreement and so far, a precise estimation of this observable for muonic hydrogen doesn't exist.

A first attempt was made by the CREMA collaboration measuring the hyperfine splitting of the muonic hydrogen in the 2S state. This is not the ideal condition to perform this measurement. It results in a quite big uncertainty that doesn't help to give an answer to the unsolved problem.

In this context, FAMU ("Fisica degli Atomi MUonici" that can be translated as

Muonic Atomic Physics) which is an international collaboration (Italian led) involving 25 institutions and about 60 scientists, aims to measure the hyperfine splitting of the muonic hydrogen in the ground state ($\Delta E_{\mu p}^{hfs}(1S)$), which allows a level of uncertainty better than 1%. This will result in the first precise measurement of the Zemach radius with muonic hydrogen spectroscopy. Adding an independent precise measurement of the Zemach radius in the current panorama should give a hint to the proton radius puzzle solution. Moreover, it will influence the nuclear structure theories of simple atoms and act as a precise test of QED.

The physical processes behind these measurements are related to muonic atomic physics. In particular, the ability of the muonic hydrogen to transfer its muon to nearby heavy atoms when in a gaseous mixture. The rate of this transfer process was found to be energy dependent for some elements such as oxygen.

Right after its formation, muonic hydrogen decays to its ground state. At this point, a tunable medium infra-red photon (at the right frequency ~ 0.182 eV) excites the hyperfine splitting transition ($\Delta E_{\mu p}^{hfs}(1S)$). In subsequent collisions with a H_2 molecules it de-excites back to the lowest state. In this process, the muon gains $\sim 2/3$ of the photon transmitted energy. This residual energy results in an increase in the transfer rate to oxygen.

After its formation, muonic oxygen decays to the lowest energy level by emitting characteristic X-rays. Thus, by maximizing the muonic oxygen X-rays emission, changing the laser frequency, it is possible to determine the $\Delta E_{\mu p}^{hfs}(1S)$.

In this thesis, the main mechanisms involved in the measurement are explained from the theoretical and experimental point of view. The experimental section is focused on the preparation phase performed at Rutherford Appleton Laboratory (RAL) in the UK. This first phase is devoted to the study of the muon transfer mechanism in order to fix the operative conditions for the final measurements.

A complete description of the set-up is provided by devoting particular attention on the X-rays detection system and the data analysis in which the author has been mainly involved.

The recent developments on the laser system, not used in this phase but the main core of the experiment are also presented.

Finally, the results of the first measurements of the energy dependence of the transfer rate from muonic hydrogen to oxygen are presented.

Table of contents

List of figures	viii
List of tables	xvii
I Theoretical background	1
1 The muon	2
1.1 Muon properties	2
1.2 Muon decay and lifetime	5
1.3 Muon production	6
1.4 Muon interaction with matter	10
1.5 Muonic atoms	12
1.6 Nuclear muonic capture	16
1.7 Muon transfer rate	20
2 Proton radius puzzle	24
2.1 Proton	26
2.2 The proton radius (scattering)	27
2.3 The proton radius (hydrogen spectroscopy)	30
2.3.1 Fine structure and Lamb shift	32
2.3.2 Hyperfine structure and Zemach radius	34
2.4 Scattering measurements results	37
2.5 CREMA muonic hydrogen spectroscopy	39

II	The FAMU experiment	45
3	The strategy	47
4	The apparatus	56
4.1	Muon source	58
4.2	Beam monitor	61
4.3	Cryogenic target	66
4.3.1	2014 design	67
4.3.2	2016 design	68
4.4	Laser system	72
4.5	Optical cavity	76
4.6	X-rays detection system: LaBr ₃	79
4.7	X-rays detection system: High Purity Germanium	95
4.8	Data acquisition and data handling	100
4.9	Data Analysis	105
4.9.1	On-line analysis	105
4.9.2	Off-line analysis	116
III	Results and discussion	126
5	Transfer rate to not thermalized gas mixtures: 2014 data	127
6	Transfer rate to thermalized oxygen gas mixture: 2016 data	132
7	Comparison with the models and discussion	138
	Conclusions	142
	References	143

List of figures

1.1	Lifetime of various particles [1]. On the left we can see the kaon, pion and muon lifetime. In the centre of the picture, the neutron lifetime is shown ($\approx 10^3s$) while on the far right side the stable particles are shown.	4
1.2	Feynman diagram of the μ^- decay.	4
1.3	Cross section for 50MeV π^+, π^- production in respect of the proton beam energy. The main muon source laboratories are listed [1]. . .	8
1.4	Decay muons production scheme [1].	10
1.5	Stopping power of positive muons in copper as a function of kinetic energy (top) and momentum (bottom) [2].	11
1.6	Energies of muonic X-rays. The lines are the predicted values for a point nucleus [3].	15
1.7	Feynman graph of the muon proton interaction.	17
1.8	Comparison of the reduced muon total capture rate with the Primakoff formula (1.13), and the Goulard–Primakoff extension,(1.14). The black solid squares are the experimental data from Suzuki et al [3].	19
1.9	Binding energy per nucleon from Bethe-Weizsäcker formula in the intervals $Z, N = [1, 200]$	19
1.10	Muonic X-rays time distribution for sulphur on the left and oxygen on the right. The first one shows a pure exponential decay while a more complex structure is evident in the case of oxygen [4]. . . .	21
1.11	Transfer rate from hydrogen to oxygen versus the μp energy. Three different region are present [5].	22
1.12	Transfer rate energy dependence in the 0–10 eV region [6].	22
1.13	Transfer rate from hydrogen to oxygen versus the gas target [7]. . .	23

2.1	Summary of the main measurements of the proton charge radius (R_{CH} or $\langle r_E^2 \rangle^{1/2}$). In the following pages most of the measures will be explained [8].	25
2.2	Summary of the main measurements of the proton Zemach radius (R_Z or $\langle r_{ME}^2 \rangle^{1/2}$). In the following pages most of the measures will be explained [8].	25
2.3	Feynman graph of the e-p interaction where in (a) p is point-like and in (b) it has finite dimension	28
2.4	Cross section extrapolation example	30
2.5	Summary of the fine and hyperfine splitting for the n=2 state for ordinary hydrogen and muonic hydrogen. LS stands for Lamb shift and HFS for hyperfine splitting [8].	32
2.6	Hyperfine splitting: F=0 singlet and F=1 triplet state.	34
2.7	One-loop Feynman diagram contribution to the vacuum polarization amplitude.	36
2.8	CREMA Experimental setup. The muon beam passing through thin carbon foils (S_1S_2) is frictionally cooled and enters the 1 mbar H_2 target. The electrons generated are drifted by ExB and then read by 3 photomultiplier. The emitted X-rays are detected by 20 Large-Area Picosecond Photodetectors (LAPDDs not shown here) [9]	39
2.9	Atomic levels scheme involved in the CREMA experiment. In a, right after the muonic hydrogen formation, the muon decays from n=14 to n=1 but with 1% of probability it can get stuck in the 2S state where the decay to the 1S is prohibited. In b a tuned laser source excites the muons in the 2S state to the 2P. Now the decay is possible emitting 2 keV X-rays [9].	41
2.10	Time evolution of the 2 keV X-rays emitted by the hydrogen target. The prompt phase (in blue) coincides with the muons arrival thus the muonic hydrogen formation. In a the laser was shot but not in b. It is clear that the laser excited the right resonance (2S-2P transition) [9].	42

2.11	Ratio of the delayed X-rays (by the laser excitation) over prompt ones (due to the muonic hydrogen formation) versus the emitted laser frequency. For comparison, the charge radius from CODATA and e-p scattering was used to calculate the Lamb shift and inserted in the graph [9].	43
2.12	Proton charge radius from different sources. The CODATA 2014 value takes into account e-p scattering, hydrogen and deuterium spectroscopy but doesn't consider the muonic results [10].	43
3.1	FAMU experimental strategy scheme [11].	49
3.2	Time evolution of the μp average energy at fixed density and different temperatures [12].	51
3.3	Average μp energy versus time at different pressures [12].	51
3.4	Time evolution of the $\mu p^{F=1}$ population over time at different pressures but fixed temperature [12].	52
3.5	Time evolution of the μp population, after the thermalization ends, over time at different oxygen concentration but fixed temperature and pressure [12].	53
4.1	ISIS neutron and muon source schematic. The synchrotron accelerated protons are split in 2 target station (TS). In TS1 are hosted the muon beamlines, a particular of these beamlines is shown in the enlarged red circle [13].	58
4.2	The four ports scheme of the RIKEN-RAL muon facility. Each muon production and delivery element position is indicated	59
4.3	RIKEN-RAL muon beam time distribution	60
4.4	Predicted intensities for positive and negative muons both from the decay channel and surface (only for μ^+). It worth nothing to notice the increase in number of muons in respect of the chosen momentum [14].	60
4.5	Port 4 and Port 1 magnetic field profiles obtained with the TURTLE beam simulation software. The magnets names are on the top while the set currents are on the bottom of each figure.	62
4.6	Reverse current-voltage characteristics of the 64 SiPMs mounted on the hodoscope. The response is quite similar [15]	63

4.7	Hodoscope mounting [15]	63
4.8	Digitized hodoscope waveform of single fibre, the integration threshold is shown in red [15].	64
4.9	Measured muon flux of the RIKEN-RAL muon beam at port 1. The filled boxes are calculated using the equation 4.1 and are in good agreement with the expected flux Fig. 4.4 [16].	65
4.10	Hodoscope 2D map of the integrated charge. The Q11 magnet position is shown in Fig. 4.5. One fibre defect is clearly visible. . .	66
4.11	FAMU GEANT4 simulation of the muon distribution stopped into the gas at 57 MeV/c. The different lines represent different CO ₂ concentration in hydrogen target [17].	67
4.12	2014 target design with all the dimensions in mm. On top the gas feeding system is shown as well.	68
4.13	2016 Target 3D model and details of the entrance window design [18].	69
4.14	2016 internal target particulars.	69
4.15	FAMU GEANT4 simulation of the muons stopped fraction into the different volume of the target: green line for the tested gas, black for the aluminium walls, cyan for the lead collimator, yellow and pink for respectively the gold and nickel coatings and red for other materials. At 57 MeV/c the number of muons stopped into the gas is maximized. [18].	70
4.16	FAMU simulation of the muon distribution stopped into the gas at 57 MeV/c. Top panel: ZX projection. Middle panel: ZY projection. Bottom panel: muons stop distribution along Z axis [18].	71
4.17	FAMU2016 temperature cycle for the H ₂ O ₂ (0.3%) gas mixture. In blue, the cold head temperature, in green the target one and in magenta the percentage power of the heater [18].	73
4.18	FAMU DFG based laser system. Where WP - waveplate, PO - polarizer, M1–M5 - mirrors, T1 and T2 - telescopes, BS - beamsplitter, DC1 - dichroic mirror (1.26 μ m reflected and 1.06 μ m transmitted), DC2 - dichroic mirror (1.06 μ m and 1.26 μ m reflected and 6.76 μ m transmitted) [19].	74

4.19 Cr:forsterite oscillator scheme. Where 1 - decreasing telescope, 2 - entrance mirror (1.26 μm reflected and 1.06 μm transmitted), 3 - Cr:forsterite crystal, 4 - prism, 5 - diffraction grating, 6 and 7 - tuning mirrors of coupled resonator [19].	75
4.20 4 meters humid air absorption versus the wavenumber at 300 K, 1 atm and 60% umidity. The hyperfine splitting expected energy is at $\approx 1473.8 \text{ cm}^{-1}$	76
4.21 Schematic view of a longitudinal optical cavity.	78
4.22 Schematic view of a transversal optical cavity.	78
4.23 Signal to noise ratio enhancement versus time for various inter-mirrors distances d	80
4.24 LaBr ₃ light emission. Three cerium dopant concentration are shown [20].	82
4.25 Absorption versus incident photon energy for different crystal thickness [21].	82
4.26 ¹³⁸ La decay scheme[22].	83
4.27 Photon nonproportional response of LaBr ₃ (Ce) as a function of X-ray energy (EX) curve at (1) 80 K, (2) 295 K, and (3) 450 K [23].	84
4.28 LaBr ₃ old design matrix [17].	85
4.29	86
4.30 PMT cathode quantum efficiency for bialkali, super bialkali and ultra bialkali photocathode [24].	87
4.31 Ratio of output voltagr to voltage divider current over incident light level. Three region are present: A linear, B non linear, C saturation [25].	87
4.32 Left: linear voltage divider. Right: tapered voltage divider, the voltage drop across the last dynodes is increased by increasing the resistance value [25]	88
4.33 Deviation from linearity versus the anode output current (proportional to the incident light) for a linear and a tapered voltage divider. The linear region is increased by the second divider style [25]. . .	89
4.34 Active voltage divider used in the 2016 detector version [18]. . . .	90

4.35	Left panel: disassembled detector: the circular LaBr ₃ :Ce crystal and the squared PMT are visible. Right panel: assembled detector with part of the electronic visible, in particular the active voltage divider MOSFETs. [18].	91
4.36	Five assembled FAMU LaBr ₃ custom detectors and a commercial one during the test phase before the integration. The three cable connections are visible at the bottom end of the aluminium profile.	92
4.37	3D CAD of the LaBr ₃ star shaped detectors array fitted around the gas target [18].	93
4.38	Top: particular of the shifted half stars shape detector array around the gas target. Bottom: detectors positioning and muons stop simulation [18].	93
4.39	¹³⁷ Cs peak as acquired at the anode level and after the 125 MHz active filter.	94
4.40	ORTEC coaxial HpGe detector efficiency curve as function of the X-ray photon energy.	96
4.41	Scheme of a continuous reset pre-amplifier with a $R_f C_F$ feedback network.	97
4.42	Typical output of a transistor reset pre-amplifier (TRP). When the signal reaches 4 V, the transistor injects the output in the amplifier resulting in a fast return to the baseline.	97
4.43	On beam spectrum with GEM-S HpGe detector shaped with an Ortec 672 with 2 μ s of shaping time.	99
4.44	On beam spectrum with GEM-S HpGe detector without any shaping. The pre-amplifier signal was used.	99
4.45	Noise in the GEM-S fast amplified baseline signal [26].	100
4.46	Proposed DAQ upgrade schematic design.	103
4.47	Left panel. SNR of the single ADC and of the interleaved system. ADS45j60 is shown as reference. Right panel. THD of the single ADC and of the interleaved system. ADS45j60 is shown as reference [27].	104
4.48	Example of LaBr ₃ waveform and the derivation made by the "quick-look" software [18].	106

4.49	Example of a single LaBr ₃ detector waveform time evolution as shown in the FAMU quicklook web page. Each box reproduce the cumulated energy spectrum for different successive time cut. In the bottom left, a false colours 2D map of the time spectra in X (the double pulse muon beam time shape is clearly visible) and energy one in Y.	107
4.50	Shaping parameters useful in the ENC calculation (equation 4.17) [28].	110
4.51	Desired trapezoidal shaping output. It is a composition of four linear pulses $f_{A,B,C,D}(t)$. The time length of these pulses defines the shaping parameters R rise time and M flat top duration [29].	111
4.52	Schematic view of the shaping algorithm blocks [29].	112
4.53	(Left panel. ⁵⁷ Co 122 keV peak resolution using the peak height (raw) and by using a 100 ns digital triangular filter. Right panel. ¹³⁷ Cs 662 keV peak resolution using the peak height (raw) and by using a 100 ns digital triangular filter.	113
4.54	Typical on-beam LaBr ₃ waveform.	118
4.55	Single pulse and piled-up pulses and the relative fit (red line). The pile up is successfully disentangled (blue dotted dash) [18].	119
4.56	Time spectrum of X-rays detected by LaBr ₃ detector. Three zone can be identified: in the black box, the pre trigger with no counts. In the red box, the prompt zone where the beam interacts with the target and the beam time distribution appears evident. In the green box, the delayd phase [18].	119
4.57	Top panel: Time spectra of detected X-rays by LaBr ₃ detector. Bottom panel: percentage of single pulses (single X-ray photon) versus time. [30].	120
4.58	In blue the efficiency curve versus time of LaBr ₃ detectors due to saturate events only. In black, the resulting efficiency after imposing $\bar{\chi}^2 < 100$ of the peaks fit. In red the total efficiency, the reader can notice that in the thermalized phase (above 1200 ns) it remain stable [30].	121
4.59	Efficiency versus time for fast shaped HpGe detector. During the prompt phase, the efficiency drop down to 20% [26].	122

4.60	Total spectrum, without time cut. All the prompt muonic lines due to the interaction between muons and the aluminium, nickel coated target vessel are visible.	123
4.61	Total delayed spectrum of muonic oxygen. The muonic oxygen k_α , k_β and k_γ (cluster together) appear well distinguished from the background.	123
4.62	In black a delayed spectrum of muonic oxygen X-rays. In green the pure hydrogen spectrum smoothed with a Gaussian kernel in red. This last one is considered background and is subtracted to the oxygen spectrum.	124
4.63	Energy spectrum of three different delayed time bins. The results of the background subtraction shows the muonic X-ray lines and a small structure at low energy, probably due to nuclear capture processes.	125
5.1	2014 data taking, LaBr ₃ mosaic H ₂ +CO ₂ (4%) spectrum.	128
5.2	2014 data taking, LaBr ₃ mosaic H ₂ +Ar(2%) spectrum [17].	128
5.3	Time distribution of aluminium and oxygen (on the left) or argon (on the right). A difference of $\approx 5-10$ ns is visible [31].	129
5.4	Transfer rate measurement results in a non thermalized gas mixture, relative, from top to bottom, to CO ₂ , O ₂ and Ar. The shaded region reflects the systematic uncertainties while the long horizontal error bar reflect the unknown μp energy distribution. Comparison with data [5] and models [6], [32] in literature [31].	131
6.1	Time dependence of the oxygen signal at 300 K (green) and 100 K (blue). The points represent the counts at each time bin below the k_α and $k_\beta+k_\gamma$ clustered peaks. The solid lines are the respective fit to the data following equation 3.7. In the inset, a zoom in logarithmic scale [30].	133
6.2	Transfer rate measurement versus temperature obtained with LaBr ₃ detectors and 0.3% oxygen concentration. The shaded region represents the systematic uncertainty. Empty small triangle is the measure from [33].	135

-
- 6.3 Transfer rate measurement versus temperature obtained with LaBr_3 detectors and 0.3% oxygen concentration (red dots). The shaded region represents the systematic uncertainty. Empty small triangle is the measure from [33]. 135
- 6.4 Transfer rate measurement versus temperature obtained with LaBr_3 detectors and 0.05% oxygen concentration (black dots). The red dots are from the 0.3% concentration gas mixture and the shaded region represents the systematic uncertainty of this last results. Empty small triangle is the measure from [33]. 136
- 6.5 Black solid line shows the delayed energy spectrum obtained with LaBr_3 detectors with an oxygen concentration of 0.3%. In green, the delayed spectrum with an oxygen concentration of 0.05%. . . 136
- 6.6 Transfer rate measurement versus temperature obtained with fast amplified GEM-S Hphe detector and 0.3% oxygen concentration (black dots). The red dots are from LaBr_3 and the shaded region represents the systematic uncertainty of this last results. Empty small triangle is the measure from [33]. 137
- 7.1 Transfer rate versus temperature. Our results are in red while the only other measurement is from [33] in the empty triangle. The two models [6] and [32] present in literature are shown as well [34]. 139
- 7.2 Transfer rate versus energy. The parabola fitting of our results is shown in red while the dashed and dotted lines are respectively from [6] and [32] [34]. 140

List of tables

1.1	Muon properties.	3
1.2	Energies of muonic X-rays in a few elements, for heavy elements the $2p_{3/2} - 1s$ and the $2p_{1/2} - 1s$ transitions are listed [3].	16
2.1	Value and uncertainty of the ΔE_{th}^{hfs} contributions [35].	36
4.1	Characteristic muonic X-ray lines detected by the GEM-S HpGe during the 2016 data taking.	99
4.2	Summary of the DAQ modules characteristics [36].	101
5.1	Values needed to compute the transfer rate. They come from multiple references such as [37] and [38], and [39]. For the deuterium concentration, we measured in laboratory the tested gas.	130
6.1	Summary of the 2016 data taking measurements at RIKEN-RAL (RB852).	132

Part I

Theoretical background

Chapter 1

The muon

This first chapter is focused on the muon and its main characteristics. The first paragraphs will focus on the uniqueness of this particle as a test for the quantum electrodynamics (QED). Later, this chapter will provide all the basic principles, related to the negative muon physics, needed to understand the processes taking place in the FAMU experiment.

1.1 Muon properties

The muon, which symbol is μ^- , is an elementary particle and it is classified as a lepton. It has an electric charge of $-1e$, a spin of $1/2$ and a mass of $105.7MeV/c^2$. It has the same electric and spin characteristics of the electron but its mass is about 207 times bigger.

The muon has a corresponding antiparticle with the same spin and mass but opposite electric charge ($+1e$), this is called anti-muon or positive muon (μ^+).

Due to its mass, the muon is an unstable elementary particle with a mean life time of $2.2\mu s$. Muon decay is slow (compared to other subatomic particles) and, after the neutron (among unstable particles) has the longest life time (Fig. 1.1). Negative and positive muons decay via the weak interaction (Fig. 1.2). Charge and leptonic family numbers have to be conserved so, the decay products must involve a couple of neutrinos (electron and muon one) and a charged particle. The dominant muon decay mode is the simplest possible where a μ^- decays to an electron, an electron anti-neutrino and a muon neutrino. Anti-muon decays into a positron, an electron

neutrino and a muon anti-neutrino. In formulae:

$$\mu^- \rightarrow e^- + \bar{\nu}_e + \nu_\mu,$$

$$\mu^+ \rightarrow e^+ + \nu_e + \bar{\nu}_\mu.$$

The decay $\mu \rightarrow e\gamma$ violates the lepton flavour conservation and led Bruno "Pontecorvo and others to postulate the existence of two distinct neutrino types; an electron-flavoured neutrino and a muon-flavoured neutrino" [40]. The research of this violation is one of the central subjects in current particle physics [41].

Thanks to high energy e^+e^- experiments, considering quantum electrodynamics (QED) and that the electron and the positron are both point-like it can be therefore concluded that μ^+ and μ^- are point-like too.

Free muons interact with other charged particles via the Coulomb interaction creating different possible bound states:

- muonium μ^+e where e stands for the electron;
- muonic hydrogen μ^-p where p is the proton;
- muonic Z-atoms μ^-Z .

High precision spectroscopy using these bound states offers a unique set of QED tests. These experiments also provide very precise measures of the muon properties, such as its mass (m_μ) and its magnetic moment (μ_μ). m_{μ^+} can be determined very precisely by measuring the energy interval between the 1S and 2S quantum levels in muonium. m_{μ^-} can be evaluated measuring the energy interval between atomic states in muonic Z-atoms [42].

In the following Table 1.1 are summarized the main muon properties.

	μ^+	μ^-
Charge	+1	-1
Spin	1/2	1/2
Mass (m_μ)	105.658386(44)[43] (MeV)	105.6583715(35) (MeV)[42]
Magnetic moment (μ_μ/μ_p)	3.18334513(39)[43]	3.183345137(85) [44]
Free decay lifetime (10^{-6} s)	2.196803(22)[45]	2.1948(10)[44]

Table 1.1 Muon properties.

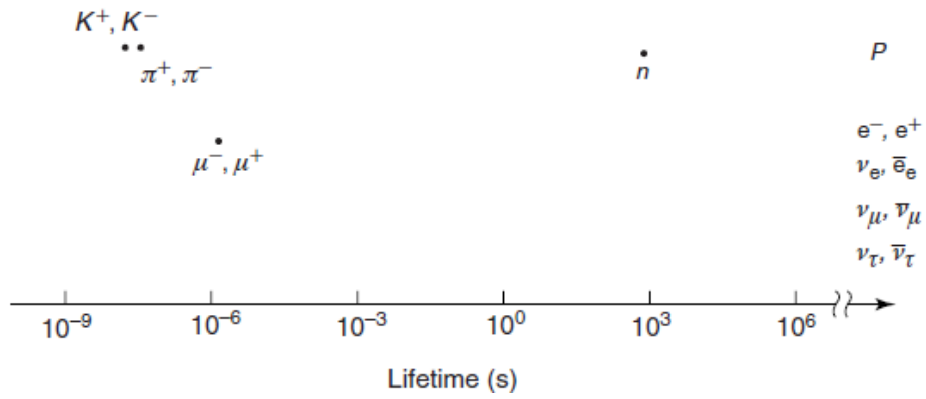


Fig. 1.1 Lifetime of various particles [1]. On the left we can see the kaon, pion and muon lifetime. In the centre of the picture, the neutron lifetime is shown ($\approx 10^3 s$) while on the far right side the stable particles are shown.

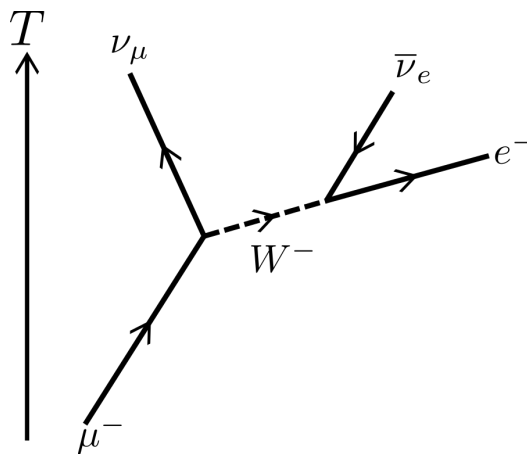


Fig. 1.2 Feynman diagram of the μ^- decay.

1.2 Muon decay and lifetime

Muons decay via the weak interaction. Its lifetime follows an exponential rule $\propto e^{-\frac{t}{\tau_\mu}}$. The strength of the weak force is governed by the Fermi Constant (G_F). Within the standard model, G_F is given by:

$$\frac{G_F}{\sqrt{2}} = \frac{g^2}{8M_W^2} (1 + \sum_i r_i), \quad (1.1)$$

where $1/M_W^2$ is the three-level propagator corresponding to the W boson (Fig. 1.2) exchange and g is the weak coupling. The $\sum_i r_i$ take into account the higher-order electro-weak interactions. The Fermi constant can be expressed in relation to the muon lifetime (τ_μ):

$$G_F = \sqrt{\frac{192\pi^3}{\tau_\mu m_\mu^5} \frac{1}{1 + \Delta q^{(0)} + \Delta q^{(1)} + \Delta q^{(2)}}}, \quad (1.2)$$

where the " Δq " factors are theoretical corrections accounting non zero electron mass on the muon-decay phase space and the contributions of one and two loop radiative corrections. In 2013 at PSI the MuLan experiment [45], using positive muons obtained the best uncertainty in the value of τ_μ :

$$\tau_\mu = 216980.3 \pm 2.2 ps.$$

Using this value and the m_μ in Table 1.1 in the (1.2), it results:

$$G_F = 1.1663787(6) \times 10^{-5} GeV^{-2},$$

that is the most accurate value of the Fermi constant and it is listed in the CODATA database [46].

The Fermi constant obtained from the muon lifetime is mandatory for the universality tests of the weak force. Comparison between the leptonic decays (the tau and the muon ones) are excellent opportunities to test the universality of leptonic weak interactions across the three generations. Using the available data on the lifetime and its purely leptonic $\mu \nu \bar{\nu}$ and $e \nu \bar{\nu}$ branching ratios the leptonic universality of weak interactions have been determined to the levels of several parts-per-thousand

[47].

The above considerations involved measurements of the τ_μ for positive muons only. For stopped negative muons, in addition to the decay process, the capture by the nucleus is possible (for further details see section 1.6). This is a concurrent process that reduces the apparent lifetime. For this reason, the negative muon lifetime estimation is far more complicate and this is reflected in the higher uncertainty in its measure.

1.3 Muon production

Muon science is made possible by the use of intense and high-quality muon beams. Cosmic rays were the only muon source before accelerator physics begun, The energy range of these muons is centred in the GeV region. Muons in the MeV or sub MeV energy region, are preferred because of their short stopping range (nm-cm).

Muons can be only produced by the pion decay:

$$\pi^+ \rightarrow \mu^+ + \nu_\mu,$$

$$\pi^- \rightarrow \mu^- + \bar{\nu}_\mu,$$

with a probability of 99.9877%. The second most possible decay with a branching fraction of 0.000123 is also a leptonic decay into an electron and the corresponding electron anti-neutrino. The charged pions mean lifetime is $\tau_\pi = 2.6 \times 10^{-8}s$. Pions are produced from high energy collisions between hadrons, in particular, protons. If a proton (p_1) collides with one at rest (p_2), for the four-momenta (p^μ) conservation principle, it is possible to calculate the impinging proton energy threshold to produce a pion (π):

$$\begin{aligned} p_1^\mu + p_2^\mu &= p_1'^\mu + p_2'^\mu + p_\pi^\mu, \\ \langle p_1^\mu | p_1^\mu \rangle + 2\langle p_1^\mu | p_2^\mu \rangle + \langle p_2^\mu | p_2^\mu \rangle &= \langle p_1'^\mu | p_1'^\mu \rangle + 2\langle p_1'^\mu | p_2'^\mu \rangle + 2\langle p_1'^\mu | p_\pi^\mu \rangle + \langle p_2'^\mu | p_2'^\mu \rangle \\ &\quad + 2\langle p_2'^\mu | p_\pi^\mu \rangle + \langle p_\pi^\mu | p_\pi^\mu \rangle. \end{aligned} \tag{1.3}$$

$p^\mu p_\mu = \langle p^\mu | p^\mu \rangle$ is invariant for any frames of reference so $p^\mu p_\mu = m^2 c^2$ and simplifies to:

$$2m_p^2 c^2 + 2 \langle p_1^\mu | p_2^\mu \rangle = 4m_p^2 c^2 + 4m_p m_\pi c^2 + m_\pi^2 c^2, \quad (1.4)$$

p_2 is initially at rest so $p_1^\mu = (\frac{E}{c}, \vec{p})$ and therefore:

$$2m_p E = 2m_p^2 c^2 + 4m_p m_\pi c^2 + m_\pi^2 c^2. \quad (1.5)$$

Rearranging for E we obtain:

$$E = m_p c^2 + 2m_\pi c^2 + \frac{m_\pi^2 c^2}{2m_p}. \quad (1.6)$$

Using the constants for the proton and pion masses $m_p = 938 \text{ MeV}/c^2$ and $m_\pi = 139.6 \text{ MeV}/c^2$:

$$E = 1.228 \text{ GeV} \implies T = 289 \text{ MeV}, \quad (1.7)$$

where T is the minimum kinetic energy the proton must have.

The cross section σ_π of the pion production in proton-nucleus in respect of proton energy is shown in Fig. 1.3, the main laboratories are listed as well.

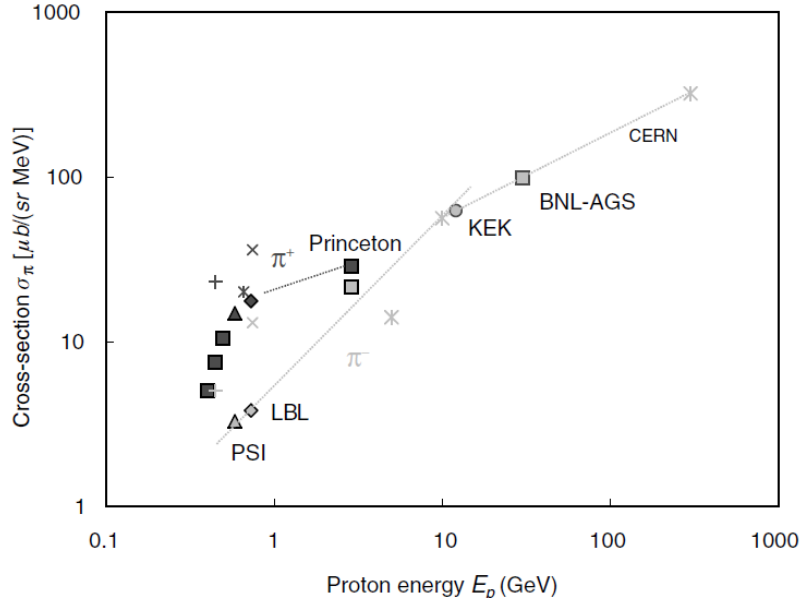


Fig. 1.3 Cross section for 50MeV π^+ , π^- production in respect of the proton beam energy. The main muon source laboratories are listed [1].

The decay length of pions with momentum p_π (in MeV/c) is:

$$L_\pi = c\beta\gamma\tau_\pi = 5.593 \times p_\pi,$$

where c is the speed of light, γ is the Lorentz factor, $\beta = v/c$ and $\tau_\pi = 2.6 \times 10^{-8} \text{ s}$, as stated previously is the pion lifetime at rest. A moderate pion momentum in the 100 MeV/c–200 MeV/c range, permits a decay length in the range of 5.6 m–11.2 m. When the pion decays into a muon, the latter momentum in the pion rest frame is 29.8 MeV/c and its direction is isotropic. In the laboratory frame, pions are moving with momentum p_π so the muons momentum has a flat distribution between two limits corresponding to forward (Fw) and backward (Bw) decay in the pion rest frame:

$$p_\mu^{Fw} = (\beta_\pi + \beta_\mu^*)p_\pi / [\beta_\pi(1 + \beta_\mu^*)],$$

$$p_\mu^{Bw} = (\beta_\pi - \beta_\mu^*)p_\pi / [\beta_\pi(1 + \beta_\mu^*)],$$

the backwards decay product muons are more interesting. Their momentum is about half of the p_π so they can be cleanly separated from other particles, in particular pions. Both of them have full polarization, +1 and -1 respectively.

The pion beam has all the three pion species (π^+ , π^- , π^0). Due to the π^0 decay:

$\pi^0 \rightarrow e^+ + e^-$, a large number of electron/positron could potentially contaminate the beam. Various momentum selecting magnets can reduce this "background". There are three different types of muon production depending on where, in real space, the $\pi \rightarrow \mu$ decay takes place in respect of the pion production: decay, cloud, and surface. Only the first one is able to produce negative muons.

In the sub-GeV region (proton beam energy) the π^+ production rate is four times higher than the π^- [1]. This is reflected in the μ^+/μ^- yield too.

A classic decay muon channel (muons beam-line from decay) consists in three main elements:

- Pions collection system, able to select the p_π and inject into the decay section.
- In the decay section, pions decay into muons while in flight whilst being confined by a superconducting solenoid (Fig. 1.4). The length of this solenoid is comparable with the pion decay length.
- A muon extraction system selects the operating momentum and act as a filter for unwanted particles as electron/positron and remaining pions.

There are two different muon delivery methods: continuous and pulsed. In the first case, the instantaneous muons flux is low (some MHz) and each particle is identified and all the measurable events are associated with an individual muon. In the pulsed method, an instantaneous intense muon pulse is stopped inside the target to test (through X-rays and/or e^-/e^+ measurements). Each pulse is separated by several milliseconds. There is no labelling associated to a single muon. The advantages of the latter method are mainly two: the possibility to stimulate the muonic target in between two separated pulses and the ability to perform the measurements far from the the beam muons-sample interaction instant that can be source of background noise (i.e. electron/positron, photons and neutrons, quite typical in accelerator buildings).

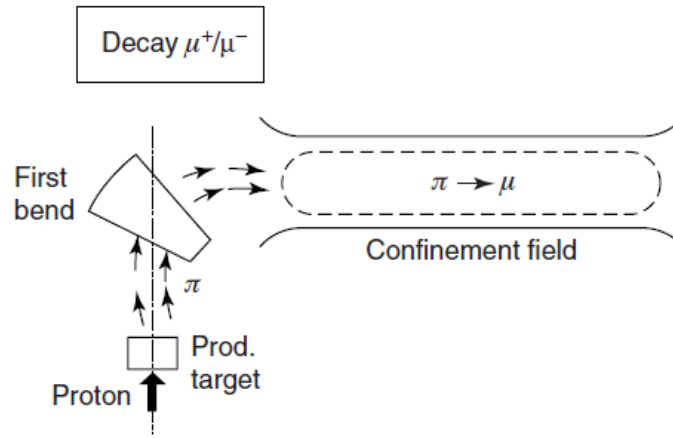


Fig. 1.4 Decay muons production scheme [1].

1.4 Muon interaction with matter

Positive and negative muons interact with matter at energy higher than some tenths of keV without significant difference (Fig. 1.5) [14]. The main mechanism of energy loss in the energy range 100 keV – 100 GeV is ionization and this is described by the Bethe formula (1.8)[1]. This formula describes the energy loss dE along a dx path, of a charged particle with charge e (in multiples of electron charge), speed v and energy E into a target of electron number density n and mean excitation potential I :

$$-\frac{dE}{dx} = \frac{4\pi}{m_e c^2} \cdot \frac{nz^2}{\beta^2} \cdot \left(\frac{e^2}{4\pi\epsilon_0}\right)^2 \cdot \left[\ln\left(\frac{2m_e c^2 \beta^2}{I \cdot (1 - \beta^2)}\right) - \beta^2 \right], \quad (1.8)$$

where c is the speed of light, ϵ_0 the vacuum permittivity, $\beta = \frac{v}{c}$ and m_e the electron rest mass. The electron density of the material can be calculated by:

$$n = \frac{N_A \cdot Z \cdot \rho}{A \cdot M_u},$$

where ρ is the density of the material, Z the atomic number, A the relative atomic mass, N_A the Avogadro number and M_u the molar mass constant. Using this formula is possible to calculate quantitative information about the muons range (R_0) in matter.

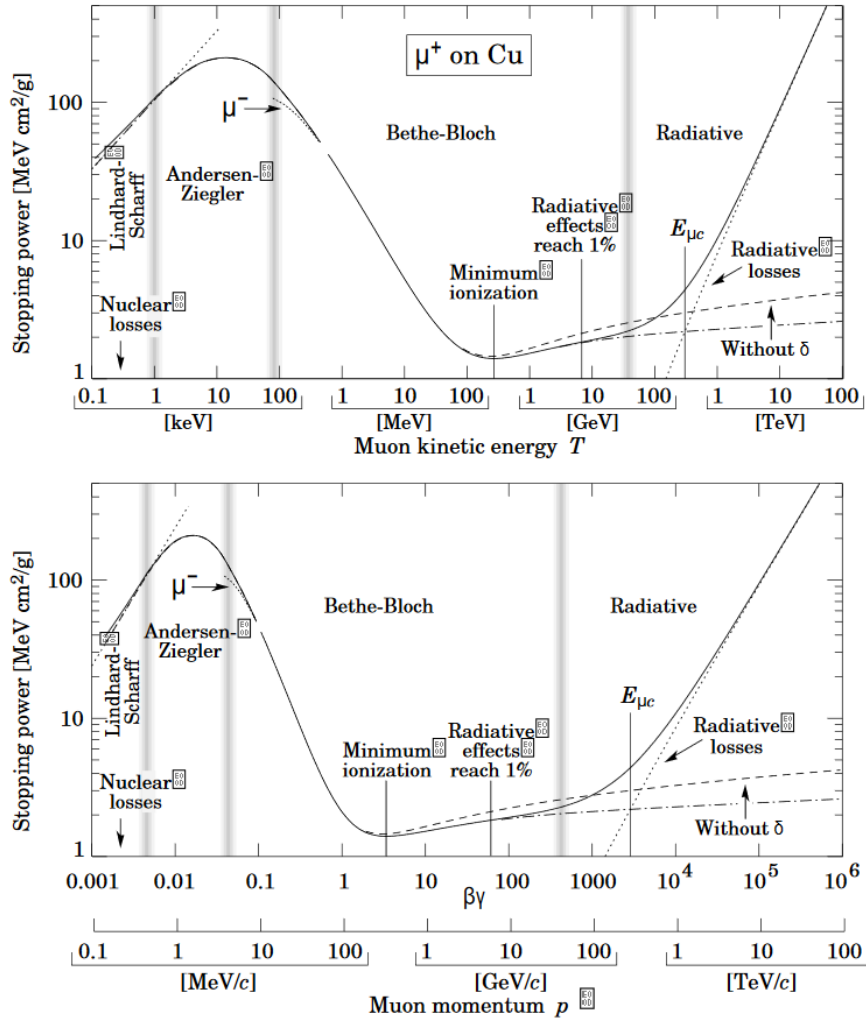


Fig. 1.5 Stopping power of positive muons in copper as a function of kinetic energy (top) and momentum (bottom) [2].

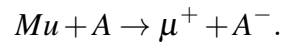
During the ionization process, due to the statistical nature of the collisions (scattering) involved, a collimated muon beam impinging any kind of target, is subjected to a spatial spread in the lateral (D_{\parallel}) and longitudinal (D_{\perp}) directions. Through semiempirical calculations it is possible to express this spread as a function of the range (R_0) [48]:

$$D_{\parallel} = 2.6 \times 10^{-2} R_0^{0.94},$$

$$D_{\perp} = 7 \times 10^{-2} R_0^{0.92}.$$

When the energy of the muon is lower than few keVs the behaviour differs depending on the charge.

For μ^+ in gases, insulator and semiconductors, at the end of the ionization phase, due to the Coulomb attraction, muonium (Mu) is formed. Mu is a hydrogen-like atom made by the bound state of μ^+ and e^- . After its formation, muonium decelerates because of elastic collisions with surrounding atoms. During these collisions there is a finite probability that the electron of Mu is captured by the colliding atom releasing the $\mu^+ e^-$ bond:



If muon is polarized, the formed Mu is polarized too. During the slowing down process, the polarization loss is in the order of 0.1 mstr [49]. Mu is in a paramagnetic state and when μ^+ decays, the spatial distribution of the emitted positron is oriented along the Mu (or μ^+) polarization. Because of its paramagnetism, Mu is used to investigate microscopic magnetic properties of condensed matter thanks to a method called muon spin rotation/relaxation/resonance or μ SR. The technique consists in measuring the positrons spatial distribution of a sample subjected to a muon beam (to form muonium) immersed in a static or dynamic magnetic field. μ SR is the main technique among muon physics.

In metals, μ^+ can't form Mu because of the strong collisions with electrons in the conduction band that prevent the binding state.

It is possible to imagine μ^+ as a "small" proton when interacts with matter. On the other hand, μ^- is more similar to an electron. As it is slowed down to some keV, μ^- is strongly attracted (by a Coulombian force) by the nuclear electric field. At this point, the muon replaces an electron of the atomic shell to form an exotic state of matter: a muonic atom.

1.5 Muonic atoms

Muonic atoms are created when a negative muon is stopped in material and one electron of the atomic shell is replaced by this muon. Fermi and Teller suggested that the capture probability was proportional to the atomic number of the hosting atom ($\propto Z$) [50]. More studies on oxides shown that the capture probability is

affected, not only by electronic shells related effects but by the atomic structure too. Taking into account the target density (ρ) and the valency (V), Stanislaus et al developed a relationship which works quite well for oxides, chlorides and fluorides [3]:

$$A\left(\frac{Z_1}{Z_2}\right) = 0.6\rho(1 + \alpha_1\rho)\left(\frac{Z_2}{Z_1}\right)^{\frac{1}{8}}(1 + 5.53V^{5.45} \times 10^{-5}), \quad (1.9)$$

with $\alpha_1 = 0$ for $Z_1 \geq 18$, -0.164 for oxides with metal $Z_1 \leq 18$ or -0.222 for chlorides with metal $Z_1 \leq 18$.

Because of the muon mass, the formed atom is quite different from the host one. For low atomic number (Z) nuclei, using the point like nuclei dimension approximation, the ground state ($1s$) radius ($R_\mu(1s)$) and energy ($E_\mu(1s)$) can be described as:

$$R_\mu(1s) \approx 270/Z \times 10^{-13}(cm),$$

$$E_\mu(1s) \approx 13.6 \times Z^2(eV),$$

where 207 is the ratio between m_μ and m_e . The energy levels differ from the point like approximation because of two factors: the finite nuclear size (obviously) that becomes more important for heavy nuclei, and the vacuum polarization.

When the muonic atom is formed, it is in an excited atomic state with critical quantum number $n_c = \sqrt{m_\mu/m_e} = 14$. The muonic states take quantum numbers distribution around n_c and the associated quantum number l .

The return to the ground state results into the emission of Auger electrons (transitions between higher orbits) and X-rays (lower orbits), respectively:

$$(\mu^-Z)_n + Z' \rightarrow (\mu^-Z)_{n'} + Z'^+ + e^-,$$

$$(\mu^-Z)_n + Z' \rightarrow (\mu^-Z)_{n'} + \gamma.$$

The muon cascade to the ground state takes place in about 10^{-9} seconds. This kind of phenomena is so fast with respect to the mean lifetime of the muon that we can assume that muon is stable in the scale time of the muonic atom.

Starting from the initial main quantum number (n) that for the most case is n_c , the distribution of the initial occupation of different l values is:

$$W(l) = (2l + 1)e^{\alpha_2 l} \quad \text{and} \quad n_0 = n_c = 14, \quad (1.10)$$

where α_2 is a parameter that is near to 0 ($\alpha_2 \leq 0.1 - 0.3$). Starting from (1.10) it is possible to compute all the X-rays and Auger electron emission transitions. The energy levels (in the point like nucleus approximation) are expressed by:

$$E_{n,j} = -\frac{m_\mu c^2}{1 + m_\mu/A} \frac{(Z\alpha)^2}{2n^2} \left[1 + \left(\frac{Z\alpha}{n} \right)^2 \left(\frac{n}{j+1/2} - \frac{3}{4} \right) \right], \quad (1.11)$$

where α is the fine-structure constant and j the total angular momentum quantum number, which is equal to $|l \pm 1/2|$ depending on the direction of the electron spin. Due to the muon mass, the difference in the energy levels is bigger than in traditional atoms. $\Delta n = 1$ transitions are the most likely to happen, such as $4f \rightarrow 3d$ or $3d \rightarrow 2p$ and so on, but $\Delta n \geq 1$ transitions can also occur with lower intensity. Similarly to the common atomic notation, the lines having as final state the ground state (1s) are called Lyman series, the ones that have as final state the 2s one are called Balmer series. Due to the spin interaction, a fine structure pattern is present. The p level, for instance, is split in two different levels: $2p_{1/2}$ and $2p_{3/2}$. The latter is more energetic and has twice the intensity than the former. The difference between the two levels is quite small for light elements but as $Z=22$, the separation is 2.2keV and it is possible to resolve it with Germanium detectors. The point-like assumption works well for low Z nuclei or for high order orbitals (Fig. 1.6).

In Table 1.2, some X-rays lines of some elements are shown. These lines are "narrow, come in patterns, and are emitted instantaneously with the arrival of the muon. They can thus act as a useful beacon in navigating a spectrum, indicating which elements are present" [3].

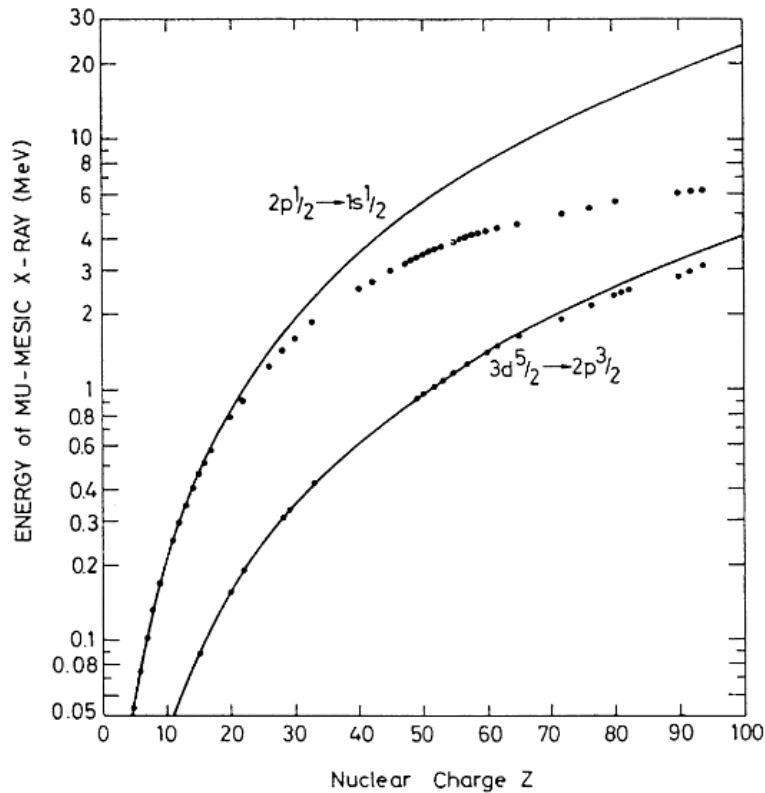


Fig. 1.6 Energies of muonic X-rays. The lines are the predicted values for a point nucleus [3].

The levels are in theory statistically populated and the lines intensity ratios are:

$$(2p_{3/2} - 1s_{1/2}) : (2p_{1/2} - 1s_{1/2}) = 2 : 1,$$

$$(3d_{5/2} - 2p_{3/2}) : (3d_{3/2} - 2p_{3/2}) : (3d_{3/2} - 2p_{1/2}) = 9 : 1 : 5,$$

$$(4f_{7/2} - 3d_{5/2}) : (4f_{5/2} - 3d_{5/2}) : (4f_{5/2} : 3d_{1/2}) = 20 : 1 : 14.$$

In reality, the levels are not quite populated statistically, so for example, the first ratio is closer to 1.9 than 2. Moreover, if a muon is stopped in a gas, the electrons are ejected, and cannot refill before the muon reaches the $1s$ state. Thus, the cascade proceeds more by X-ray emission (than Auger) and the $2p-1s$ transition has a higher yield.

Element	$2p - 1s$ (keV)	$3p - 1s$ (keV)	$4p - 1s$ (keV)	$2d - 2p$ (keV)
C	75.2588(5)	89.212(15)	94.095(15)	13.966(3)
N	102.403(5)	121.437(15)	128.091(16)	19.04(1)
O	133.535(2)	158.422(4)	167.125(5)	24.915(6)
²³ Na	250.229(2)	297.461(13)	313.961(12)	47.26(2)
²⁷ Al	346.828(2)	412.877(10)	435.981(12)	66.11(2)
Si	400.177(5)	476.829(12)	503.59(4)	76.723(10)
Cl	578.6(3)	691.4(3)	730.9(3)	113(1)
K	712.69(3)	854.34(5)	903.84(5)	143.8(4)
Ca	782.7(2)	941(1)	997(1)	156.83(2)
	784.15(3)			158.17(2)
Fe	1253.06(6)	1525(1)		265.7(1)
	1257.19(5)			269.4(1)
⁸⁹ Y	2420.1(4)	3033.1(6)		599.4 (4)
	2439.4(5)	3038.6(6)		616.4(4)
¹²⁷ I	3667.36(4)			1101.8(2)
	3723.74(3)			1150.4(2)
¹⁹⁷ Au	5591.71(15)	8091(1)		2341.2(5)
	5760.79(15)	8135(1)		2474.2(5)
²⁰⁸ Pb	5778.1(1)	8453.95(10)		2500.59(3)
	5962.9(1)	8501.15(11)		2642.33(3)

Table 1.2 Energies of muonic X-rays in a few elements, for heavy elements the $2p_{3/2} - 1s$ and the $2p_{1/2} - 1s$ transitions are listed [3].

1.6 Nuclear muonic capture

In muonic atoms, as the muon is in the ground state, its orbit overlaps the charge nuclear distribution. In this situation, the muon could interact with a nuclear proton via the weak interaction producing a neutron and muonic neutrino (Fig. 1.7):

$$\mu^- + p \rightarrow n + \nu_\mu. \quad (1.12)$$

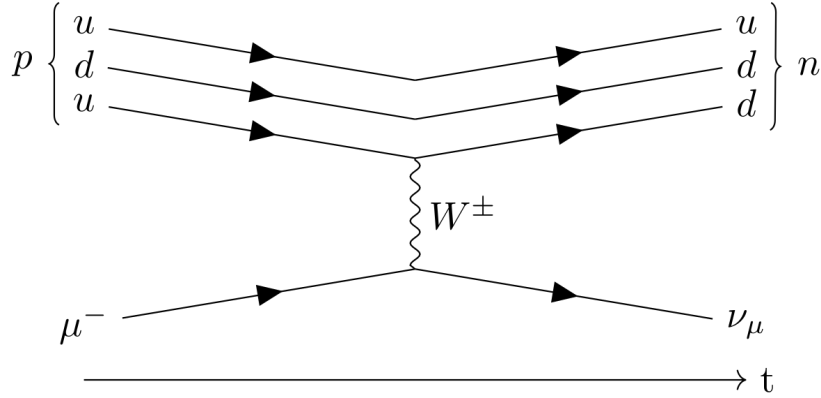


Fig. 1.7 Feynman graph of the muon proton interaction.

The capture rate measure is far easier than its calculation. Measuring the apparent muon lifetime gives us a good estimation of the capture rate. When muon replaces an atomic electron it reaches the ground state in some picoseconds. At this point, it could either decay or be captured by the nucleus. The measured apparent lifetime is the simple sum of the capture rate and the decay rate:

$$\Lambda_t = \Lambda_c + Q\Lambda_d,$$

where $\Lambda_t = (\tau_\mu^-)^{-1}$, $\Lambda_d = (\tau_\mu^+)^{-1}$ or the decay rate of a free muon and Q is the Huff factor ([51] and experimentally [52]). It is a numerical value, Z dependent, that takes into account not only relativistic time dilatation but mainly the fact that the decay rate for a bound μ^- is reduced because the binding energy reduces the available energy amount for the decay itself. For heavy nuclei, the situation is a bit more difficult: due to the neutron abundance (with respect to protons) and the Pauli exclusion principle, it becomes more difficult for protons to transmute in neutrons. Primakoff proposed this formula for the capture rate [53]:

$$\Lambda_c(A, Z) = Z_{eff}^4 X_1 \left[1 - X_2 \left(\frac{A-Z}{2A} \right) \right], \quad (1.13)$$

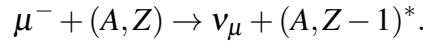
where $X_1 = 170s^{-1}$ is the muon capture rate for hydrogen but reduced because the neutrino has less energy for nuclear capture. $X_2 = 3.125$ takes into account the Pauli exclusion principle. This formula was extended by Goulard [54] adding two

more fitting terms for relativistic corrections:

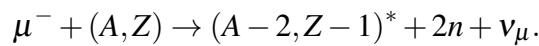
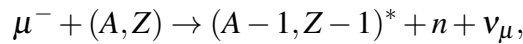
$$\Lambda_c(A, Z) = Z_{eff}^4 G_1 \left[1 + G_2 \frac{A}{2Z} - G_3 \frac{A-2Z}{2Z} - G_4 \left(\frac{A-Z}{2A} + \frac{A-2Z}{8AZ} \right) \right]. \quad (1.14)$$

In Fig. 1.8 the comparison between the two models and experimental data is shown. This model gives a reasonable, but not perfect, description of the phenomenon [3].

As soon as the capture happens, the interested atom loses a proton gaining a neutron. For this reason, a nuclear transmutation occurs and, because the formed nucleus is in an excited state it could emit γ -rays, β particles and so on. In formula the transmutation is:



From the comparison with the (π^-, γ) reaction it is possible, with a simple scaling process due to the masses difference between π and μ ($m_\pi/m_\mu \simeq 9$), to figure out that the muon capture should excite the nucleus of about 10-20 MeV [3]. The average neutron binding energy (for stable elements) in the nucleus is about 8 MeV (Fig. 1.9) so the capture process results in one or two neutron emission. This leads to further nuclear transmutations:



The created nucleus de-excitation is followed by γ -rays emission. By this emission is possible to experimentally extract the nuclear capture rate.

As an example, let's take oxygen in its 99.757% natural abundance stable isotope ^{16}O . As the capture occurs, two gamma lines are visible at 120 keV and 276 keV [55]. By consulting an isotopes chart it is possible to recognize the two lines coming from the excited ^{16}N nucleus. The measured rate $\Lambda_O^{nuclear} = 102.5 \times 10^3 \text{ s}^{-1}$ [3].

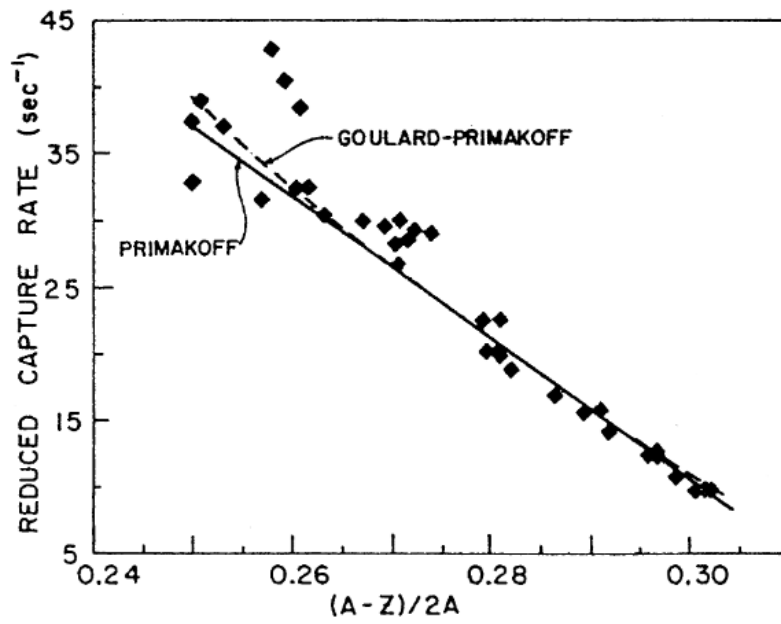


Fig. 1.8 Comparison of the reduced muon total capture rate with the Primakoff formula (1.13), and the Goulard–Primakoff extension,(1.14). The black solid squares are the experimental data from Suzuki et al [3].

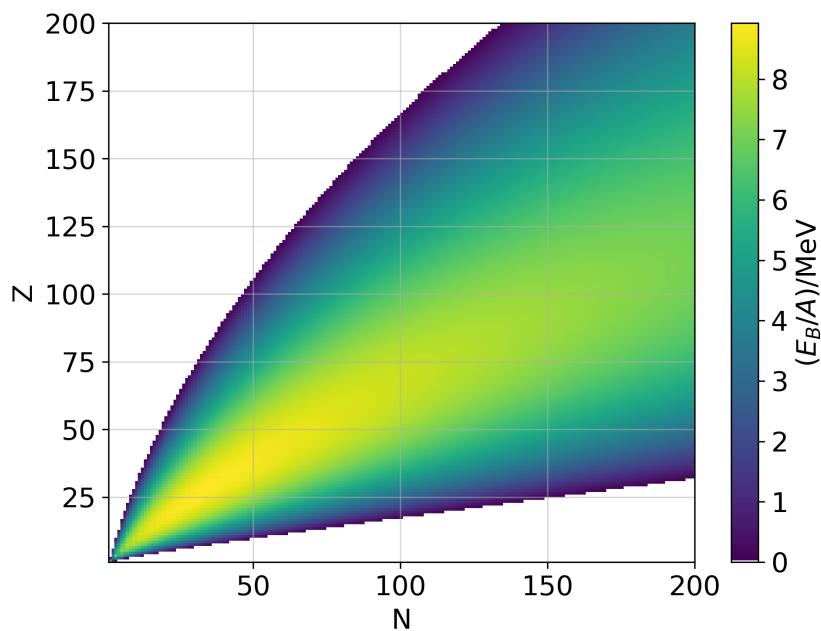
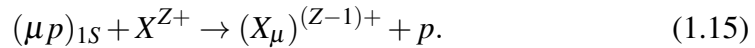


Fig. 1.9 Binding energy per nucleon from Bethe-Weizsäcker formula in the intervals $Z, N = [1, 200]$.

1.7 Muon transfer rate

Hydrogen represents a special element for muon physics. When the muon is captured by hydrogen and reaches the ground state it can either decay or be captured by the nuclear proton. For this element, the capture to decay probability ratio is of the order of 4×10^{-4} . Thus, the resulting bound neutral state (called μp) has a lifetime comparable with the one of the free muon. Because of its neutrality, μp can easily penetrate the potential barrier of nearby atoms and the muon can quickly be transferred to the higher Z nucleus (X^Z), in formula:



The transfer occurs, due to the stronger Coulomb potential of the higher Z nucleus. Thus, in case of a target made of molecules in which one of the elements is hydrogen, such as H_2O , the behaviour in negative muonic interactions is, in effect, as a pure oxygen target. In a low-pressure environment, with a high hydrogen concentration and only some per cent (or less) of a heavy element, however, the transfer rate is slower and can be observed. This "slow" transfer can take hundreds of nanoseconds and can be monitored by the emission of characteristic muonic X-rays from the cascade of the receiving heavy element (X_{μ}).

It was found that some elements, especially oxygen, exhibit complex transfer rates. Oxygen is one of the very few elements for which there exist experimental and theoretical data about the energy dependence of the transfer rate but they don't fully agree. The main idea behind this phenomenon is that the μp atoms, after their formation, have a variety of energies, up to several tens of eV. The transfer rate is related, for some elements on this kinetic energy.

The first studies were performed on sulphur oxide showing a difference in the muonic X-rays emission between sulphur and oxygen. The first one shows a pure exponential decay X-rays time distribution, while appears more complex for the latter. In Fig. 1.10 b) we can notice a slow decay (with the same decay constant τ_1 as in the sulphur case) and a fast component τ_2 [4]. τ_2 was found to depend on the target pressure and the oxygen concentration [33]. The suggested interpretation tells us that τ_2 reflects the mean lifetime of a particular $\mu p(1S)$ state which decays through two distinct channels respectively related to the hydrogen density (c_p) and the oxygen concentration (c_o). The latter is related to the muon-oxygen transfer

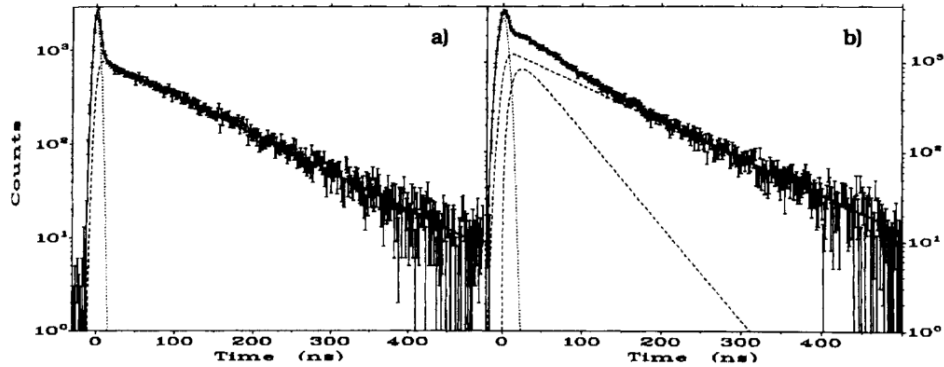


Fig. 1.10 Muonic X-rays time distribution for sulphur on the left and oxygen on the right. The first one shows a pure exponential decay while a more complex structure is evident in the case of oxygen [4].

while the first one is due to the μp thermalization process [33]. Hence, the τ_2 parameter can be expressed:

$$\tau_2^{-1} = \lambda_2 = \lambda_0 + \phi(c_p \lambda_p + c_o \lambda_{pO}^*), \quad (1.16)$$

where λ_p is the thermalization rate and λ_{pO}^* the transfer to oxygen rate. A first model suggested three different oxygen transfer rates depending on the μp energy (Fig. 1.11) [5]:

- $\lambda_{pO} = 8.5 \times 10^{10} s^{-1}$ for μp energies in the $[0 - 0.12]$ eV range;
- $\lambda_{pO} = 39 \times 10^{10} s^{-1}$ for μp energies in the $[0.12 - 0.22]$ eV range;
- $\lambda_{pO} = 0$ above 0.22 eV.

In the epithermal region (0.12–0.22 eV) the transfer rate is more than four times bigger than in the thermal one. Some studies suggested the existence of a resonance at relatively low energy [56].

Further studies have shown a more complicate energy dependence on the transfer rate. In particular, Le and Lin [6], using adiabatic hyperspherical close-coupling calculations for the charge exchange of a negative muon from muonic hydrogen to oxygen, computed the transfer energy dependence in the 10^{-3} – 10^3 eV region. Results are shown in Fig. 1.12(a) as comparison with another reference [32] and in Fig. 1.12(b) where the electron screening was investigated using the Fermi–Teller

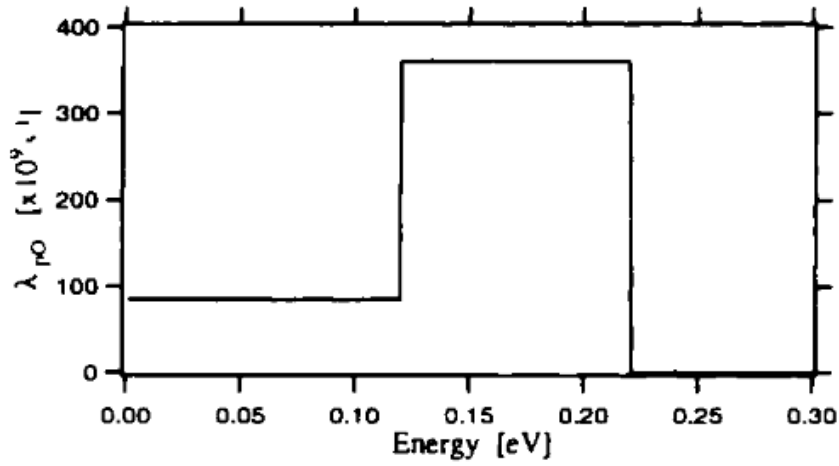
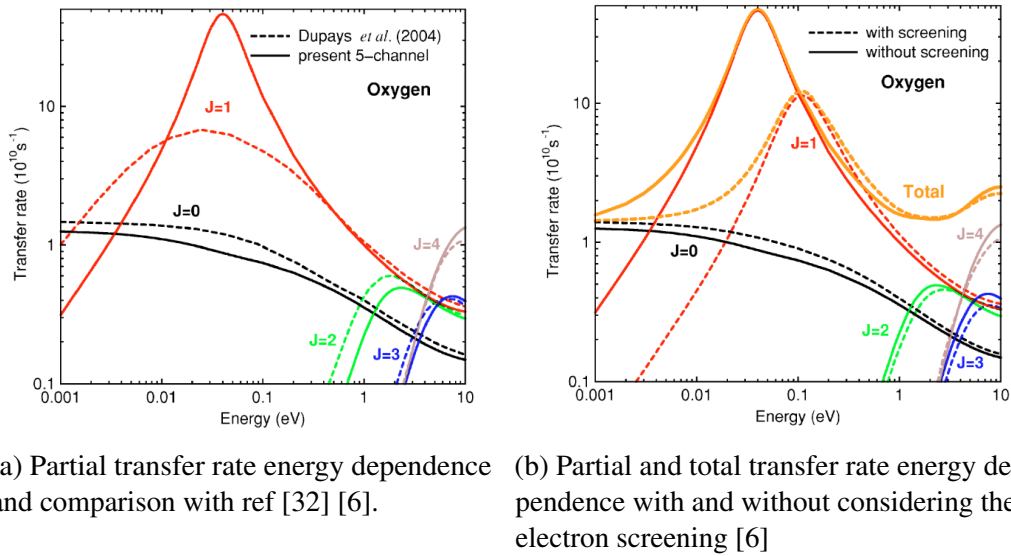


Fig. 1.11 Transfer rate from hydrogen to oxygen versus the μp energy. Three different region are present [5].



(a) Partial transfer rate energy dependence and comparison with ref [32] [6]. (b) Partial and total transfer rate energy dependence with and without considering the electron screening [6]

Fig. 1.12 Transfer rate energy dependence in the 0–10 eV region [6].

reduced potential.

When μp reaches the same kinetic energy of the other particles in the gas, its energy is, as for the entire gas volume, related to the target temperature. In fact, the energy distribution ($f_E(E)$) of the gas molecules can be parametrized with a Maxwell-Boltzmann function where the temperature parameter (T) is the gas

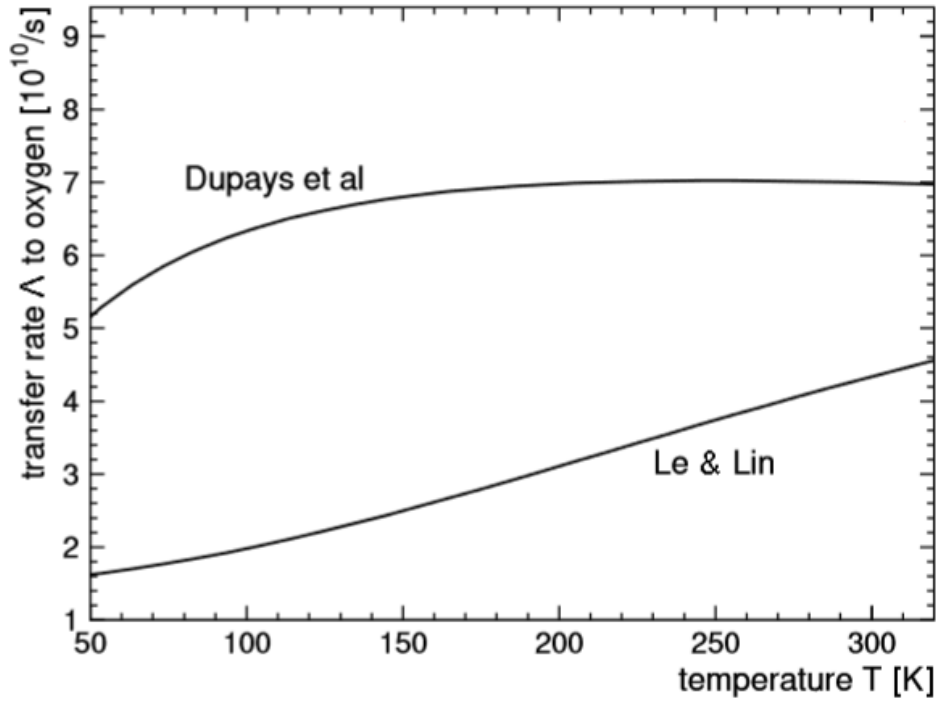


Fig. 1.13 Transfer rate from hydrogen to oxygen versus the gas target [7].

temperature itself:

$$f_E(E)dE = 2\sqrt{\frac{E}{\pi}}\left(\frac{1}{kT}\right)^{3/2}e^{-\left(\frac{E}{kT}\right)}dE. \quad (1.17)$$

By using this conversion, in the 50–320 K temperature range, the transfer behaviour of [6] and [32] is shown in Fig. 1.13. The different models are not in good agreement. thus, more studies are needed to fully understand the transfer process.

The muonic hydrogen ground state has a hyperfine structure with two levels ($F=0$ and $F=1$) separated by 0.182 eV (see section 2.3.2). When μp in the $F=1$ state collides with H_2 molecules in the gas, it de-excites and accelerates by $\sim 2/3$ of the hyperfine energy [57]. It results in an excess of energy that can be shared with the collisional partners. Thus, this is a source of epithermicity for the transfer process.

Chapter 2

Proton radius puzzle

This second section is focused on the so-called "Proton radius puzzle" that is still an unanswered problem in physics.

The "puzzle" arises due to the discrepancy (of more than 5%) amongst totally independent ways to measure the proton charge radius (Fig. 2.1):

- electron-proton scattering (e-p) and its
- dispersion relation analysis (DR);
- hydrogen and deuterium spectroscopy (H/D);
- muonic hydrogen spectroscopy carried out at PSI by the CREMA collaboration (μp).

Another spatial related observable, called Zemach radius (R_Z or r_{EM}), could lead to the puzzle solution. The various measures of this observable demonstrate inconsistencies among them though (Fig. 2.2).

Most of the measures in Fig. 2.1 and Fig. 2.2 are going to be quickly explained as the methodology involved in the measure itself. In the following sections, some notions about the proton and its spatial related observables are provided. These are related to the fine and hyperfine splitting of the electric or muonic (surrounding the proton) energy levels. The main contribution to the fine splitting is the Lamb shift, thus it will be explained.

The importance of muons in this research as investigating particle will be pointed out, mainly in the Lamb shift paragraph.

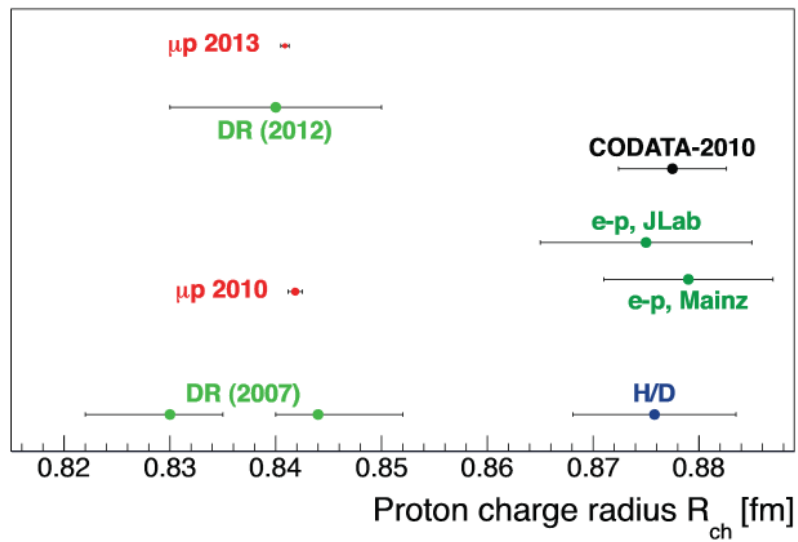


Fig. 2.1 Summary of the main measurements of the proton charge radius (R_{ch} or $\langle r_E^2 \rangle^{1/2}$). In the following pages most of the measures will be explained [8].

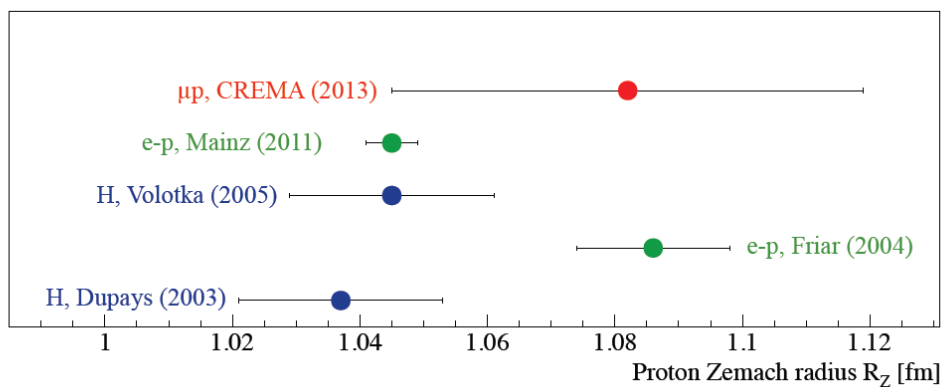


Fig. 2.2 Summary of the main measurements of the proton Zemach radius (R_Z or $\langle r_{ME}^2 \rangle^{1/2}$). In the following pages most of the measures will be explained [8].

2.1 Proton

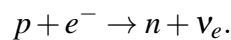
A proton (p or p^+) is a subatomic particle with a positive unitary charge +1, spin 1/2, magnetic moment of $\kappa = 1.5210322053(46) \times 10^{-3} \mu_B$ and it is composed by three valence quarks: 2 up and 1 down. Thus it is classified as a Baryon. The three quarks (uud) are held together by the strong force via gluons interaction. Its mass $938.2720813(58) \text{ MeV}/c^2$ [44] is composed just in small part by the quarks rest mass ($\simeq 9.4 \text{ MeV}/c^2$) but mainly by the gluons quantum chromodynamics binding energy (QCBE).

The free proton is considered a stable particle in the Standard Model and has not been observed to break down spontaneously to other particles. Multiple experiments give lower limits for the proton mean lifetime (τ_p):

- $\tau_p = 6.6 \times 10^{33}$ years for the $p \rightarrow \mu^+ + \pi^0$ decay;
- $\tau_p = 8.2 \times 10^{33}$ years for the $p \rightarrow e^+ + \pi^0$ decay;
- a more general $\tau_p = 2.1 \times 10^{29}$ years for any kind of decay product.

The first two values are from Super-Kamiokande detector in Japan [58] while the latter one is from the Sudbury Neutrino Observatory in Canada. It searched for gamma rays from residual nuclei resulting from the decay of a ^{16}O proton [59]. The age of the universe is $\sim 1.37 \times 10^{10}$ years thus, any of the protons generated in the Big Bang have still $\simeq 10^{19}$ years of life span.

Similarly to the nuclear muon capture (see 1.6), protons can interact with electrons through the electron capture process (or inverse beta decay) producing neutrons and electronic neutrinos. This process takes place only if energy is provided to the proton (typically from the nucleus):



Such as for the atomic radius, the definition of proton radius is quite misleading. Protons (as atoms) don't have definite boundaries however it is possible to model proton as a sphere of positive charge, in particular for electron scattering experiments. The qualification of "rms" (for "root mean square") arises because it is the proton cross-section, proportional to the square of the radius, which is determining for electron scattering. Anyway, the shape of a proton varies from a simple sphere

for protons free in space to complex shapes when part of an atomic nucleus, due to pressures from contact with adjacent protons and neutrons [60].

2.2 The proton radius (scattering)

We can treat the theoretical assumption on the proton radius from an experimental point of view, in particular from the scattering experiments one. Let's start with the Rutherford cross section scattering formula:

$$\left(\frac{d\sigma}{d\Omega}\right)_R = \left(\frac{Z\alpha}{2E}\right)^2 \frac{1}{\sin^4(\theta/2)}, \quad (2.1)$$

where E is the electron energy and θ is the resulting angle after the interaction in respect to the incoming direction. This equation takes into account the hypotheses that the interacting particles are point-like and spinless, the proton has infinite mass, the interaction is elastic, non-relativistic and described by the Coulomb force, and the validity of the $Z_1 Z_2 \alpha \ll 1$ relation where Z_s are the particle charges. The last hypothesis is also known as the Born approximation.

Because the proton dimension is of the order of the fm, the electron must have energy above 200 MeV (from $\lambda = \hbar c$) and, at these energies, the electron is moving at relativistic speeds. The Mott formulation considers this effect changing the 2.1 into:

$$\left(\frac{d\sigma}{d\Omega}\right)_M = \left(\frac{d\sigma}{d\Omega}\right)_R (1 - \beta^2 \sin^2 \theta/2). \quad (2.2)$$

Rosenbluth taking into account the proton spin introduced two form factors (A and B):

$$\left(\frac{d\sigma}{d\Omega}\right)_{Ros} = \left(\frac{d\sigma}{d\Omega}\right)_M [A(q^2) + B(q^2) \cdot \tan^2(\theta/2)]. \quad (2.3)$$

In this formulation, the proton is still dimensionless or point-like. To obtain a more interesting relation between scattering parameters and the proton radius, some QED's concepts are needed. In accordance with the QED, the e-p scattering can be described using Feynman diagrams so from the (Fig. 2.3.a) situation where a single photon is exchanged to the more complex vertex (Fig. 2.3.b) situation passage is

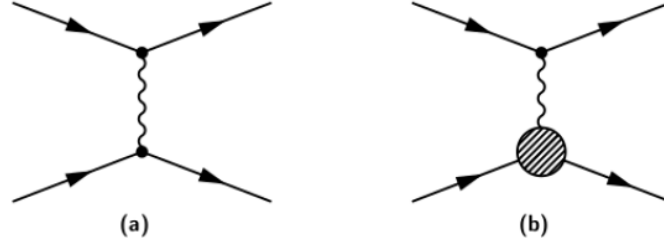


Fig. 2.3 Feynman graph of the e-p interaction where in (a) p is point-like and in (b) it has finite dimension

needed. The matrix element of the interaction is:

$$M_{fi} = J_{\mu}^{elec} \frac{1}{q^2} J_{prot}^{\mu}, \quad (2.4)$$

in which $J_{\mu}^{elec} = -e\bar{u}(k')\gamma_{\mu}u(k)$ and $J_{prot}^{\mu} = e\bar{u}(p')\Gamma^{\mu}u(p)$ are the electron and proton currents, $q = k - k'$ is the exchange momentum; (k, k') and (p, p') are the initial and final four-momenta respectively of electron and proton, and $u(k)$ $u(p)$ their associated spinors.

The proton current J_{prot}^{μ} is a Lorentz four vector and using the Gordon decomposition:

$$\Gamma^{\mu} = [F_1(q^2)\gamma^{\mu} + \frac{\kappa}{2m_p}F_2(q^2)i\sigma^{\mu\nu}q_{\nu}], \quad (2.5)$$

where $\sigma^{\mu\nu} = i[\gamma^{\mu}\gamma^{\nu}] / 2$, $F_1(q^2)$ and $F_2(q^2)$ are phenomenological form factors. " F_1 is associated with the Dirac charge and intrinsic magnetic moment of the proton and F_2 is associated with the Pauli part of the moment" [61].

The cross section is obtained by calculating the modulus squared of the matrix element and by summing over the final spins and averaging on the initial ones. The final result for the Rosenbluth cross section is:

$$\begin{aligned} \left(\frac{d\sigma}{d\Omega}\right)_{Ros} &= \left(\frac{d\sigma}{d\Omega}\right)_M \left\{ [F_1(q^2) - \frac{\kappa^2 q^2}{4m_p^2}F_2(q^2)] \right\} \\ &\quad - \left(\frac{d\sigma}{d\Omega}\right)_M \left\{ \frac{q^2}{2m_p} [F_1(q^2)\kappa F_2(q^2)] \tan(\theta/2) \right\}. \end{aligned} \quad (2.6)$$

At this point is possible to rewrite the 2.6 introducing the electric and magnetic form factors (G_E and G_M):

$$G_E = F_1 + \frac{\kappa q^2}{4m_p^2} F_2,$$

$$G_M = F_1 + \kappa F_2,$$

so the Rosenbluth cross section becomes:

$$\left(\frac{d\sigma}{d\Omega}\right)_{Ros} = \left(\frac{d\sigma}{d\Omega}\right)_M \left\{ \frac{G_E^2(Q^2) + \tau G_M^2(Q^2)}{1 + \tau} + 2\tau G_M^2(Q^2) \tan^2 \theta / 2 \right\}, \quad (2.7)$$

in which $Q^2 = -q^2$ and $\tau = Q^2/(4m_p^2)$. G_E describes the proton electric charge distribution and G_M the magnetic dipole moment distribution. We can describe the behaviour of these two form factor as a function of q^2 with a dipole expression:

$$G_E(q^2) = \left(\frac{1}{1 + (q^2/0.71)} \right)^2, \quad (2.8)$$

with q^2 is expressed in $(\text{GeV}/c)^2$.

The form factor can be expressed as a function of the charge density ρ_E applying the Fourier transform:

$$G_E(q^2) = \int \rho(r) e^{iqr} dr. \quad (2.9)$$

Investigating the region in which the exchanging momentum is almost zero ($q^2 \rightarrow 0$):

$$\begin{aligned} G_E(q^2) &\simeq \int [1 + iq \cdot r - 1/2(q \cdot r)^2 + \dots] \rho(r) \\ &= Q(0) - 1/6Q^2 \int r^2 \rho(r) dr + \dots \\ &= Q(0) - 1/6Q^2 \langle r^2 \rangle + \dots \end{aligned} \quad (2.10)$$

where $Q(0)$ is the proton charge. From the last relations, it is possible to extract the mean squared value of the proton charge radius:

$$\langle r_E^2 \rangle = - \frac{6}{G_E(0)} \left. \frac{dG_E(Q^2)}{dQ^2} \right|_{Q^2=0}. \quad (2.11)$$

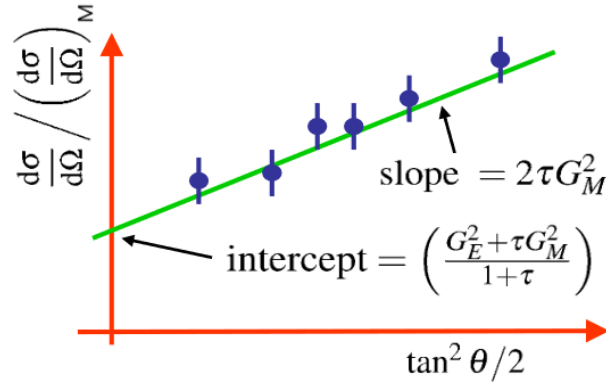


Fig. 2.4 Cross section extrapolation example

A similar procedure leads to the mean squared magnetic radius:

$$\langle r_E^2 \rangle = -\frac{6}{G_M(0)} \left. \frac{dG_M(Q^2)}{dQ^2} \right|_{Q^2=0}. \quad (2.12)$$

To practically determine the two form factors, the equation 2.3 is exploited. With q^2 fixed, the ratio of the measured cross sections to the Mott cross section versus the deflecting angle is studied. From the linear fit of these data, it is possible to extract both the $B(Q^2)$ and $A(Q^2)$ values as the slope and the y-intercept respectively. By the analogy between the equations 2.3 and 2.7 the two form factors thus the charge and magnetic rms radii can be measured (Fig. 2.4).

2.3 The proton radius (hydrogen spectroscopy)

Another way to extract the proton radius is to investigate the electronic distribution of the hydrogen atom. According to the Lamb shift, the electron-proton bound and thus the electronic distribution is affected by the proton dimension. The idea is to exploit the radiation emissions of stimulated energy transitions in order to investigate the proton dimension.

The radiation wavelength (λ) emitted by an electronic transition between two energy levels (m and n with $m < n$) in hydrogen is described by the Balmer's formula

(in the Rydberg's formulation):

$$\frac{1}{\lambda} = R_H \left(\frac{1}{m^2} - \frac{1}{n^2} \right). \quad (2.13)$$

R_H is the Rydberg constant, it is expressed as the inverse of a length and represents the minimum wave number of a photon that can be emitted from the hydrogen atom ground state leaving it ionised:

$$R_H = \alpha^2 \frac{m_e c^2}{2\hbar c}. \quad (2.14)$$

Assuming that the proton is point-like, has infinite mass in respect of the electron and considering a central Coulomb potential, generated by the proton, the energy levels depend only on the principal quantum number (n) (Bohr interpretation):

$$E_n = -m_e c^2 \frac{(Z\alpha)^2}{2n^2}. \quad (2.15)$$

The Dirac formulation takes into account the relativist energy dependence of an electron on its momentum and the electron spin. A general expression of the atomic energy levels is described by the following equation:

$$E_{njl} = mc^2 + Mc^2 + (f(n, j) - 1)m_r c^2 - (f(n, j) - 1)^2 \frac{m_r^2 c^2}{2(m + M)} + \frac{1 - \delta_{l0}}{(j + 1/2)(2l + 1)} \frac{(Z\alpha)^4 m_r^3 c^2}{2n^3 M^2}, \quad (2.16)$$

where M is the nuclear mass, $m_r = \frac{mM}{m+M}$ is the reduced mass, n , j and l are the quantum numbers and

$$f(n, j) = \left[1 + \frac{(Z\alpha)^2}{(n - j - 1/2 + \sqrt{(j + 1/2)^2 - (Z\alpha)^2})^2} \right]^{-1/2}.$$

From this formulation the 2S and 2P energy levels degeneration appears broken (j dependency of the formula).

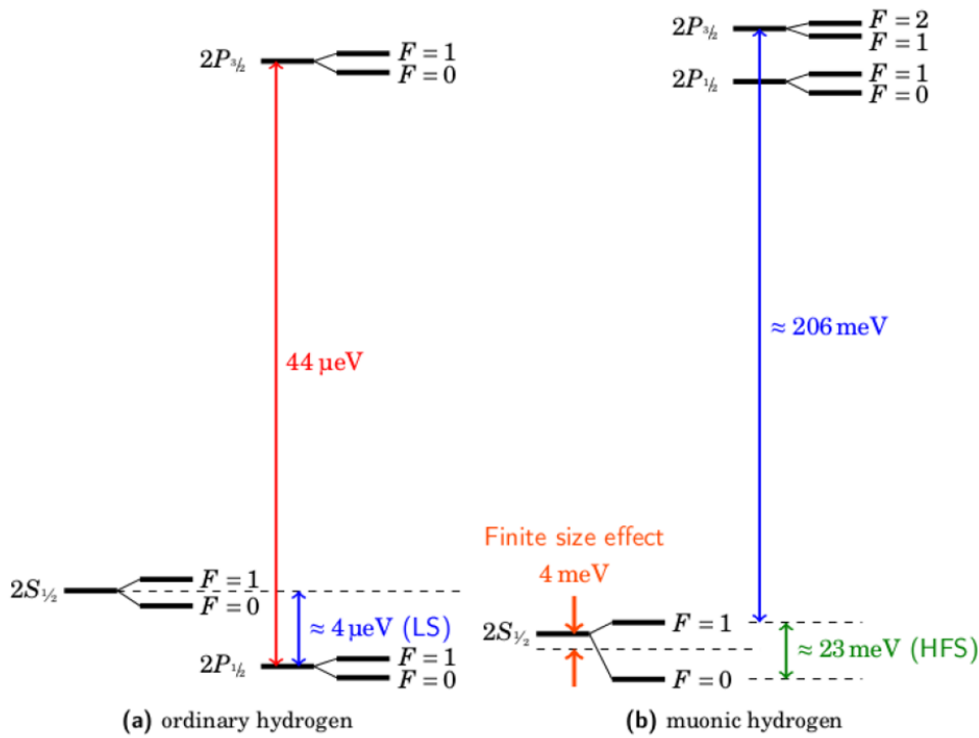


Fig. 2.5 Summary of the fine and hyperfine splitting for the $n=2$ state for ordinary hydrogen and muonic hydrogen. LS stands for Lamb shift and HFS for hyperfine splitting [8].

2.3.1 Fine structure and Lamb shift

In 1947, Willis Lamb discovered that $2P_{1/2}$ state energy is slightly lower than the $2S_{1/2}$ resulting in a small shift of the corresponding spectral line (LS in Fig. 2.5). This was not predicted by Dirac, in fact, in the Dirac formulation, the two states are degenerate thus, a fine structure in the atomic levels exists. This discovery was the harbinger of modern quantum electrodynamics (field theory) and Lamb won the Nobel Prize in Physics in 1955 for his discoveries.

The main contributions to the Lamb shift phenomenology are [62]:

- radiative corrections: they take into account QED effects as self-energy and vacuum polarization for an electron in a Coulomb potential of an infinite heavy and point like nucleus; they depend only on α and $Z\alpha$;

- recoil corrections: they reflect the finite size of the nucleus and arise from the fact that the reduced mass introduction can't consider relativistic recoil corrections. They depend on $Z\alpha$ and m/M ;
- radiative-recoil corrections: they take into account recoil contributions with radiative QED phenomenology such as photon loops. They depend on α , $Z\alpha$ and on the two masses involved ratio (m/M);
- finite nuclear size corrections: they are needed when the proton is not considered point-like. This causes a deviation in the Coulomb potential and depends on r_E .

The only contribution that shows dependency on the proton radius is the last one and can be expressed as follows [63]:

$$\Delta E_{finitesize} = \frac{2\pi Z\alpha}{3} |\phi^2(0)|^2 \langle r_E^2 \rangle = \frac{2m_r^3 (Z\alpha)^4}{3n^3} \langle r_E^2 \rangle, \quad (2.17)$$

where $\phi(0)$ is the wave function at the origin in coordinate space. It is easy to notice the importance of the reduced mass term (m_r). As the investigating particle (electron or muon) mass increases, the effect on the energy splitting becomes larger and can be measured easily and more precisely. In fact, proton electron mass ratio is:

$$\frac{m_p}{m_e} = 1836.1526665(40), \quad (2.18)$$

and recalling the muon electron mass ratio:

$$\frac{m_\mu}{m_e} = 206.768277(24), \quad (2.19)$$

the splitting for electronic hydrogen:

$$\begin{aligned} {}^e\Delta E_{2S_{1/2}-2P_{1/2}} &= 1057.833(4) \text{MHz}/h \\ {}^e\Delta E_{2S_{1/2}-2P_{1/2}} &\simeq 4.372 \mu\text{eV}, \end{aligned} \quad (2.20)$$

to compare with the muonic hydrogen one:

$$\begin{aligned} {}^\mu\Delta E_{2P_{3/2}-2S_{1/2}} &= 49.8084(12)(150) \text{THz}/h \\ {}^\mu\Delta E_{2P_{3/2}-2S_{1/2}} &= 205.991(5)(62) \text{meV}, \end{aligned} \quad (2.21)$$

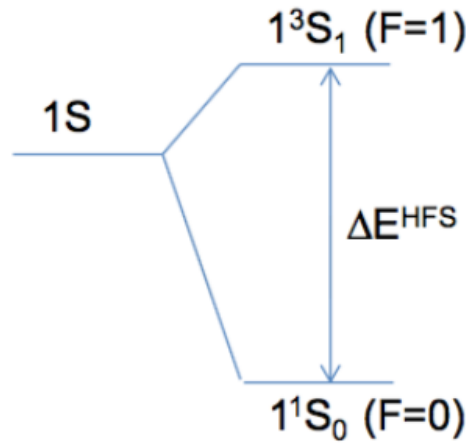


Fig. 2.6 Hyperfine splitting: F=0 singlet and F=1 triplet state.

in which it is possible to extrapolate the $\langle r_E^2 \rangle$ dependency:

$${}^\mu \Delta E_{2P_{3/2}-2S_{1/2}} = [206.0336(15) - 5.2275(10) \langle r_E^2 \rangle + 0.0332(20)] \text{meV}. \quad (2.22)$$

The effect of the muon mass increases the Lamb shift of ≈ 40000 times that is roughly the square of the masses ratio.

2.3.2 Hyperfine structure and Zemach radius

There is another finer splitting in the atomic levels that depends on the interaction between the electron (J) and the nuclear (I) angular momentum (HFS in Fig. 2.5), ignored in the Dirac formulation. The atom energy levels depend on $F=I+J$. If we consider hydrogen, the ground state is split into two levels F=0 and F=1 and the energy difference is on the order of μeV . The two hyperfine states are named F=0 and F=1, and represent the singlet and triplet proton-muon spin coupling (Fig. 2.6).

The simple solution of the Hamiltonian interaction between non-relativistic Schroedinger-Coulomb wave functions of the two magnetic moments (muonic and nuclear) gives the Fermi result for the ground state splitting:

$$\begin{aligned} E^F &= \frac{8}{3} (Z\alpha)^4 (1 + \alpha_\mu) \frac{m_e}{m_\mu} \left(\frac{m_r}{m_e}\right)^3 mc^2 \\ &= \frac{16}{3} Z^4 \alpha^2 \frac{m_e}{m_\mu} \left(\frac{m_r}{m_e}\right)^3 chR_H, \end{aligned} \quad (2.23)$$

recalling that α is the fine structure constant, m_e , m_μ and m_r are the electron, the muon and, the reduced masses respectively; α_μ is the muon anomalous magnetic moment and R_H the Rydberg constant.

Introducing all the relativistic effects and the QED described interactions, we can write the hyperfine energy split as a sum of different contributions:

$$\begin{aligned}\Delta E^{hfs} &= E^F (1 + \delta^{QED} + \delta^{struct}) \\ &= E^F (1 + \delta^{QED} + \delta^{Zemach} + \delta^{recoil} + \delta^{pol} + \delta^{hvp}),\end{aligned}\quad (2.24)$$

in which δ^{QED} includes radiative and recoil effects and is (up to the α^3 term):

$$\delta^{QED} = a_e + \frac{3}{2}(Z\alpha^2) + \alpha^2(\log 2 - \frac{5}{2}) - \frac{8\alpha^3}{3\pi} \log \alpha (\log \alpha - \log 4 + \frac{281}{480}) + 18.984 \frac{\alpha^3}{\pi} + \dots$$

where a_e is the electron anomalous magnetic moment. This contribution doesn't depend on masses (i.e. m_e or m_μ or m_r) or proton radius. However, they contribute to the δ^{struct} term that is composed by:

- δ^{recoil} , it contains the reduced mass contribution;
- δ^{pol} , it takes into account the fact that both the charge and magnetic distributions are polarized. An independent model measure doesn't exist but an upper limit from theoretical calculation can be fixed;
- δ^{hvp} depends on the vacuum polarization, in particular to the photon propagator in the Feynman for the lepton-proton interaction (Fig. 2.7);
- δ^{Zemach} that considers both charge and magnetic proton moment and more explicitly [64]:

$$\delta^{Zemach} = -2Z\alpha\mu \langle r_{EM} \rangle, \quad (2.25)$$

where $\langle r_{EM} \rangle$ is the Zemach radius and can be expressed as convolution of the proton charge and magnetic distribution:

$$\begin{aligned}\langle r_{EM} \rangle &= \int |r| d^3 r \int d^3 r' \rho_e(|r-r'|) \rho_\mu(r') \\ &= -\frac{4}{\pi} \int_0^\infty \frac{dQ}{Q^2} \left(G_E \frac{G_M(Q^2)}{\mu_p} - 1 \right),\end{aligned}\quad (2.26)$$

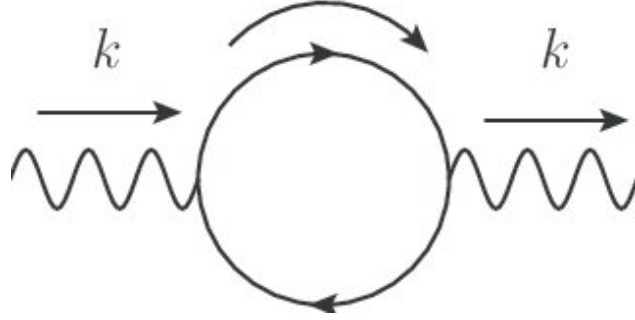


Fig. 2.7 One-loop Feynman diagram contribution to the vacuum polarization amplitude.

where ρ_e and ρ_μ are the charge and magnetic distribution respectively. The electric and magnetic form factors can be extracted by this relation and directly compared with the ones obtained by the scattering measurements.

In Table 2.1 are summarized the various contribution, and their uncertainty, to the hyperfine splitting for both traditional and muonic hydrogen. Calculations of the various contributions lead to these estimations that are in good agreement [8]:

$$\Delta E_{th}^{hfs} = 183.978(16) - 1.287 \langle r_{EM} \rangle [meV] \quad (2.27)$$

$$\Delta E_{th}^{hfs} = 183.967(16) - 1.287 \langle r_{EM} \rangle [meV] \quad (2.28)$$

in which $\langle r_{EM} \rangle$ is expressed in fm. The polarizability contribution uncertainty is the main source of the first term uncertainty.

To summarize, by measuring the hyperfine splitting of the muonic hydrogen ground state, it is possible to estimate the Zemach radius ($\langle r_{EM} \rangle$). "The repeated

	Hydrogen		Muonic Hydrogen	
	magnitude	uncertainty	magnitude	uncertainty
E_F	1420 MHz	0.01 ppm	182.443 meV	0.1 ppm
δ^{QED}	1.16×10^{-3}	$< 0.001 \times 10^{-6}$	1.16×10^{-3}	10^{-6}
$\delta^{Zemach} + \delta^{recoil}$	39×10^{-6}	2×10^{-6}	7.5×10^{-3}	0.1×10^{-3}
δ^{recoil}	6×10^{-6}	$\times 10^{-8}$	1.7×10^{-3}	10^{-6}
δ^{pol}	1.4×10^{-6}	0.6×10^{-6}	0.46×10^{-3}	0.08×10^{-3}
δ^{hvp}	10^{-8}	10^{-9}	0.02×10^{-3}	0.002×10^{-3}

Table 2.1 Value and uncertainty of the ΔE_{th}^{hfs} contributions [35].

measurements of $\langle r_{EM} \rangle$ in hydrogen and muonic hydrogen are the best way to verify" the theoretical evaluation of the δ^{pol} in 2.24: "compatible values of $\langle r_{EM} \rangle$ extracted from the hyperfine splitting in hydrogen and muonic hydrogen will confirm the reliability of the theoretical values of δ^{pol} and vice versa"[35]. "A measurement of the Zemach radius on the 1% level or better will influence two aspects of fundamental physics: nuclear structure theory of the simplest nuclei as well as tests of bound-state QED." [8].

2.4 Scattering measurements results

Two main experiments in the last ten years provided the proton radii measurements through e-p scattering.

The first one is from the A1 collaboration at the Mainz Microtron MAMI (e-p Mainz). They measured about 1400 cross sections "with negative four-momentum transfers squared up to $Q^2 = 1(\text{GeV}/c)^2$ with statistical errors below 0.2%". Investigating several models they divided the fits to the measured data in two main groups: "those based on splines with varying degree of the basis polynomial and number of support points and those composed of polynomials with varying orders" [65]. For the first group they obtained (in fm):

$$\begin{aligned} \langle r_E^2 \rangle^{1/2} &= 0.875(5)_{stat}(4)_{syst}(2)_{model} \\ \langle r_M^2 \rangle^{1/2} &= 0.775(12)_{stat}(9)_{syst}(4)_{model}, \end{aligned} \quad (2.29)$$

for the second one (in fm):

$$\begin{aligned} \langle r_E^2 \rangle^{1/2} &= 0.883(5)_{stat}(5)_{syst}(3)_{model} \\ \langle r_M^2 \rangle^{1/2} &= 0.778 \begin{pmatrix} +14 \\ -15 \end{pmatrix}_{stat} (10)_{syst}(6)_{model}. \end{aligned} \quad (2.30)$$

The weighted average of the two differs by 0.008 fm. The cause of the discrepancy between the two model groups was not found. Therefore, as the final result they gave the average of the two values with an additional uncertainty of half of the difference:

$$\begin{aligned} \langle r_E^2 \rangle^{1/2} &= 0.879(5)_{stat}(4)_{syst}(2)_{model}(4)_{group} \\ \langle r_M^2 \rangle^{1/2} &= 0.777(13)_{stat}(9)_{syst}(5)_{model}(2)_{group} \end{aligned} \quad (2.31)$$

The second measure was performed in 2011 at Jefferson Lab (e-p JLab) in Hall A [66]. Using a 1.2 GeV polarized electron beam incident on a 6cm thick liquid hydrogen target, they measured the recoil proton polarization in coincidence with the elastically scattered electron. Using the one photon exchange (Born) formalism, the proton form factors are related to the ratio of the transverse (P_T) and longitudinal (P_L) polarization:

$$R = \mu_p \frac{G_E}{G_M} = -\mu_p \frac{E_e + E'_e}{2m_p} \tan(\theta/2), \frac{P_T}{P_L} \quad (2.32)$$

with μ_p the proton magnetic moment. They performed a low Q^2 analysis obtaining with 1% of uncertainty the electric and magnetic radii:

$$\begin{aligned} \langle r_E^2 \rangle^{1/2} &= 0.875 \pm 0.008_{exp} \pm 0.006_{fit} \\ \langle r_M^2 \rangle^{1/2} &= 0.867 \pm 0.009_{exp} \pm 0.018_{fit}. \end{aligned} \quad (2.33)$$

The two methods give a consistent evaluation of the charge radius but there is a big difference in the magnetic one.

The two previous measurements depend strongly on the model and the related fitting process. Dispersion relations provides a model-independent framework to analyse the nuclear form factors. A couple of studies, using experimental data, re-analysed the measurements obtaining interesting results. In particular, through two different approaches, Belushkin et al. [67] (DR 2007) found for the electric charge radius (in fm):

$$\begin{aligned} \langle r_E^2 \rangle^{1/2} &= 0.844 \begin{pmatrix} +0.006 \\ -0.004 \end{pmatrix}, \\ \langle r_E^2 \rangle^{1/2} &= 0.830 \begin{pmatrix} +0.005 \\ -0.008 \end{pmatrix}, \end{aligned} \quad (2.34)$$

and for the magnetic one (in fm)

$$\begin{aligned} \langle r_M^2 \rangle^{1/2} &= 0.854 \begin{pmatrix} +0.005 \\ -0.005 \end{pmatrix}, \\ \langle r_M^2 \rangle^{1/2} &= 0.850 \begin{pmatrix} +0.002 \\ -0.007 \end{pmatrix}. \end{aligned} \quad (2.35)$$

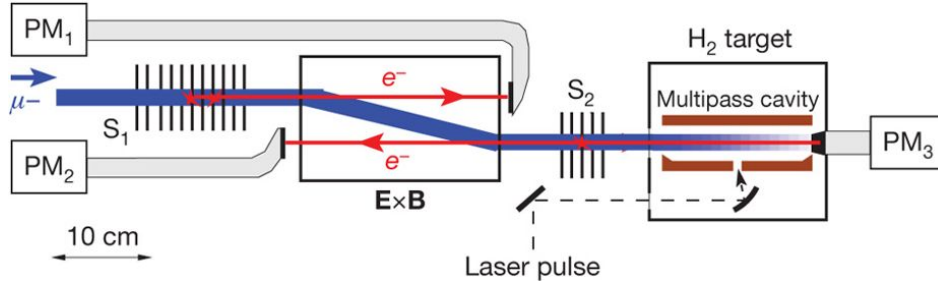


Fig. 2.8 CREMA Experimental setup. The muon beam passing through thin carbon foils (S_1S_2) is frictionally cooled and enters the 1 mbar H_2 target. The electrons generated are drifted by $E \times B$ and then read by 3 photomultiplier. The emitted X-rays are detected by 20 Large-Area Picosecond Photodetectors (LAPDDs not shown here) [9]

Lorenz et al. [68] (DR 2012), using the Mainz group data, obtained for $\langle r_E^2 \rangle^{1/2}$ and $\langle r_M^2 \rangle^{1/2}$ respectively (in fm):

$$\begin{aligned} \langle r_E^2 \rangle^{1/2} &= 0.84 \begin{pmatrix} +0.01 \\ -0.01 \end{pmatrix}, \\ \langle r_M^2 \rangle^{1/2} &= 0.86 \begin{pmatrix} +0.02 \\ -0.03 \end{pmatrix} \end{aligned} \quad (2.36)$$

The summary for the charge radius of all these measurements is shown in Fig. 2.1. The e-p scattering is a powerful tool to investigate the proton structure, but it relies on models. This is reflected in the difference between the dispersion analysis and the extrapolated data. Moreover, the two e-p scattering experiments give very different estimations of the magnetic radius that is reflected in the Zemach radius too Fig. 2.2.

2.5 CREMA muonic hydrogen spectroscopy

In 2009 at PSI (Paul Scherrer Institute), Switzerland the first successful measurement of the Lamb shift of muonic hydrogen was done by the CREMA (Charge Radius Experiment with Muonic Atoms) collaboration. From this measurement, the charge radius was extrapolated.

The PSI continuous slow negative muon beam had been used to create muonic hydrogen in 1 mbar (300 K) pressurized target. The very low gas pressure is needed to enhance the number of μp s in the $2S$ state over time. At higher pressures, $\mu p(2S)$

has enough energy (above $\sim 0.3eV$ in the laboratory frame) to collide with $\mu p(1S)$ resulting in a de-excitation thus, a fast 2S state depletion [69].

To stop muons in such a low-pressure target, the CREMA collaboration had to slow down the muon of the $\pi E5$ PSI muon beam line, from 10 MeV/c down to almost 0 keV. To do that, they used a mix of passive (Mylar film) and a 2 stages active moderation (via frictional cooling in thin carbon foils). This process produces electrons that are separated from the slowed muons by an electric and magnetic field (5T). The light emitted by these electrons passing through plastic scintillators is acquired by a photomultiplier and acts as the trigger. The whole muon stop volume is illuminated by the laser thanks to an optical cavity that permits multiple light reflections in order to increase the light-atom interactions (Fig. 2.8).

Right after the muonic atom creation, the muon decays mainly to the ground state (1S). There is a small probability (of about 1%) that the decaying particle ends up in the 2S energy level which is metastable ($1\mu s$ lifetime for 1 mbar H_2 gas pressure) [69] (Fig. 2.9 a). At this point, a tunable laser beam produces the muon $2s - 2p_{3/2}$ excitation that immediately de-excites to the ground state emitting 2 keV X-ray ((Fig. 2.9 b), promptly detected by an array of 20 avalanche photodiodes (LAAPD).

The time evolution of the X-rays emitted by the target at different laser frequencies shows a bump in coincidence with the laser emission when the 2S-2P transition is stimulated. By the comparison between the distribution with the laser (Fig. 2.10 a) and the one without (Fig. 2.10 b) is possible evaluate the maximum X-rays emission.

They obtained the maximum X-ray emission when the laser was tuned to a wavelength of $\simeq 6\mu m$ or a frequency of $49.88188(46)$ THz/h (Fig. 2.11) that is quite different from the predicted one in equation 2.21. From this frequency in Hz is possible to obtain the energy transition in meV. Putting it into equation 2.22 it is possible to evaluate the charge radius $\langle r_E^2 \rangle = 0.84184(67)$ fm (μp 2010 in Fig. 2.1) "which differs by 5.0 standard deviations from the CODATA value (which was basically related only to the e-p scattering measurements) of $0.8768(69)$ fm" [9].

In the next years, they introduced the hyperfine splitting in their experiment, in particular, they measured two different transitions (refer to Fig. 2.5):

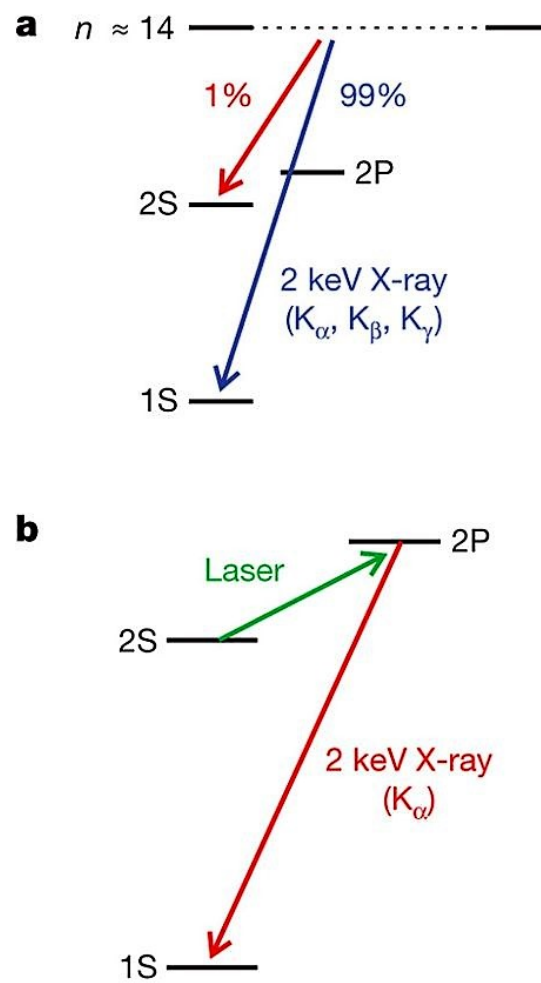


Fig. 2.9 Atomic levels scheme involved in the CREMA experiment. In a, right after the muonic hydrogen formation, the muon decays from $n=14$ to $n=1$ but with 1% of probability it can get stuck in the 2S state where the decay to the 1S is prohibited. In b a tuned laser source excite the muons in the 2S state to the 2P. Now the decay is possible emitting 2 keV X-rays [9].

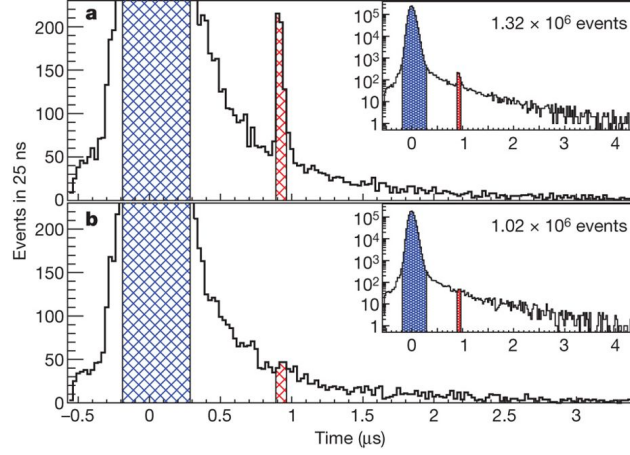


Fig. 2.10 Time evolution of the 2 keV X-rays emitted by the hydrogen target. The prompt phase (in blue) coincides with the muons arrival thus the muonic hydrogen formation. In a the laser was shot but not in b. It is clear that the laser excited the right resonance (2S-2P transition) [9].

- $2S_{1/2}^{F=1} - 2P_{3/2}^{F=2} = 49881.35(65)GHz$
- $2S_{1/2}^{F=0} - 2P_{3/2}^{F=1} = 54611.16(1.05)GHz$

and by them, the proton radius value $\langle r_E^2 \rangle = 0.84087(39) (\mu p \text{ 2013 in Fig. 2.1})$ was extract, increasing the difference with the CODATA one, up to 7σ .

It is very important to notice that the error associated with these measurements is some order of magnitude lower than the e-p scattering ones, demonstrating the value and reliability of the muonic hydrogen spectroscopy as a nuclear physics low energy high precision technique.

In 2014, the CODATA updated the proton charge radius value reducing the difference with the one measured by the CREMA collaboration at 5.6σ (Fig. 2.12) [10].

Moreover, from the 2013 data was possible to measure the ΔE^{hfs} for the 2S state. This hyperfine splitting shows a dependence from the Zemach radius (in fm), in particular [70]:

$$(2S)\Delta E^{hfs} = 22.9843(30) - 0.1621(10) \langle r_{EM} \rangle \text{ meV} \quad (2.37)$$

so:

$$\langle r_{EM} \rangle = 1.082(31)_{exp}(20)_{theory} \text{ fm} = 1.082(37) \text{ fm} \quad (2.38)$$

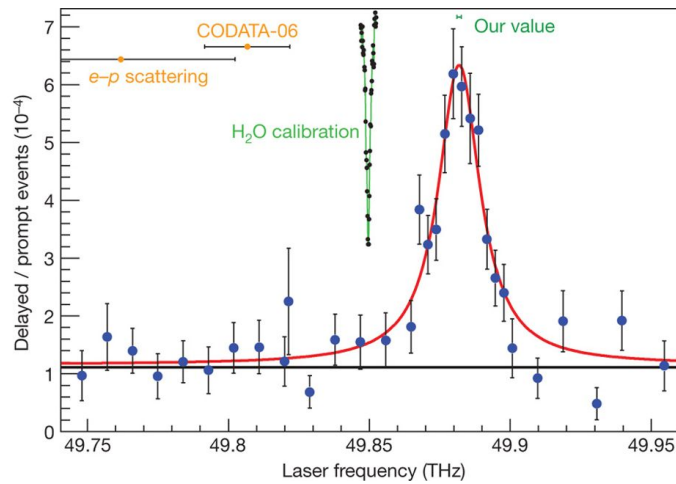


Fig. 2.11 Ratio of the delayed X-rays (by the laser excitation) over prompt ones (due to the muonic hydrogen formation) versus the emitted laser frequency. For comparison, the charge radius from CODATA and e-p scattering was used to calculate the Lamb shift and inserted in the graph [9].

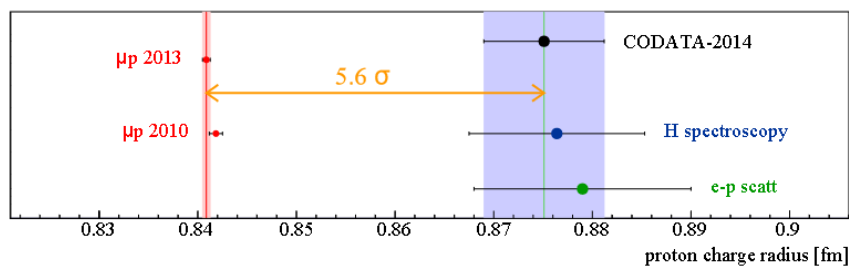


Fig. 2.12 Proton charge radius from different sources. The CODATA 2014 value takes into account e-p scattering, hydrogen and deuterium spectroscopy but doesn't consider the muonic results [10].

In Fig. 2.2 this value is shown and it is possible to notice the big uncertainty that doesn't help in the current Zemach radius scenario. The experimental error arises due to the measurement as a difference of two different measures; on top of this error, the theoretical uncertainty is quite big as well because of the different approximations needed for the hyperfine splitting of the 2S state.

Part II

The FAMU experiment

FAMU ("Fisica degli Atomi MUonici" that can be translated as Muonic Atomic Physics) is an international collaboration involving 25 institutions and about 60 scientists. It aims to give a measurement of the hyperfine splitting of the muonic hydrogen in the ground state ($\Delta E_{\mu p}^{hfs}(1S)$) with less than 1% of uncertainty. From this measure, it is possible to estimate the Zemach radius. Adding an independent measurement of the Zemach radius in the current panorama could give a hint to the proton radius puzzle solution.

Chapter 3

The strategy

The FAMU's experimental idea is to exploit muonic atoms behaviour, laser spectroscopy technique and X-rays detection to monitor the spin-flip transition of the muonic hydrogen ground state, from which is possible estimate the Zemach radius. The main concept is quite simple and described as follow. A hydrogen gaseous target is subjected to a low energy high-intensity muon beam in order to form muonic hydrogen (μp). Right after the formation, the μp s decay to the ground state, in particular, 75% of them to the F=1 (triplet) while the remaining 25% to the F=0 (singlet) hyperfine state (Fig. 2.6). A collisional thermalization process brings all these μp s to the singlet state (F=0). At this point, a laser source, tuned to the right hyperfine splitting energy ($\simeq 183$ meV), excites the μp s F=0 to F=1 transition. Through collisions with other H_2 molecules, the triplets de-excite to the singlet state but gaining about two-thirds of the hyperfine transition energy ($\simeq 122$ meV) [57]. Now, the question is: how to measure such a small amount of energy in a gas target?

Our idea is to take advantage of the μp neutrality, thus its ability to transfer the muon to another element forming a muonic atom. For some elements, the transfer process is regulated by the μp energy or in other words, by its excess in energy with respect of the total gas mixture. The formed muonic atom is in an excited state and due to the muon decaying to the ground state, the atom emits characteristic X-rays. Thus, observing the element characteristic X-rays time evolution in coincidence with the laser pulse will provide the laser wavelength triggering the spin-flip transition (F=0 \rightarrow F=1). The converted laser wavelength is the $\Delta E_{\mu p}^{hfs}(1S)$.

The contaminant element mixed with hydrogen inside the target is oxygen. The

muon transfer probability from μp to oxygen was investigated in the past with controversial results (see section 1.7), thus, we performed further tests.

Practically, the measurements method is composed of three different phases: the prompt, the thermalization and the laser phase. They are explained in the following pages.

Towards the final measurement, by now, only the first two phases were investigated, in particular, most of the effort was necessary to study the muon transfer process. This necessity arises to fix the optimal operative conditions in which we must perform the final measurements. As showed in 1.7, models are not in agreement. A schematic representation of the described strategy is in Fig. 3.1.

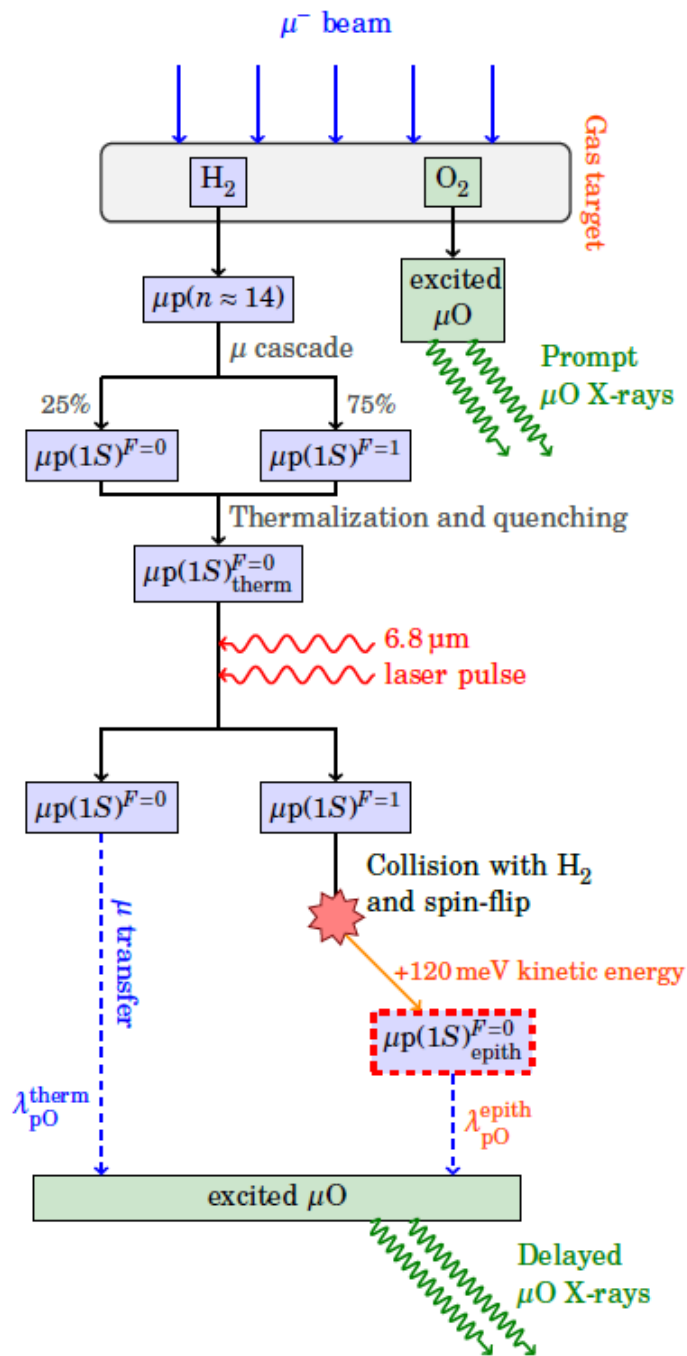


Fig. 3.1 FAMU experimental strategy scheme [11].

Prompt phase

The muon beam impinging the gaseous target produces muonic atoms, in particular, muons stop in the aluminium vessel, in hydrogen, forming μps and in the oxygen contaminant. These main muonic elements emit characteristic X-rays that can be measured (except for hydrogen whose lines are too low in energy so likely absorbed by the vessel itself) in coincidence with the muon beam, thus called "prompt phase".

Thermalization phase

In this phase all the muonic hydrogen thermalizes. The thermalization process depends on the hydrogen density ϕ and the initial gas temperature. Considering the $H_2 + O_2$ gas composition, thanks to Monte Carlo simulations it is possible to compute the time evolution of the μp energy for different temperatures at fixed ϕ . These simulations show that, interdependently from the temperature, the thermalization process ends after about 150 ns. Below this region, the thermalization curves differ due to the different thermal energy of the H_2 molecules (Fig. 3.2). Moreover, if we consider different gas pressures at a fixed temperature we can notice that, as the pressure increases, the thermalization rate increases as well (Fig. 3.3).

As stated before, right after the muonic hydrogen formation and the subsequent decay to the ground state, the singlet ($F=0$) and triplet ($F=1$) populations show a 25%/75% ratio. Due to collisions between $\mu p^{(F=1)}$ and H_2 molecules, the triplet state depopulates. The depopulation rate depends on the gas pressure and, as shown in Fig. 3.4, it is about ten times faster than the thermalization process (Fig. 3.3).

Taking into account both the triplet depopulation and the thermalization process, the time (t_0) at which the system can be consider totally thermalized is [12]:

$$t_0 \sim 20 \times \frac{T}{P}, \quad (3.1)$$

where T and P are respectively expressed in K and atm.

The μp collision with H_2 molecules can cause the formation of $pp\mu$. The production rate depends only on the hydrogen density. If the muon is captured by the entire hydrogen molecule, it cannot be transferred to oxygen. Another non-transferring species is the μd , where muon is captured by deuteron. The μd

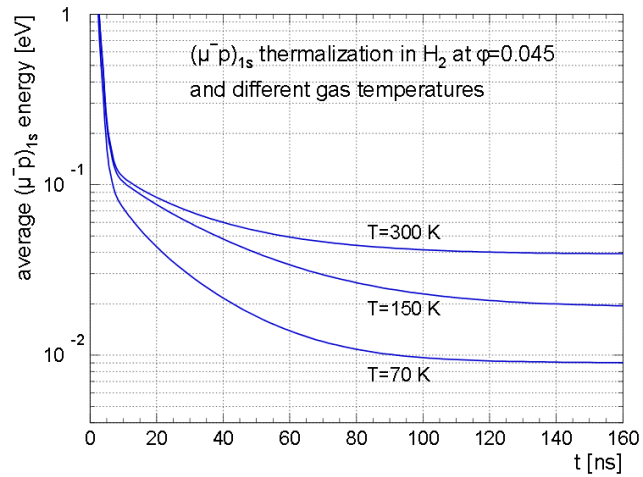


Fig. 3.2 Time evolution of the μp average energy at fixed density and different temperatures [12].

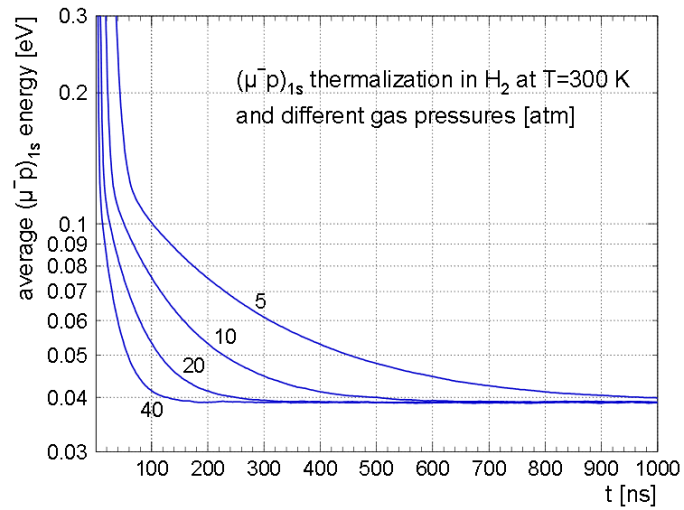


Fig. 3.3 Average μp energy versus time at different pressures [12].

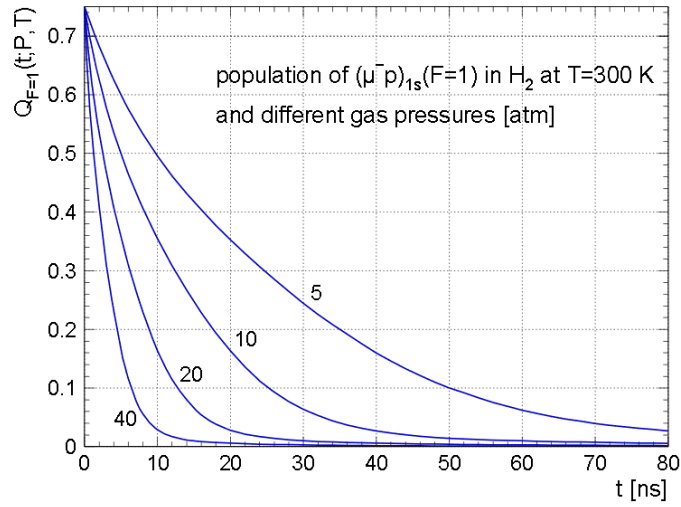


Fig. 3.4 Time evolution of the $\mu p^{F=1}$ population over time at different pressures but fixed temperature [12].

formation rate (Λ_{pd}) depends on the gas temperature [71].

After t_0 all the μps are thermalized and the μp disappearance rate depends, not only on the muon decay and nuclear capture rates (λ_0) but on the transferring to H_2 , deuterium and oxygen:

$$\lambda_{dis} = \lambda_0 + \phi(c_p \Lambda_{pp\mu} + c_d \Lambda_{pd} + c_o \Lambda_{pO}), \quad (3.2)$$

where ϕ is the gas density, liquid nitrogen number density (LHD) unit ($N_0 = 4.25 \times 10^{22} \text{ cm}^{-3}$) normalized, and c_p , c_d and c_o are the hydrogen, deuterium and oxygen concentrations in the total gas:

$$\phi = \frac{pN_a}{RTN_0}, \quad c_p = N_p/N_{tot}, \quad c_d = N_d/N_{tot}, \quad c_o = N_o/N_{tot}, \quad (3.3)$$

with N_a the Avogadro number, $N_{tot} = N_p + N_d + N_o$ and $c_p + c_d + c_o = 1$. A simulation of how the μp population versus time at different oxygen concentrations is shown in Fig. 3.5.

The parameters of equation 3.2 depend on the composition, temperature and pressure of the gas. The values $\lambda_0 = (4665.01 \pm 0.14) \times 10^{-1} \text{ s}^{-1}$, $\Lambda_{pp\mu} = 2.01 \times 10^6 \text{ s}^{-1}$ and $\Lambda_{pd} = 1.64 \times 10^{10} \text{ s}^{-1}$ can be found in literature and theoretical calculations, respectively in [37] and [38], [37], and [39].

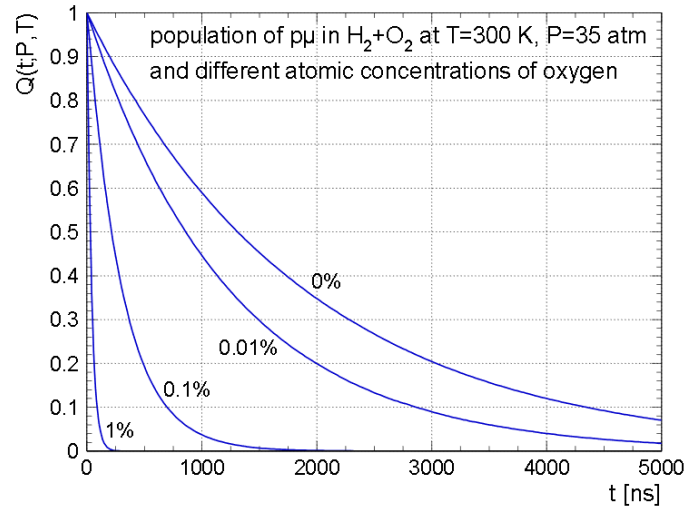


Fig. 3.5 Time evolution of the μp population, after the thermalization ends, over time at different oxygen concentration but fixed temperature and pressure [12].

The variation in the number of muonic hydrogen $N_{\mu p}$ in the thermalized phase is thus:

$$dN_{\mu p}(t) = S(t)dt - N_{\mu p}(t)\lambda_{dis}dt, \quad (3.4)$$

where $S(t)$ is the number of generated μp that after the prompt phase, it is 0. By solving the differential equation 3.4, we have:

$$N_{\mu p}(t) = N_{\mu p}(0)e^{-\lambda_{dis}t}, \quad (3.5)$$

where $N_{\mu p}(0)$ is the number of muonic hydrogen at the end of the thermalization phase. The variation in the number of muonic oxygen over time is:

$$dN_{pO}(t) = c_o\Lambda_{pO}N_{\mu p}(t)dt, \quad (3.6)$$

thus, we obtain:

$$dN_{pO}(t) = c_o\Lambda_{pO}N_{\mu p}(0)e^{-\lambda_{dis}t}dt. \quad (3.7)$$

A fit of the oxygen X-rays time evolution can be performed by numerically integrate the equation 3.7 leaving Λ_{pO} as free parameter.

Laser phase

Finally, a pulsed middle infra red (MIR) laser is used to excite the spin-flip transition resulting in an increase in the transfer thus, in the X-rays emission.

Calculations on the induced probability of spin-flip transition by a laser source were performed in [72] and reported as follows. If the μp is stimulated by an external oscillating magnetic field (with frequency ν), $B(t) = \cos 2\pi\nu t$ the transition matrix is:

$$\begin{aligned} & \langle \mu p(1S)^{F'=1} | -e\hbar \cos(2\pi\nu t) \left(\frac{\mu_p}{m_p} B_0 S_P - \frac{\mu_\mu}{m_\mu} B_0 s_\mu \right) | \mu p(1S)^{F=0} \rangle \\ & = -\frac{e\hbar}{2} \cos(2\pi\nu t) \left[\frac{\mu_p}{m_p} + \frac{\mu_\mu}{m_\mu} \right] |B_0|, \end{aligned} \quad (3.8)$$

with $\hbar S_P$ and $\hbar s_\mu$ denote the proton and muon spin operator with magnetic moment μ_p and μ_μ expressed in units $e\hbar/(2m_p)$ and $e\hbar/(2m_\mu)$. The probability per unit of time of the transition is:

$$dP(\nu, \nu_0)/dt = \frac{1}{\hbar^2} (\mu_B |B_0|)^2 \left[\frac{\mu_p}{m_p} + \frac{\mu_\mu}{m_\mu} \right]^2 \delta(\nu - \nu_0), \quad (3.9)$$

where μ_B is the Bohr magneton and ν_0 the spin-flip transition resonance frequency. Due to the Doppler effect, the probability distribution (ρ_D) around the rest $\bar{\nu}_0 = \Delta E^{hfs}/h$ is not a delta, but:

$$\rho_D(\nu_0) = \frac{1}{\sigma_D \sqrt{2\pi}} e^{-\frac{(\nu_0 - \bar{\nu}_0)^2}{2\sigma_D^2}} \quad (3.10)$$

with:

$$\sigma_D = \bar{\nu}_0 \cdot \sqrt{\frac{kT}{(m_p + m_\nu)c^2}}. \quad (3.11)$$

Taking into account a laser line width $\rho_L(\nu)$, the observable transition probability per unit of time becomes the product of the two distributions:

$$\frac{d\bar{P}}{dt} = \int d\nu_0 \rho_D(\nu_0) \int d\nu \rho_L(\nu) \frac{dP}{dt}(\nu, \nu_0). \quad (3.12)$$

The interesting situation is when $\sigma_L \ll \sigma_D$ and the laser is tuned at the resonance frequency, obtaining:

$$\frac{d\bar{P}}{dt} \simeq \sqrt{\frac{(m_p + m_\mu)c^2}{s\pi kT\bar{v}_0^2} \left[\frac{\mu_B}{h} \left(\frac{m_e}{m_p} \mu_p + \frac{m_e}{m_\mu} \mu_\mu \right) \right]^2} |B_0|^2, \quad (3.13)$$

where k and T are the Boltzman constant and the gas temperature.

We can express the square modulus of B_0 as function of the energy flux average $|\bar{F}| = c/(2\mu_0) \cdot |B_0|^2$ carried by the electromagnetic field. μ_0 is the vacuum magnetic permeability. Now, integrating the equation 3.13 over a laser pulse duration τ we obtain:

$$\bar{P} = \frac{\mu_0 \mu_B^2}{\hbar^2 c^2 \bar{v}_0} \sqrt{\frac{(m_p + m_\mu)c^2}{2\pi kT}} \left(\frac{m_e}{m_p} \mu_p + \frac{m_e}{m_\mu} \mu_\mu \right) |\bar{F}| \tau. \quad (3.14)$$

We can express the energy flux as function of the laser energy output E divided by the multiplication between the cross section S and the time duration of the laser beam τ : $|\bar{F}| = E/(S\tau)$ and replacing it in the last equation. By replacing the constants in equation 3.14 with the numerical values, we have:

$$\bar{P} \approx 2 \times 10^{-5} \frac{E}{S\sqrt{T}}, \quad (3.15)$$

with E expressed in J, S in m^2 and T in K.

The idea is to do a difference measure with and without the laser pulse, normalizing the two measures with the muon flux. In order to find the right laser frequency, a scan is needed. The laser scan cycle must take into account the time required in order to accumulate enough statistics thus, to have a reliable measurement.

Chapter 4

The apparatus

In this chapter, all the experimental apparatus is discussed.

From the previous chapter, where the FAMU strategy is shown, we can deduce the experimental necessities to achieve a reliable $\Delta E_{\mu p}^{hfs}(1S)$ measurement, briefly recalled here: we want to study the X-rays time evolution of muonic oxygen after a laser pulse. These X-rays are related to the amount of muonic hydrogen (in the ground state) in which the laser excites the hyperfine transition ($F=0 \rightarrow F=1$).

Muonic hydrogen is the main actor in this experiment. We want as much μps as possible in order to increase the process statistics thus, reduce the beam time for each tested laser frequency. So, a high intensity, negative muon source is needed. Due to the gaseous nature of hydrogen, muons must have low energy to be stopped into it.

The ideal situation is to shoot the laser when all the muonic hydrogen atoms are thermalized. The mechanisms involved in this measurement show a precise time dependency right after the muonic hydrogen formation. Thus, the muon beam has to be pulsed with sufficient time between two successive pulses.

A beam monitor is needed in order to measure the number of muons interacting with the gaseous target that can be used as a normalization factor of every single measure.

The muonic transfer mechanism is strictly related to the gas energy or in other words, temperature. In order to study this effect, the tested gas must be kept at different pressures and temperatures (precisely measured), thus we put a lot of effort into the designing and testing of a custom cryogenic target.

The probability of spin-flip transition when a photon hits a μp is quite low so, in order to increase the number of light- μp interaction, an optical cavity is needed and must be hosted inside the cryogenic target. A parallel effort has to be put in order to have enough photons. There are no commercial, pulsed MIR laser with sufficient power so we developed a totally custom, high power, still tunable MIR laser.

As mentioned already, earlier in the dissertation, we want to measure the muonic oxygen X-rays emission with both high timing and energy resolution, thus a custom detection system was developed.

4.1 Muon source

There are several muon accelerators but only a few of them fit with the FAMU experimental necessities: high intensity, low energy, negative muon beam with a pulsed time distribution.

Riken-RAL muon facility at ISIS fits all the experimental necessities. ISIS neutron and muon source is a world-leading centre for research in the physical and life sciences at the STFC Rutherford Appleton Laboratory near Oxford in the United Kingdom [13]. It makes available to hundreds of scientists per year, seven different muon beamlines, four of them were made by a joint agreement between the Japanese RIKEN (The Institute of physical and chemical research) and the British Rutherford Appleton Laboratory (RAL) itself. These four beamlines are therefore called RIKEN-RAL (Fig. 4.1).

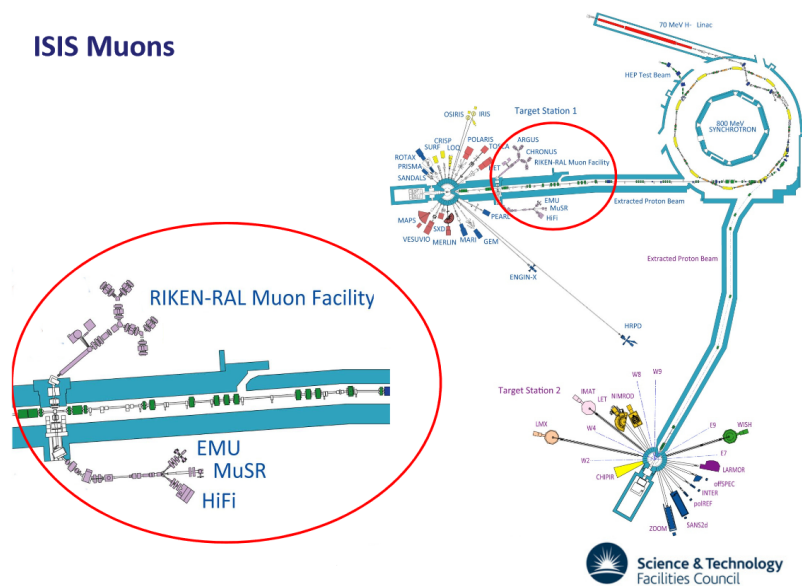


Fig. 4.1 ISIS neutron and muon source schematic. The synchrotron accelerated protons are split in 2 target station (TS). In TS1 are hosted the muon beamlines, a particular of these beamlines is shown in the enlarged red circle [13].

ISIS muon source core is a high intensity and rapid cycling proton synchrotron. It produces a double 800 MeV proton pulse with a repetition rate of 50 Hz. Each pulse has 70 ns width and it is separated by the former one by 320 ns. The total current is $170 \mu\text{A}$ [14]. The pion graphite production target is shared by all the

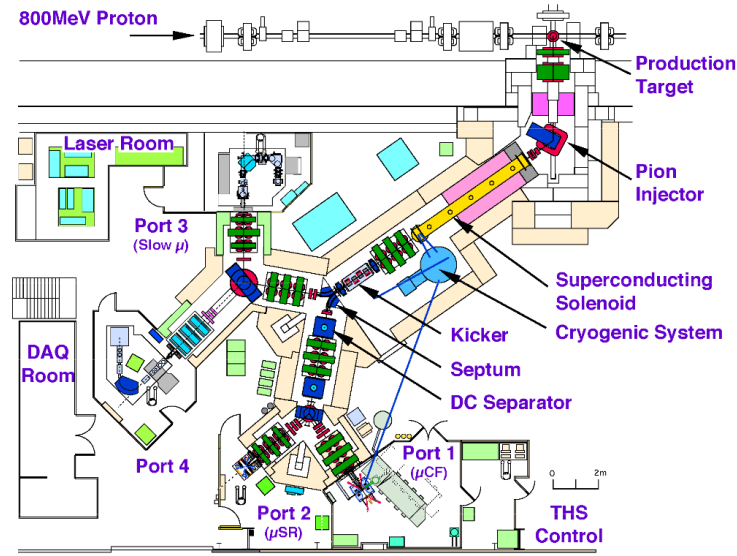


Fig. 4.2 The four ports scheme of the RIKEN-RAL muon facility. Each muon production and delivery element position is indicated

beamlines and for the RIKEN-RAL ones is followed by a couple of momentum analysing and selecting quadrupole magnets. Right after these two elements, a Cherenkov detector is placed in order to provide the timing trigger for the experiments. Pions are then transported to the decay section inside a superconducting solenoid magnet where they convert to muons by $\pi \rightarrow \mu$ decay in flight. The decay muons are introduced into the muon extraction system and, by using a kicker and a septum magnet, they can be delivered simultaneously to a double leg beamline. Each leg feeds 2 different ports. It should be noticed that without changing the cable connections for the kicker magnet the two legs are fed simultaneously with opposite polarities muons. In order to remove the e^+/e^- contamination from the pion decay, several electronic separators are placed in the beamline [73]. A schematic but detailed view of the system is in Fig. 4.2.

The final beam size (at the port level) is of about 10 cm^2 with a selectable momentum in the $20 \text{ MeV}/c$ to $120 \text{ MeV}/c$ range, with an associated selection error $\Delta p/p=10\%$ [73]. In each port, a lead duct collimates the beam to the final cross dimension of 4 cm^2 . The proton double pulse time structure is maintained in the muon beam time distribution, as shown in Fig. 4.3. The typical intensities vary in respect of the muon momentum and polarity (see Fig. 4.4). As predicted by the theory (see section 1.3), for the decay channel, μ^+ yield is higher than for μ^- .

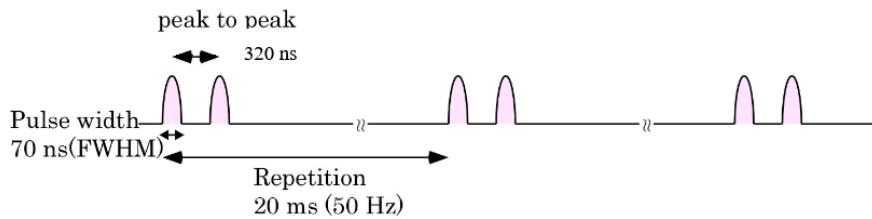


Fig. 4.3 RIKEN-RAL muon beam time distribution

Increasing the momentum, the number of produced muons increases, for example going from 20 MeV/c to 80 MeV/c it results in a factor 100 of increasing in the muon production yield.

For FAMU's purposes, negative decay muons in the 40-80 MeV/c are required.

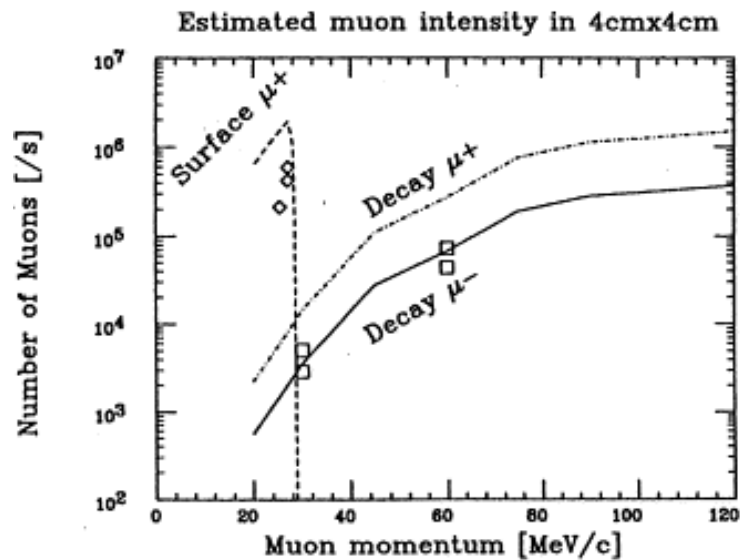


Fig. 4.4 Predicted intensities for positive and negative muons both from the decay channel and surface (only for μ^+). It worth nothing to notice the increase in number of muons in respect of the chosen momentum [14].

For the first phases of the FAMU experiment (2013-2016), port 4 was used but the last measurements took place at port 1 that is the only one able to host the laser system. Port 1 was used in the past to host a muon catalysed fusion experiment and left unused for some years. Soon after a commissioning phase (2017), to verify the magnets operation and thus the beam quality, it was set for the FAMU experiment. Fig. 4.2 shows in detail the two ports position, moreover in Fig. 4.5 the magnetic

field (inside the beamline) obtained with the simulation software TURTLE and the magnets positions and currents.

4.2 Beam monitor

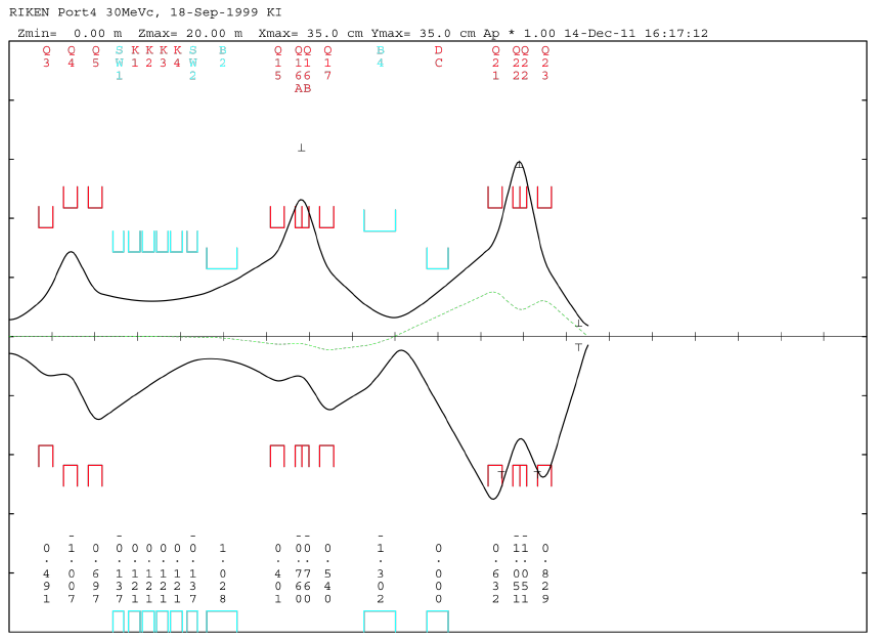
Measuring the number of muons interacting with the target, beam pulse per beam pulse, is essential to precisely normalise each measurement. Moreover, being able to visualise the beam focusing and steering, is essential as well, in particular during the commissioning phase. The FAMU collaboration¹ developed a hodoscope made by plastic scintillator fibres coupled with silicon photomultipliers (SiPM). The fibres are organized in two perpendicular crossing planes (X-Y), placed orthogonal to the beam duct, in a 32+32 configuration with 1 mm pitch, resulting in a final active area of 32 mm² [15].

The plastic scintillator fibres consist of a polystyrene-based core and a PMMA (polymethylmethacrylate C₅H₈O₂) cladding. External EMA (Extra Mural Absorber) is used to avoid optical crosstalk. They are produced by the French Saint Gobain and the model is BCF-12. They emit 435 nm blue light when hit by a crossing particle, the decay time is 3.2 ns and the absorption length is 2.7 m. The light production is ~ 8000 photons per MeV.

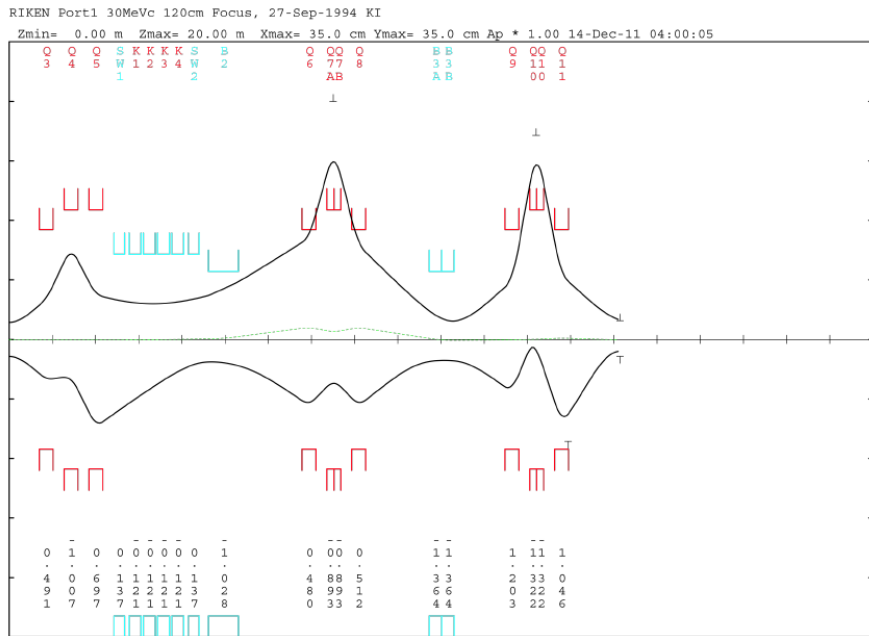
The SiPMs are made by Avansid, RGB model, with 1 mm² of area and 40 μm^2 single cell dimension. They match the BCF-12 fiber peak emission (PDE $\sim 22\%$ at ~ 440 nm, with 4 V overvoltage). Moreover, their low operating voltage ($V_{brk} \sim 29V$), their small breakdown voltage dependence from temperature ($\sim 27mV/C$) and their low dark noise made them the right choice for this instrument [15]. Characterization and selection of 64 SiPMs ensured that the differences in terms of temperature dependence and operating voltage were reduced (Fig. 4.6). It was thus possible, to use a common voltage for biasing each detection plane.

As the SiPM's footprint is slightly bigger than the fibre cross-section, fibres must be read alternating left/right and up/down sides. Thus, they are arranged in the four sides of the hodoscope in four groups of 16 fibres each. A flat cable connects the SiPMs output to a cable distribution board in which the main MCX connectors are hosted (Fig. 4.7 a and Fig. 4.7 b). The bare output signal is digitized without any kind of amplification.

¹In particular, the Milano Bicocca and Pavia INFN sections



(a) Port 4 beam profile and magnet position.



(b) Port 1 beam profile and magnet position.

Fig. 4.5 Port 4 and Port 1 magnetic field profiles obtained with the TURTLE beam simulation software. The magnets names are on the top while the set currents are on the bottom of each figure.

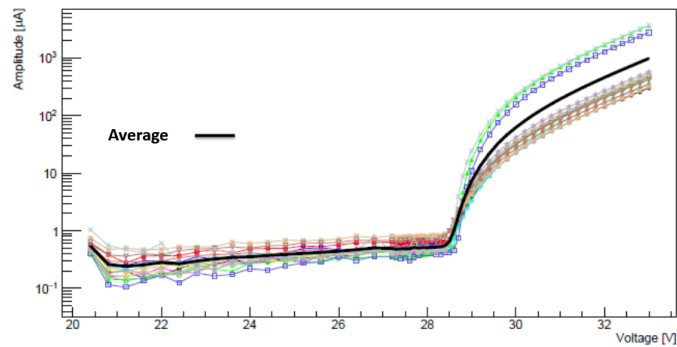
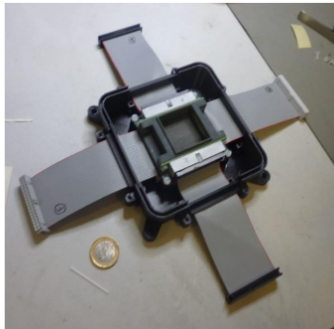
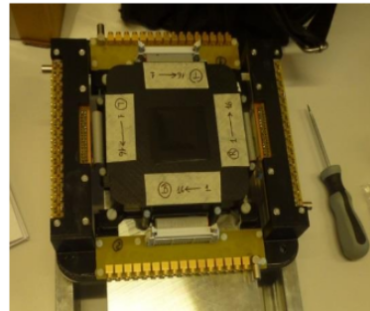


Fig. 4.6 Reverse current-voltage characteristics of the 64 SiPMs mounted on the hodoscope. The response is quite similar [15]



(a) Hodoscope mounting: in the centre the active area and the 4 flat cables connect 16 SiPMs each.



(b) Final mounting of the hodoscope. The MCX connectors connect the SiPMs signal directly to the data acquisition system.

Fig. 4.7 Hodoscope mounting [15]

The passive materials in the active area needed to host the entire system and block the visible light (that produces the signal in SiPM) have as minimum thickness as possible to barely interact with the muon beam (i.e. 1 mm PLA).

The output voltage of each detector is digitised. The typical minimum ionising particle (MIP) signal has an amplitude of 40 mV, with a signal to noise ratio bigger than 10. To extract the information on the muon beam shape and flux, the entire waveform over a certain threshold is integrated, fibre by fibre. This threshold is set high enough in order to avoid electronic noise integration. In Fig. 4.8, the acquired waveform and the integration threshold are shown. The double peak shape reflects

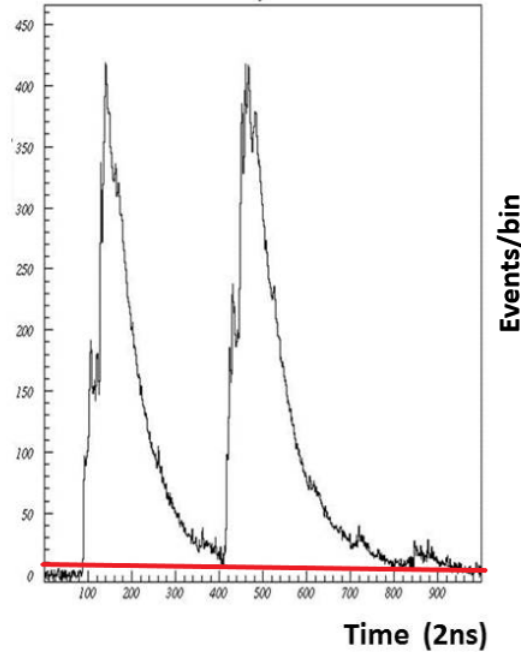


Fig. 4.8 Digitized hodoscope waveform of single fibre, the integration threshold is shown in red [15].

the RIKEN-RAL muon beam time distribution confirming the 70 ns single pulse duration spaced by 320 ns in between.

Cosmic rays were used to calibrate the instrument. The cosmic muons mean energy is greater than 1 GeV thus they interact with matter as a MIP. In the energy region of interest for our experiment (30-80 MeV/c), muons no longer behave as MIPS so a conversion parameter is needed. In reference [74] it is possible to find lists of stopping power (dE/dx) for different materials at different energies. Using the value for polystyrene in the relation:

$$\mu/s = f \times Q(p)/Q(\text{cosmics}) \times (dE/dx)_{\text{cosmics}}/(dE/dx)_p \quad (4.1)$$

where f is the beam frequency, $Q(p)$ is the total charge during the beam measurements and $Q(\text{cosmics})$ the one acquired with cosmic rays we extrapolated the total muon flux (Fig. 4.9) that is in good agreement with the expected one (Fig. 4.4).

Finally, the integrated charge of each fibre can be mapped in a 2D matrix showing the beam profile and its spatial distribution. This kind of measurements was particularly useful during the port 1 commissioning phase. Changing the magnets

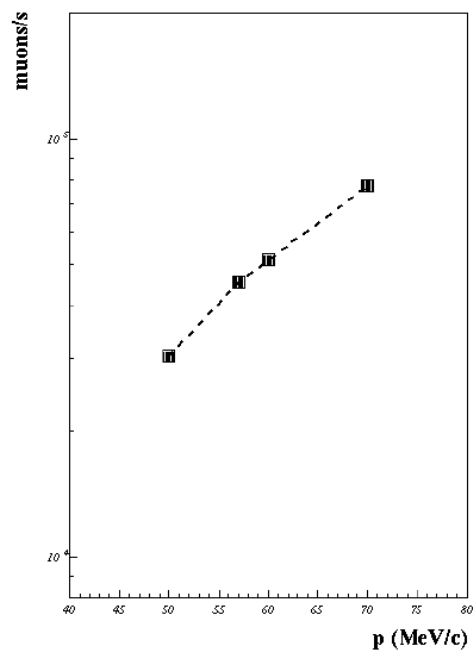
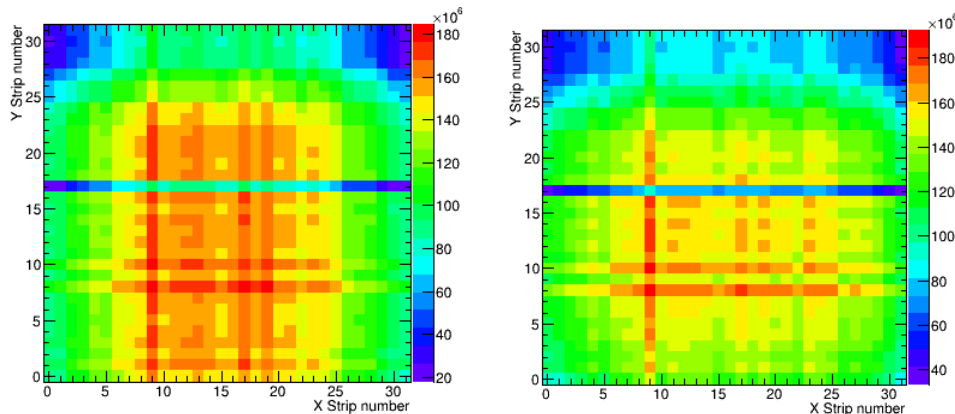


Fig. 4.9 Measured muon flux of the RIKEN-RAL muon beam at port 1. The filled boxes are calculated using the equation 4.1 and are in good agreement with the expected flux Fig. 4.4 [16].



(a) 2D map with the port 1 Q11 magnet current decreased of 20 A. (b) 2D map with the port 1 Q11 magnet current increased of 10 A.

Fig. 4.10 Hodoscope 2D map of the integrated charge. The Q11 magnet position is shown in Fig. 4.5. One fibre defect is clearly visible.

current, the beam steering is modified and by tuning each parameter we were able to achieve the best beam focusing. In Fig. 4.10, two muon beam profiles are shown. They were acquired during the port 1 commissioning phase in early 2017.

4.3 Cryogenic target

The muon to oxygen transfer mechanism shows a sharp energy dependence (see 1.7). A detailed study at different temperatures, pressures and O₂ concentration is needed to verify experimentally the theoretical models. Thus, a custom, purpose dedicated cryogenic gas target was developed. The requisites of this development are essentially:

- to be as transparent as possible for muons and X-rays;
- the capability to safely held pressures up to 40 atm;
- to be pure hydrogen safe;
- the ability to work and keep stable temperatures in the 50–300 K;
- to maximize the solid angle covered by X-rays detectors.

The first point is quite obvious: minimizing the walls thickness is mandatory to avoid muon capture (reducing the number of muons able to produce muonic

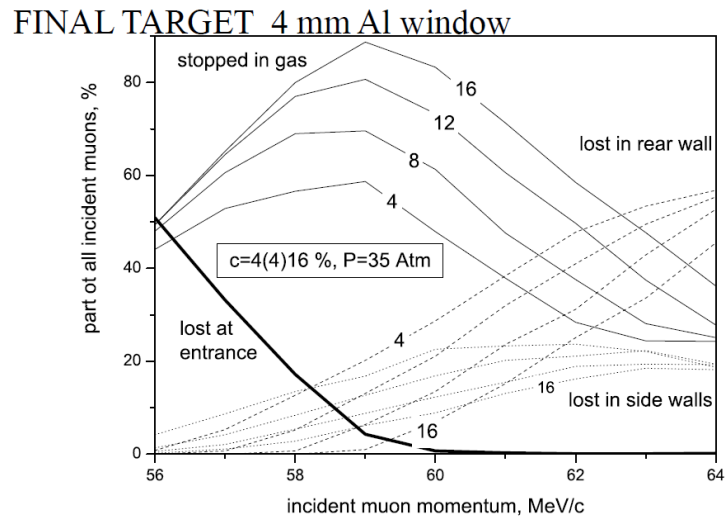


Fig. 4.11 FAMU GEANT4 simulation of the muon distribution stopped into the gas at 57 MeV/c. The different lines represent different CO₂ concentration in hydrogen target [17].

hydrogen) and X-rays absorption.

These requisites drove the development of the 2016 target and, chosen the operative conditions and taking in mind the necessity to host the optical cavity, are driving the final target design.

4.3.1 2014 design

The 2014 target design and operation are described here even though it was not devoted to a proper study of the transfer rate at different energies. The aim was to study the response of the detectors in the RIKEN-RAL muon port environment (signal to noise ratio), attempting to measure the muon transfer rate only at room temperature.

After a set of Montecarlo simulations, mainly to investigate where and how likely muons stop in the gas and/or in its container (Fig. 4.11), the design was fixed and sent to Criotec Impianti S.r.l. in order to build it. The target is made of an aluminium cylindrical vessel, in particular, the Aluminum alloy Al6061. It is a cylinder of 125 mm of base diameter and 260 mm length, with an inner volume of 2.8 litres. The thickness of the walls is 7 mm, except for a circular front face of 44 mm diameter with the entrance window, thinned to 4 mm [17]. This shape and dimensions ensure

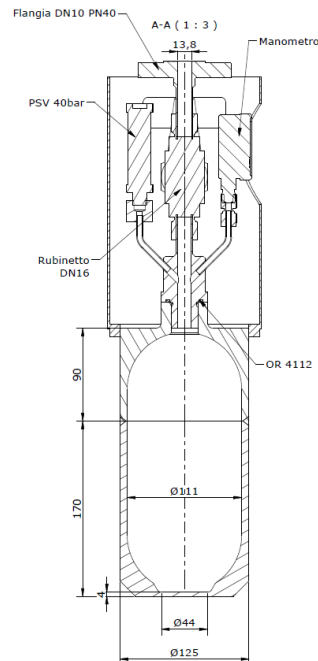


Fig. 4.12 2014 target design with all the dimensions in mm. On top the gas feeding system is shown as well.

a perfect and certified resistance to a gas pressure of several tenths of bar and minimize the divergence of the muon beam due to multiple scattering [17]. A detailed scheme is in Fig. 4.12.

4.3.2 2016 design

In order to precisely study the energy dependence of the transfer rate, a more refined target design was needed.

We designed a new Al6061 double volume, one inside the other, vessel. The vacuum between these two volumes provides proper thermal insulation. From the muons' point of view, they cross a first 0.8 mm thick Al entrance window entering the evacuated volume. In order to thermally screen the inner pressurized shell from the heat coming from this very thin entrance window, a set of three 0.1 mm thick aluminium disks separated by 0.1 mm fibreglass ring spacers is placed (Fig. 4.14(a)). After crossing this aluminium-fibreglass "sandwich", muons pass through a second 2.8 Al entrance window finally entering into the tested gas volume. The inner

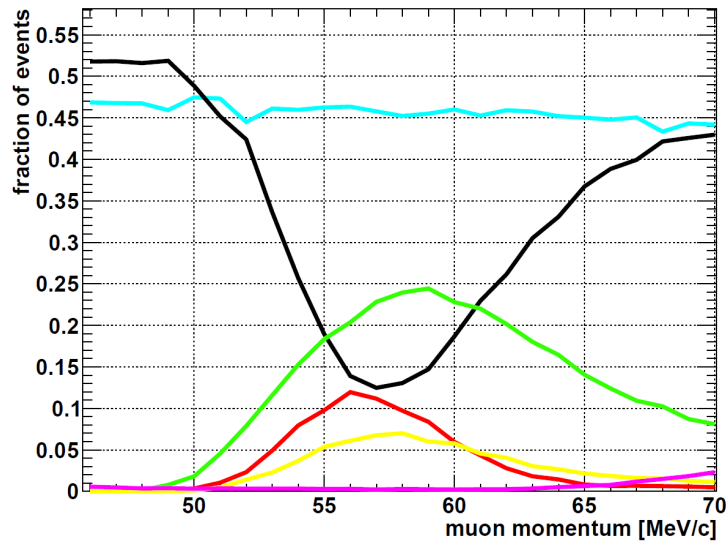


Fig. 4.15 FAMU GEANT4 simulation of the muons stopped fraction into the different volume of the target: green line for the tested gas, black for the aluminium walls, cyan for the lead collimator, yellow and pink for respectively the gold and nickel coatings and red for other materials. At 57 MeV/c the number of muons stopped into the gas is maximized. [18].

simulations take into account not only the geometrical physical dimensions but also the constituent materials, according to the technical specifications provided by the producer, Criotec Impianti S.r.l..

The FAMU GEANT4 simulation geometry reproduces the whole setup, put in the World GEANT4 volume filled with air. The FTFP BERT 2.0 physics list with initial seeds (1,2) and PIXE model activated is used in all simulations. The muon beam was simulated according to the beam specifications, i.e. with a circular shape of 4 cm diameter, a divergence of 60 mrad at the exit of the beam pipe and a momentum spread of 10% [18]. Several runs of the simulation with different initial muon momenta allow us to tune the muon beam momentum to the best value. In Fig. 4.15 the simulation shows that in order to maximize the muons stopping into the gas target, a momentum of 57 MeV/c must be chosen.

Moreover, the simulation was also used to study the spatial distribution of the muon stop in the gas, in order to optimize the detector placement along the target axis (as shown in Fig. 4.16).

In order to cool down the target, a single-stage cryogenic refrigerator operating on the Gifford-McMahon cycle. We chose a Sumitomo CH-104 cold head, it

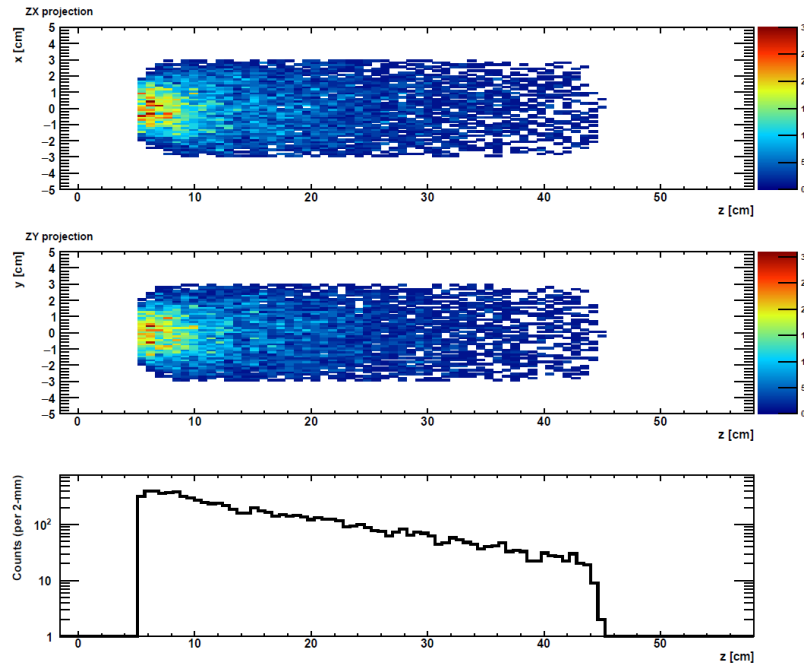


Fig. 4.16 FAMU simulation of the muon distribution stopped into the gas at 57 MeV/c. Top panel: ZX projection. Middle panel: ZY projection. Bottom panel: muons stop distribution along Z axis [18].

uses helium as expansion and compression gas to produce low temperatures. A valve motor drives the rotating valve disk that controls the helium gas flow. The high-pressure gas drives the reciprocating displacer assembly within the cylinder housing. Ports in the valve disk allow two complete cycles of the displacer for every revolution of the valve disk. The helium compressor used in the FAMU experiment is a Sumimoto model HC-4E1. This compressor is single-stage, water cooled, rotary and is designed to deliver high pressure, oil-free helium gas to the cryogenic refrigeration system. To dissipate the heat generated by the cold head and the compressor, an external water chiller, made available by the ISIS staff was used.

In order to monitor and control the temperature, four thermometers, based on DT-670 silicon diodes are integrated into the system: two on the cold head (T_B and T_D) and two at the ends of the inner cylinder (T_A and T_C). They are connected to a Lakeshore 336 temperature controller that is used for a real-time reading and to set the target temperature. In particular, T_B was set as the leading temperature of the PID system. When a temperature step is reached, the cold head is switched off and

if necessary, a resistive heater (up to 100 W) is switched on.

The performances of the system were evaluated both in our laboratories and during the data takings at RAL.

The cold head reaches, from room temperature, a temperature of 40 K in about 2.5 hours. It goes down to 28 K in a total of 3.1 hours and stabilizes to its steady-state equilibrium of 27.7 K in 4-4.5 hours, showing for the next hours good stability (less than about 0.06 K/h of drift). The target follows this trend with a time delay due to its thermal capacitance: it goes below 40 K in 2.7 hours, reaching 31K in 3h. The inner cylinder stabilizes around 30.5 K (T_A) and 31.0 K (T_C) respectively for a final average equilibrium temperature of 30.75 K with a 40 minutes delay in respect with the cold head. A drift of only 0.01 K/h was observed. Due to the good stability of the system, coupled with the constant recording of each sensor, we conservatively assume a temperature variation on the order of 1% as acceptable for our measurements (e.g. 250 K set on as the temperature we want to investigate. The measure could start when the target average temperature is within 2.5 K of the set value) [18].

About the vacuum between the two shells, the system reaches the 10^{-5} - 10^{-6} mbar vacuum range and, even once the thermo-vacuum pump is disconnected, the target keeps this vacuum level for several days.

The target filling process must be done at the environment temperature and by successive steps, the gas is cooled down to the target temperature. For each temperature step, a total of 3 hours of data were acquired. In Fig. 4.17 the entire cycle for the $H_2O_2(0.3\%)$ gas mixture is shown. In blue, the cold head temperature, in green the target one and in magenta the percentage power of the heater.

4.4 Laser system

The laser is one of the core system of the project. The main requisites of the system are:

- Pulse energy: > 1.5 mJ;
- Central wavelength: $\lambda = 6785$ nm;
- Line width: $\Delta\lambda = 0.070$ nm (450 MHz);

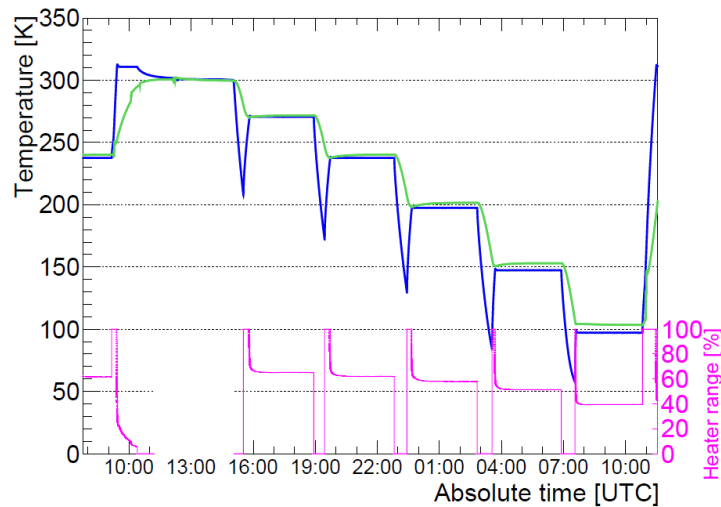


Fig. 4.17 FAMU2016 temperature cycle for the $\text{H}_2\text{O}_2(0.3\%)$ gas mixture. In blue, the cold head temperature, in green the target one and in magenta the percentage power of the heater [18].

- Tune range: 6785 ± 3 nm:
- Tune step: 0.030 nm (200 MHz);
- Repetition rate: 25 Hz.

A commercial MIR laser with these characteristics doesn't exist thus, we are designing a completely custom laser system. For the requested wavelength range there are two possible laser sources: quantum cascade lasers and by using non-linear optics schemes. The first approach lacks in energy thus, we decided to develop a light source based on difference-frequency generation (DFG) using different non-linear crystals. In DFG, the combination of two laser beams in a non-linear crystal can generate another beam with the difference of the optical frequencies of the pump beams. In our design, the pulses of a neodymium-doped yttrium aluminium garnet (Nd:YAG, INNOLAS SplitLight Hybrid²) laser ($1.064 \mu\text{m}$) are combined with the amplified pulses at $\sim 1262 \mu\text{m}$ of a chromium-doped forsterite (Cr:forsterite, LOTIS TII LT-2212A) laser through a dichroic mirror and sent to the non-linear crystal to produce a MIR pulse at $6.785 \mu\text{m}$. In particular, the Nd:YAG is a q-switched single frequency laser with a fixed wavelength of 1064 nm with a line width between 0.34

²specification website: <https://www.innolas-laser.com/Products/Lamp-Pumped-Lasers/SpitLight-Standard.html>

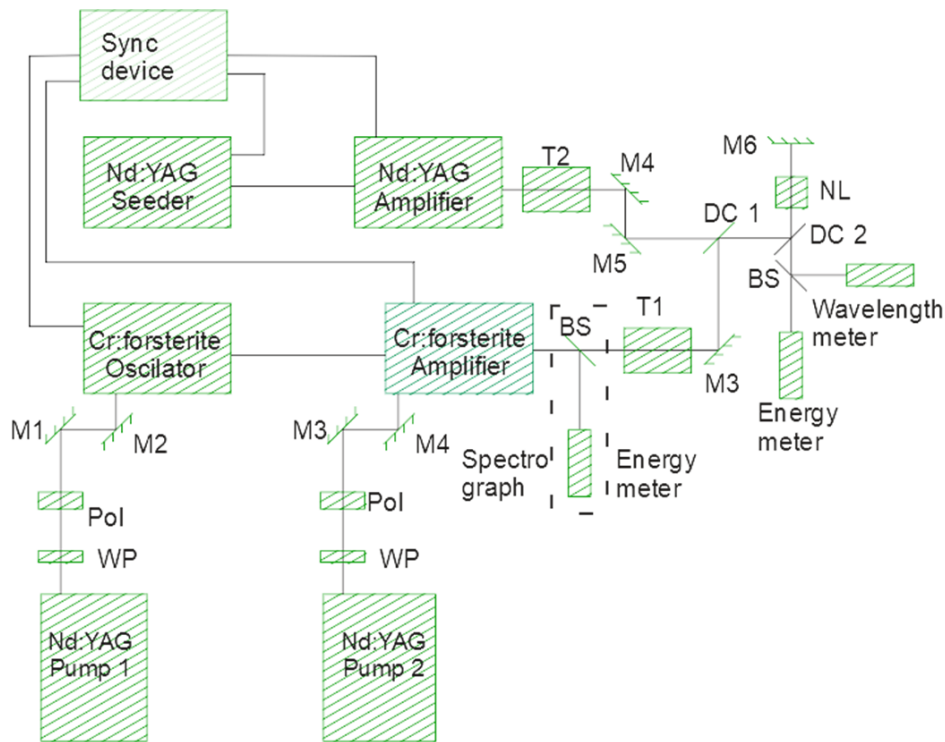


Fig. 4.18 FAMU DFG based laser system. Where WP - waveplate, PO - polarizer, M1–M5 - mirrors, T1 and T2 - telescopes, BS - beamsplitter, DC1 - dichroic mirror ($1.26 \mu\text{m}$ reflected and $1.06 \mu\text{m}$ transmitted), DC2 - dichroic mirror ($1.06 \mu\text{m}$ and $1.26 \mu\text{m}$ reflected and $6.76 \mu\text{m}$ transmitted) [19].

pm (90 MHz) and $0.11 \mu\text{m}$ (30 MHz), which produces 300 mJ of output energy. The Cr:forsterite oscillator-amplifier system, on the other hand, is a narrowband tunable laser from 1252 nm to 1272 nm with a maximum line width of 1 pm (188 MHz) with a total energy output around 25 mJ (if pumped with a 230 mJ 1064 nm source). The system scheme is shown in Fig. 4.18.

The Cr:forsterite tunability is operated inside the oscillator by a diffraction grating coupled with a two mirrors resonator as shown in Fig. 4.19.

The non-linear crystal is a key component in our design. This kind of artificial crystals is made to have different optical non-linearities which are due to a non-linear polarization. This phenomenon is based on the interaction and disappearing of two input photons at some angular frequency and, at the same time, the generation of the third one at a lower frequency. We tested a LiInS_2 non-linear crystal of dimension $7 \times 7 \times 20 \text{ mm}$ obtaining the preliminary output energy of $\approx 0.5 \text{ mJ}$ but it is expected up to 1.5 mJ after doing some extra modification related with the beam shape and

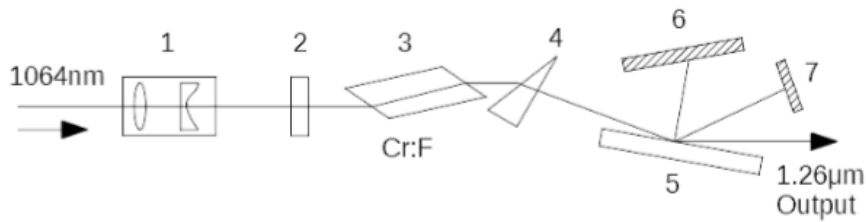


Fig. 4.19 Cr:forsterite oscillator scheme. Where 1 - decreasing telescope, 2 - entrance mirror (1.26 μm reflected and 1.06 μm transmitted), 3 - Cr:forsterite crystal, 4 - prism, 5 - diffraction grating, 6 and 7 - tuning mirrors of coupled resonator [19].

two pass configuration.

The total energy of the two input laser is 325 mJ that, for a beam diameter of 3.6 mm and a shoot duration of 12 ns, corresponds to $\approx 70 \text{ MW/cm}^2$ instantaneous power. The reason why we stepped down the input lasers intensity is the low crystal damage threshold, in fact, for most material with high non-linearity, it is below 50 MW/cm^2 . So far, we didn't perform a long term resistance sacrificial test.

We are investigating several solutions to this critical point like: use two crystals in a two passes set-up or/and acquire a crystal with larger cross section and higher damage threshold. For this last point, we ordered other crystals and the most promising seems to be BaGa_4Se_7 that could permit to achieve 5 mJ without further changes in the laser system.

Others criticalities are in the Cr:forsterite laser about the long term and shot to shot wavelength stability (mainly in the Nd:YAG pumping) thus, we need a real-time shot to shot wavelength measurement with proper accuracy in the 1.26 μm Cr:forsterite Nd:YAG pump. This measurement, after proper calibration and tuning, can be acquired and saved with the X-rays detector data and used in the further data analysis process.

We are putting parallel efforts into the Cr:forsterite power increasing, for instance cooling down the Cr:forsterite crystal and studying a multi-pass cavity to amplify the output power.

MIR light is easily absorbed by water vapour, as shown in Fig. 4.20 where the absorption of 4 meters of humid air (at room pressure and temperature with 60% of humidity) versus the wavenumber is shown. The wavenumber is defined as the wavelength reciprocal. Thus, particular attention has to be put in the laser delivery path design.

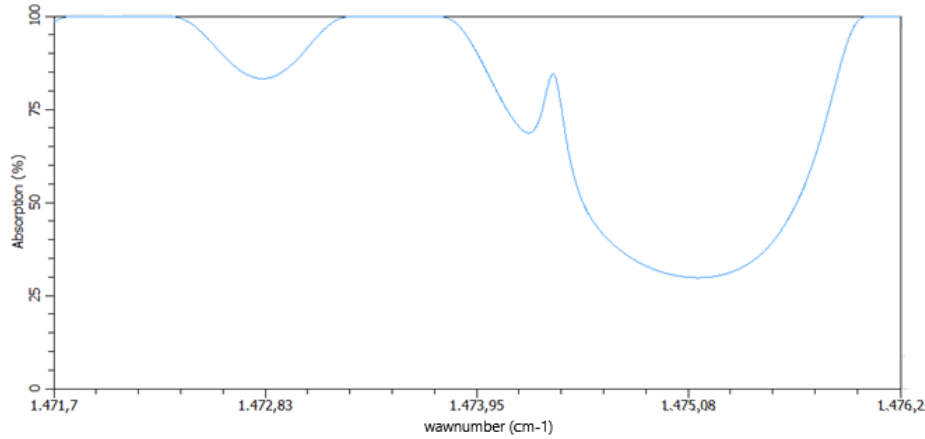


Fig. 4.20 4 meters humid air absorption versus the wavenumber at 300 K, 1 atm and 60% umidity. The hyperfine splitting expected energy is at $\approx 1473.8 \text{ cm}^{-1}$.

4.5 Optical cavity

The MIR laser light is sent inside the target in order to trigger the spin-flip transition in a volume filled with muonic hydrogen at the ground state. The transition probability depends on the laser energy per unit of surface (flux definition).

The laser beam has a small cross-section of 3.6 mm^2 while the target volume is of some cubic centimetres. There are two methods to fill the volume with light: diffusing the laser beam or using an optical cavity.

To explain the enhancement effect, we can take the equation 3.15 at a fixed temperature and express it as a function of the laser flux (D):

$$\bar{P} = \frac{\sigma_{SF}}{h\nu} D, \quad (4.2)$$

where $\sigma_{SF} = 6.58 \times 10^{-22} \text{ cm}^2$. We can replace ν with the proper laser frequency and calculate the minimum laser flux (D_{sat}) to have total probability equal to 1 (all the μ ps in the illuminated surface result spin-flipped) and obtain:

$$D_{sat} = \frac{h\nu}{\sigma_{SF}} = 4.47 \times 10^4, \quad (4.3)$$

expressed in mJ/cm^2 . This value denotes the maximum photon flux we must inject into the gas target without wasting a single photon interaction. This is an incredibly high value considering that for the proton radius experiment performed by the

CREMA collaboration, they had a $D_{sat} = 16.5 \text{ mJ/cm}^2$.

Now we can easily express the total transition probability as a function of the photon flux (D_{in}) we can provide to the muonic hydrogen:

$$\bar{P} = \frac{D_{in}}{D_{sat}}. \quad (4.4)$$

By diffusing the laser beam, D_{in} is the simple ratio between the laser energy (E), and the illuminated surface S_{ill} .

In order to virtually increase the light flux, an optical cavity will be positioned inside the target. Light confined between two mirrors (the cavity), reflects multiple times resulting in an increased total flux:

$$D_{in} = \frac{N_R E}{S_{ill}}, \quad (4.5)$$

where N_R is the number of reflections inside the cavity. Thus, the enhancement factor is equal to N_R .

As the previous formulae suggest, by reducing the illuminated surface and increasing the number of reflections inside the cavity, a reasonably high transition probability can be achieved. There are two problems in this simplistic point of view. The number of reflections depends on the mirror reflectivity that, even for high reflectivity mirrors, is less than one.

The other problem depends on the finite volume distribution of the generated μps inside the target (Fig. 4.16). μps are distributed in hydrogen, in a volume that depends on the muon beam cross-section and on its momentum. By using small cavities we can increase \bar{P} but reducing the total number of transitions at the point that the statistical fluctuations can mask the laser-induced transition effect.

We are investigating two different cavity designs:

- longitudinal, where the two mirrors are placed along the muon beam direction (Fig. 4.21);
- transversal, where the two mirrors are placed transversally to the muon beam direction (Fig. 4.22).

The mirrors sizes must be chosen to illuminate most of the μps without reducing too much the total transition probability.

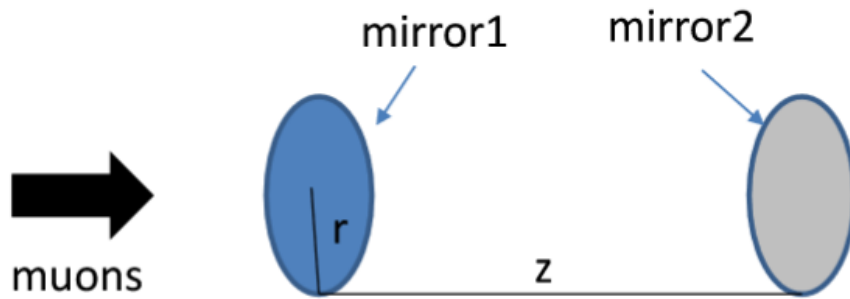


Fig. 4.21 Schematic view of a longitudinal optical cavity.

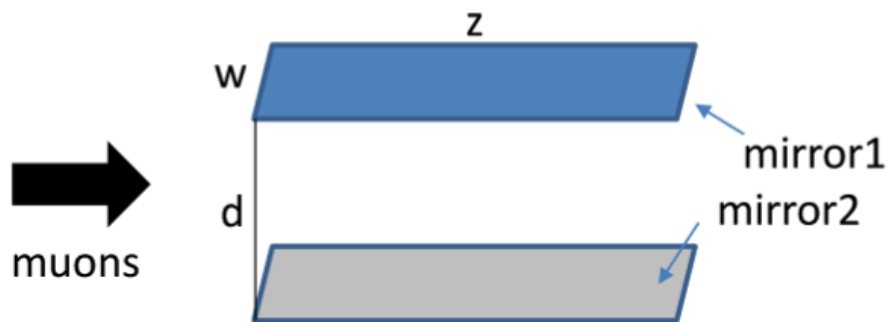


Fig. 4.22 Schematic view of a transversal optical cavity.

In this optimization process, we have to handle another parameter, the inter-mirror distance (d). In both the configurations, by increasing the inter-mirror distance, we can increase the illuminated volume without reducing the total probability. This is true if the illumination process can be considered instantaneous or much faster than the μ ps depopulation.

If we consider one thousand number of reflections, we can write the duration of the illumination process as a function of the inter-mirror distance:

$$\Delta T = \frac{1000 \times d}{c}, \quad (4.6)$$

with c speed of light. If we choose an inter-mirror distance of 5 cm, ΔT results to be ≈ 200 ns. Thus, the enhancement process is diluted in this time interval.

Furthermore, we have to remind that even for non-spin-flipped μ ps the muon can be transferred and produce muonic oxygen X-rays. Thus, we have to evaluate the signal to noise ratio, where "signal" is the difference between the number of muon transfer events from epithermal atoms (N_{SF}), spin-flipped by the laser, and the number of muon transfer event from thermalized atoms (N_0). The respective rates are λ_{SF} and λ_0 . With "noise" we consider the statistical fluctuations of the signal. In formula:

$$\rho(d, t) = \frac{\lambda_0 - \lambda_{SF}}{\sqrt{2n_T(0)\lambda_0\tau_0}} \frac{N(t)}{(1 - e^{-t/\tau_0})}, \quad (4.7)$$

in which, $n_T(0)$ is the number of μ p(1S) at the laser shot time ($t=0$), τ_0 is the muon decay time and $N(t)$ is the number of μ ps at a given time t . With a fixed surface and number of reflections, we can extrapolate the signal to noise ratio variation with time at different inter-mirror distances (Fig. 4.23).

The multi-parameters optimization process is still ongoing but we are converging on a transversal cavity design with 5x1.5 cm mirrors dimensions and an inter-mirrors distance of 5 cm. With a laser power of 1.5 mJ and 999 number of reflections, we can calculate the total enhanced flux: $D_{in} = 200$ mJ/cm².

4.6 X-rays detection system: LaBr₃

As stated before, the measurement is essentially based on the muonic oxygen X-rays time distribution detection. These high energy photons come from the muon

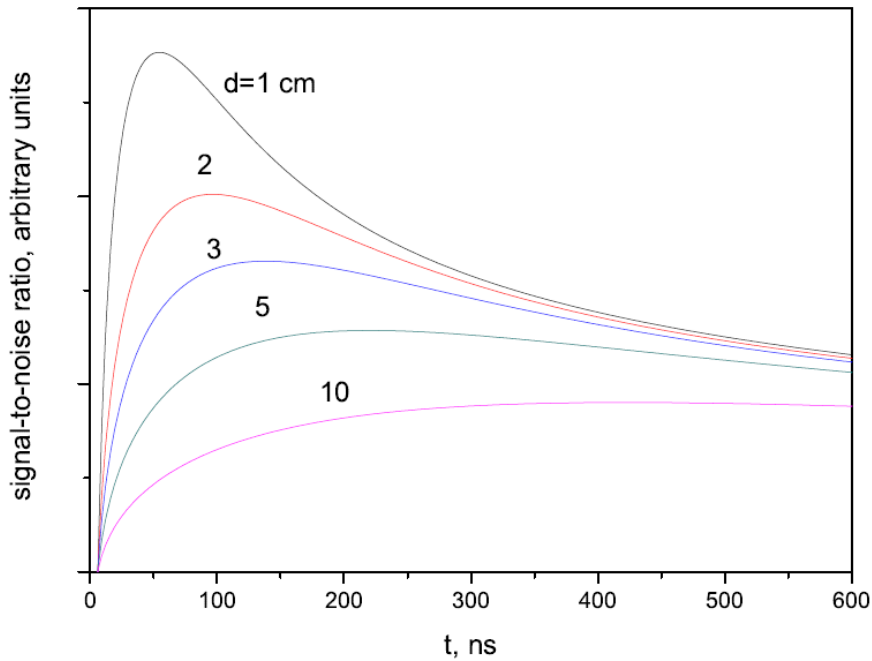


Fig. 4.23 Signal to noise ratio enhancement versus time for various inter-mirrors distances d

transferring from μp to the oxygen impurities inside the target. The transfer mechanism occurs in hundreds of nanoseconds thus, the detection system must be able to resolve X-rays, with a linear response along with all the process time window with good timing resolution. Moreover, due to the repetitive nature of the measurements, the detection efficiency must be as stable as possible during all the different phases. Multiple X-rays and electrons are generated due to the muon interaction with matter and its subsequent capture. Moreover, any accelerator facility has a high radiation background emission (with respect to the natural one). All these constitute the unwanted signal the detectors have to deal with or, in other words, what we can consider as "background" for our measurements. In order to clearly identify the muonic characteristic X-rays peaks, high energy resolution detectors are needed. During the "prompt phase" (see section 3), where muonic atoms are formed, a large number of X-rays and electrons are generated. The detector system has to face with a high flux of ionizing particles, remaining as linear as possible to deal with the subsequent delayed phase, when the muon transfer occurs. The duration of the signal generated by detectors must be as small as possible to reduce piled-up

events.

The X-rays emission by the target is isotropic thus, to maximize the X-rays collection and reduce the necessary beam time, we need to cover the maximum solid angle possible all around the target.

The necessary energy range spans from 100 keV (nitrogen and oxygen muonic lines) up to several hundreds of keV (muonic Al X-ray lines are up to ~ 450 keV as tabulated in Table 1.2).

To summarize, the detection system must fulfil these requirements:

- high energy resolution;
- good timing resolution;
- small signal duration;
- to be as linear as possible in pulsed high rate conditions;
- high efficiency in the 100-500 keV energy range;
- cover a large solid angle;
- good over time stability.

The small signal duration, with the good timing resolution, pushed us to consider a scintillation detector. To deal with the high energy X-rays with good energy resolution, the scintillator must be inorganic but fast. To fully exploit the scintillator timing characteristics, the device that reads the scintillation light must respond at least as fast as the scintillator itself. Photomultiplier (PMT) guarantees the timing specification preserving the energy resolution, and with proper cares, it can be used in high rate applications.

LaBr₃ characteristics

Scintillators were used in the last century for radiation detection [75] and in the last years, a new generation of cerium activated La-halide scintillators was proposed [76]. In particular, cerium doped tri-lanthanum bromide (LaBr₃(Ce)) crystals shown an extremely fast scintillation pulse (16 ns) and a record high energy resolution for the detection of γ -rays (2.8% FWHM at 662 keV) [77]. The light yield, that is the main contribution to the energy resolution, is 63 photons per keV (of the incident

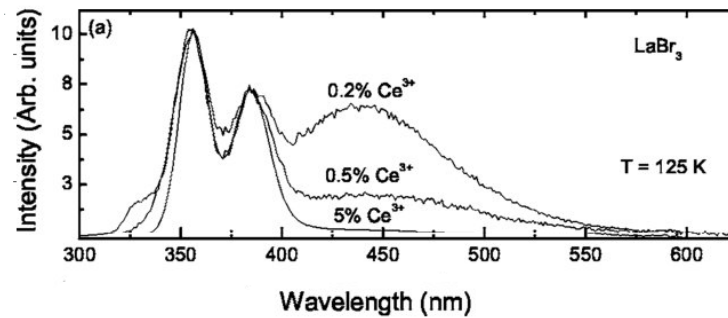


Fig. 4.24 LaBr₃ light emission. Three cerium dopant concentration are shown [20].

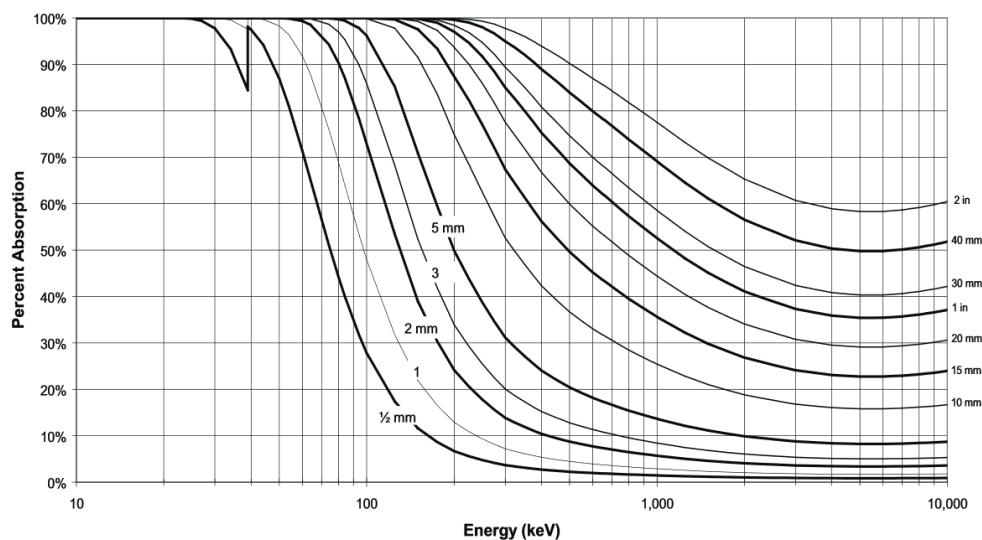
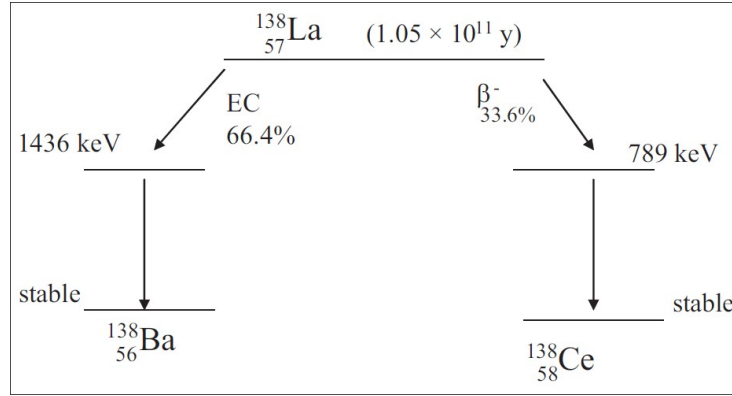


Fig. 4.25 Absorption versus incident photon energy for different crystal thickness [21].

γ -ray), 1.6 times bigger than classic thallium activated sodium iodide (NaI(Tl)), usually referred as standard in γ -rays spectrometry. The decay time constant is in the order of tens of ns and the light emission is peaked on 350-380 nm (Fig. 4.24). The duration of the decay constant depends on the amount of cerium in the crystal and on temperature but, in ordinary 5% dopant concentration is ~ 16 ns [20]. Its density of 5.08 g/cm^3 permits to achieve 50% of attenuation for 662 keV cesium 137 γ -rays within only 1.8 cm of thickness (Fig. 4.25).

However, it is hygroscopic so, particular attention must be paid in packaging to properly seal the crystal. In addition, it is not indicated for low background measurements due to its intrinsic radioactivity that results from the natural occurring ^{138}La and ^{227}Ac (in Fig. 4.26 the decay scheme). ^{138}La (0.09% abundance)

Fig. 4.26 ¹³⁸La decay scheme[22].

produces two γ -rays of 788.7 keV and 1435.8 keV. There are also barium K X-rays from 31 up to 38 keV. ²²⁷Ac decays to stable ²⁰⁷Pb through alpha decay. This last contribution has been reduced over two orders of magnitude in the last years [78].

Another drawback of this crystal is that the energy resolution is poorer than that of NaI(Tl) at low energies (below 100 keV). To explain this aspect, we can take into account three contributions to the energy resolution (R defined as the full width at half maximum over the energy centroid $\Delta E/E$):

$$R^2 = \frac{2.35^2}{N_{ndp}} + R_{det}^2 + R_{intr}^2. \quad (4.8)$$

The first term comes from the Poisson statistics in the number of detected photons (N_{ndp}). The second term considers various contribution such as the crystal quality, the quantum efficiency of the light detector entrance window and electronic noise. The third term is due to an intrinsic non-proportional light conversion, crystal dependent [77]. LaBr₃(Ce) shows a strong non-proportionality in the 20-100 keV region (Fig. 4.27).

At 662 keV the R_{intr} contribution is on the order of 2% [79] and still dominates the energy resolution. In fact, the pure statistical resolution, defined by the first term in equation 4.8 or:

$$R = \frac{2.35}{\sqrt{N_{ndp}}} \quad (4.9)$$

at 662 keV ($N_{ndp} = 662 \times 63 = 41706$) is $R = 1.15\%$. Summing both the contribution still results in $R = 2.3\%$ that is less than the 2.8% achieved in literature. The

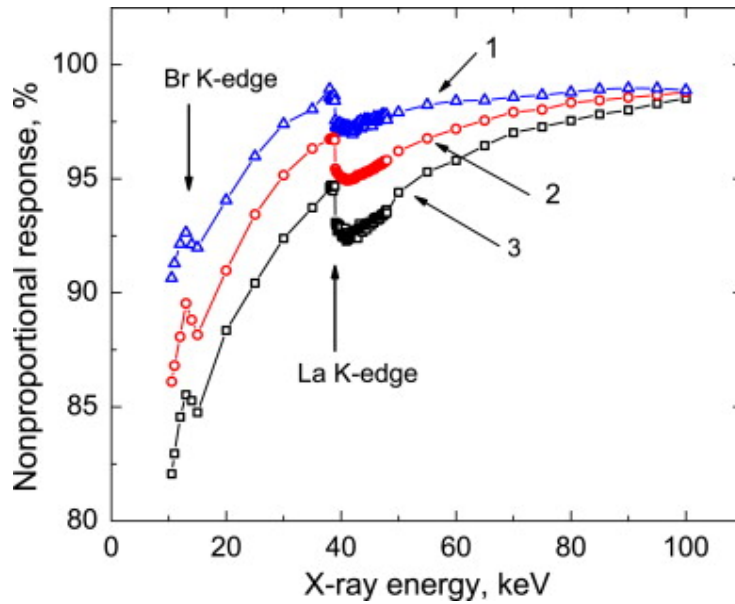


Fig. 4.27 Photon nonproportional response of LaBr₃(Ce) as a function of X-ray energy (EX) curve at (1) 80 K, (2) 295 K, and (3) 450 K [23].

reason of this discrepancy is in the R_{det} term of the equation 4.8, or the detector contribution.

For the 2014 data taking we built a 2x2, 1.27 cm x 2.5 cm (base circle diameter x height) cylinder crystal shape, matrix (Fig. 4.28). This approach was abandoned in favour of 8, 2.5 cm x 2.5 cm (base circle diameter x height) crystals arranged in a star shape all around the gas target. This new solution permits to cover a larger solid angle all around the target putting the detectors as close as possible to it. Using the same geometry but with 1.27 cm crystals would have resulted in 32 detectors thus quadruple the number of channels.

The PMT and electronics

In order to capture all the light emitted by the LaBr₃ scintillator, photomultiplier from HAMAMATSU was chosen. In particular the R11265U-200 metal channel dynode (MCD), ultra bialkali (UBA) cathode model. It has an active area of 23 x 23 mm that match with the crystal dimensions.

In PMT, photoelectrons generated by the light interaction with the cathode, are focused and accelerated by the electric field of the first dynode. By hitting this first dynode they produce secondary emission electrons. Due to the inter-dynode



Fig. 4.28 LaBr₃ old design matrix [17].

potential, the process occurs multiple times (equal to the number of dynodes) producing an electron avalanche down to the anode, resulting in an electronic multiplication (M):

$$M = \prod_{i=1}^N g_i, \quad (4.10)$$

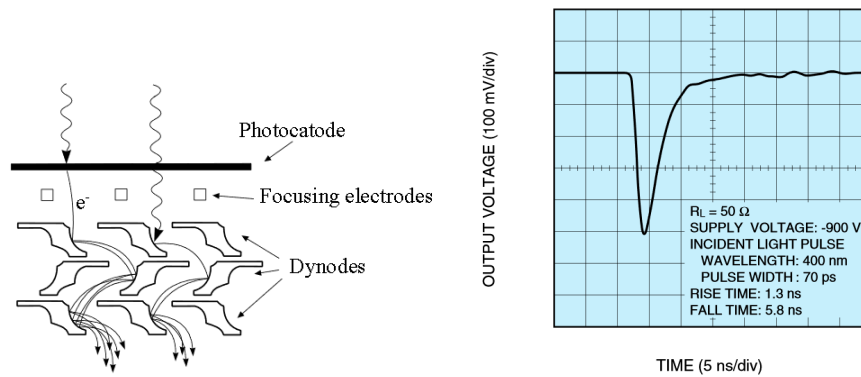
Where n is the number of dynodes and g the gain of each of them. It depends on the applied electric field.

The secondary electrons emission is governed by a Poisson distribution [80] and slightly affects the total energy resolution achievable by the entire system.

The MCD structure guarantees excellent timing characteristics and gain stability, thanks to the extreme compactness of the dynodes distribution (Fig. 4.29). In fact, the time response is fast. The rise and fall time are respectively 1.3 ns and 5.8 ns with a pulse width of 70 ps [81] that are far below the crystal timings.

Another factor that affects the energy resolution is the cathode quantum efficiency (QE). It represents the fraction of photons interacting with the cathode, that is actually converted in photoelectrons.

In recent years the main manufacturers spent a lot of effort to improve the QE of the PMT photo-cathode. The first step was to deposit a few alkali materials on an antimony film to lower the semiconductor work function, thus producing



(a) Metal channel dynode structure and visualization of the multiplication process [80]. (b) Timing characteristics of the R11265U-200 HAMAMATSU PMT[81].

Fig. 4.29

alkali-antimonide photocathode [24]. Potassium and caesium are the most used alkali materials resulting in the so-called bialkali cathode. Even with this enhancement, the QE is still lower than 30% (to be compared with silicon photodetectors reaching up to 90% of QE). Improving the antimony crystalline film characteristics, HAMAMATSU increased the QE of a bialkali cathode approximately of a factor two in the so-called "ultra bialkali" (UBA) photocathode. As shown in Fig. 4.30 a peak of 43% for the QE at 380 nm was obtained. As a reminder, 380 nm is in the emission peak region of LaBr₃ scintillator.

The QE directly affects the energy resolution because the amount of photons detected is only the 43% of the emitted by the scintillator. We can add the QE into the equation 4.8 resulting in an upper limit of $R = 2.66\%$ to the LaBr₃, UBA PMT coupled system resolution (if no sources of noise are present).

In order to generate the inter-dynodes potentials, a resistive voltage divider is commonly used. To preserve the multiplication linearity, the current flowing through the dynodes (the charge signal) must be much less than the one flowing into the voltage divider. If not, the potential at each dynode is affected by the signal, resulting in a lack of linearity. Usually a ratio of 1:100 between the two currents is sufficient to guarantee a linear response of the PMT-voltage divider system (Fig. 4.31).

Depending on the application, two different voltage dividers styles are commonly

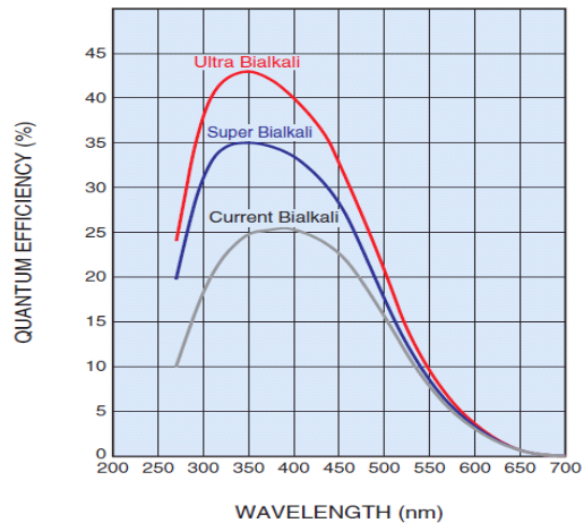


Fig. 4.30 PMT cathode quantum efficiency for bialkali, super bialkali and ultra bialkali photocathode [24].

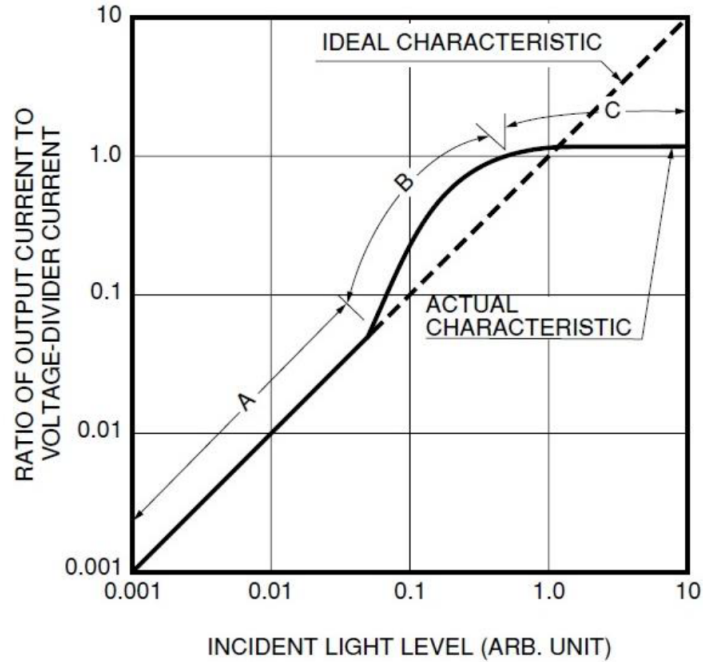


Fig. 4.31 Ratio of output voltage to voltage divider current over incident light level. Three region are present: A linear, B non linear, C saturation [25].

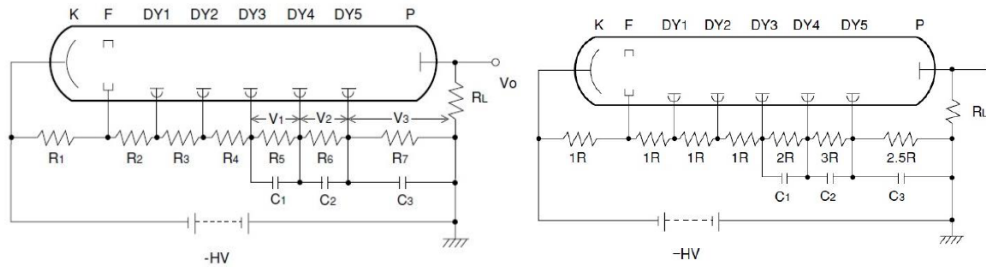


Fig. 4.32 Left: linear voltage divider. Right: tapered voltage divider, the voltage drop across the last dynodes is increased by increasing the resistance value [25]

used: linear and tapered. They differ in the inter-anode voltage ratio: in the linear case, the potential drop at each dynode stage is constant while for the tapered, the last stages have bigger drops (Fig. 4.32). The first style is used when the signal pulses (proportional to the number of photons interacting with the cathode) are not so big and/or in case of low rate application. When the impulse current increases, it is convenient to increase the inter dynode potential in the last stages in order to reduce the spatial charge accumulation that acts as a saturation, reducing the system linearity. With the tapered style, the signal current range is increased (Fig. 4.33) but the gain results reduced (usually by a factor 10).

Adding capacitors to the last dynodes resistances (in parallel) helps to deal with impulsive high rates. They deliver, for a short time period, the necessary current reducing the effect on the voltage divider potentials.

When the signal amplitude is big and the expected rate high, even the tapered voltage divider (with capacitors) loses linearity. To deal with this kind of problem, active elements, such as transistors, are added to the divider. They are placed in parallel to the resistances and act as current sources. In this way, the current flows through the transistors instead that through the resistances, reducing the voltage drop on them thus, preserving the system linearity.

During the first measurements in 2014, where the linear voltage divider coupled with a single high voltage (HV) source for 4 detectors was used, we faced linearity losses and crosstalk. These were due to two main problems:

- the high light scintillator output combined with short time decay results in a high current density produced by each detected X-ray. The single HV

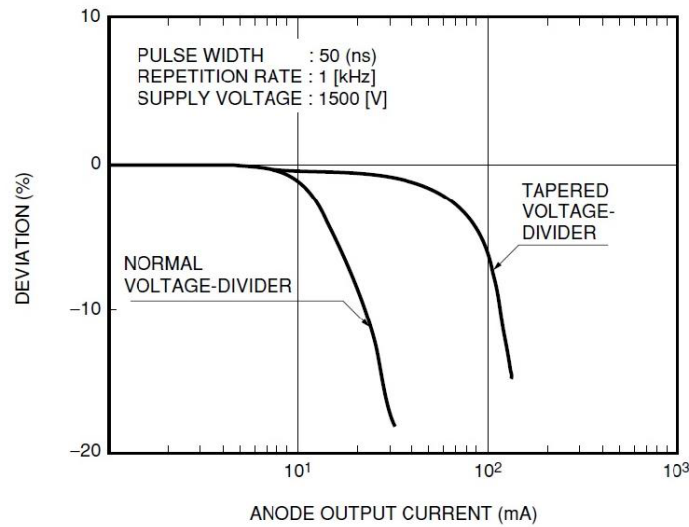


Fig. 4.33 Deviation from linearity versus the anode output current (proportional to the incident light) for a linear and a tapered voltage divider. The linear region is increased by the second divider style [25].

power supply with a maximum current of 4 ma cannot deal with such density resulting in an oscillation that affects all the four channels.

- A high multiplicity of X-rays produced during the prompt phase.

Moreover increasing the scintillator crystals volume leads to an increase of multiplicity in the detected X-rays, due to the solid angle increasing. For these reasons, in the 2016 detector design, we developed a custom, fully active voltage divider (Fig. 4.34). On the transistor gates divider (i.e. through the resistances) flows a small current (30 μ A); the line of the sources-drains is supplied with a current limited to 2 mA. The choice of the inter-dynode capacitance is fundamental for high rate applications: the size of the capacitors can provide up to 25 mA for a short time [82]. This upgrade, totally solved the previous design problems and this solution was used for the 2016 and 2017 data taking.

In the last year, we focused on the simplification of the aforementioned scheme reducing the number of transistors thus, the total power consumption and generated heat. In the new scheme, only the last four dynodes, where the signal current is far bigger than in the previous ones, have a transistor current source.

By splitting the HV power supply is possible to feed with a low current, low ripple, high voltage source the resistive divider and, with a high current (up to 4 mA)

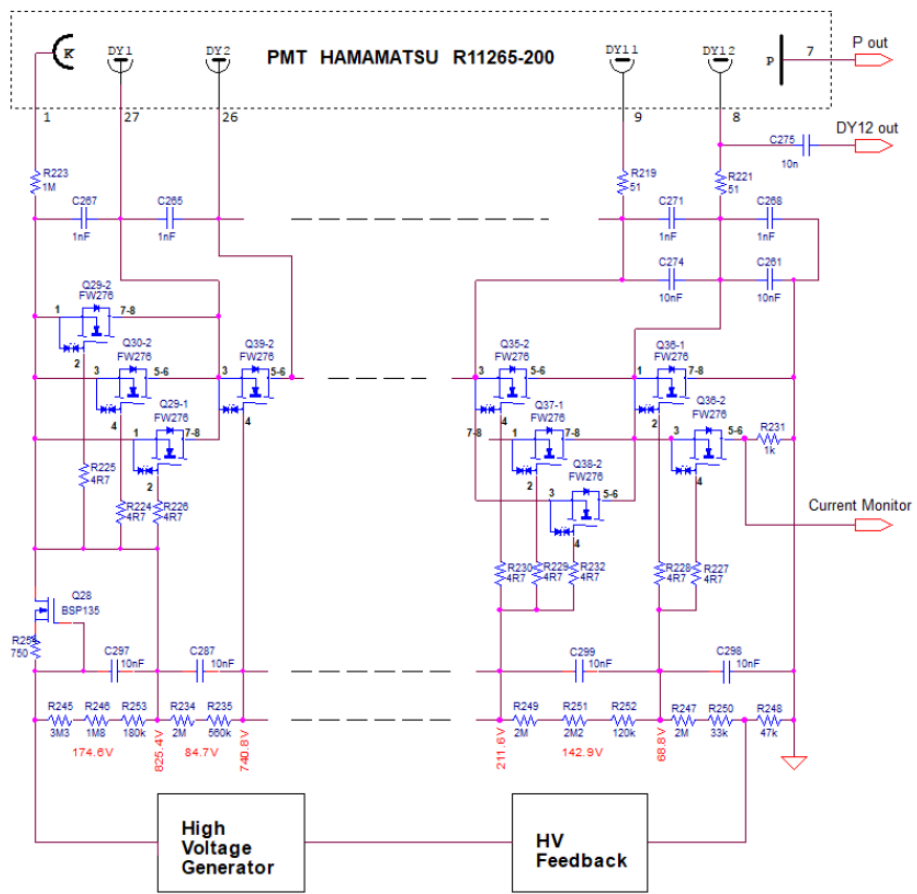


Fig. 4.34 Active voltage divider used in the 2016 detector version [18].

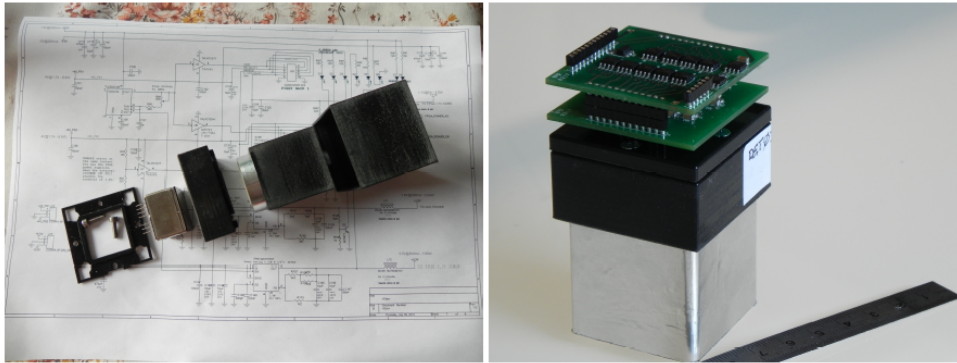


Fig. 4.35 Left panel: disassembled detector: the circular LaBr₃:Ce crystal and the squared PMT are visible. Right panel: assembled detector with part of the electronic visible, in particular the active voltage divider MOSFETs. [18].

medium voltage (300 V) source the transistors on the last 4 dynodes. The total power consumption decreases from 2 W to 1.2 W with an increase in the deliverable current of an order 2. This approach doesn't affect the signal shape and timing thus, the energy and time resolution are preserved. The two currents were set at 300 μ A and 3 mA respectively for the resistive part and for the transistors.

The anodic signal is filtered by a first order low pass active filter. The cutoff frequency is 125 MHz. This is necessary in order to decrease the amount of high-frequency noise and to reduce the data acquisition noise impact. In fact, as long as the sampling rate (500 Msps for our DAQ, see section 4.8) is at least 4 times higher than the input band, the noise is determined by the power spectral density of the input signal only [83]. This unitary amplification stage, act as cable buffer too.

The final detector and performances

We assembled 8 LaBr₃(Ce:5%) 2.5 x 2.5 cm (diameter x thickness) cylindrical shape, crystals coupled with HAMAMATSU R11265U-200 PMT and the active voltage divider in a custom plastic, 3d printed case. The PMT-crystal coupling is made using optical grease (Saint Gobain BC-630) and the ensemble is held together by the black plastic case that acta as an optical light sealer too (Fig. 4.35). The PMT+crystal ensemble is then fitted inside a 3 x 3 cm square, 2 mm thick aluminium profile. At the top side of the profile, a cable panel hosts all the connections: two low voltage power supplies (+5 V, -5 V) for the filter/amplification part, the high voltage

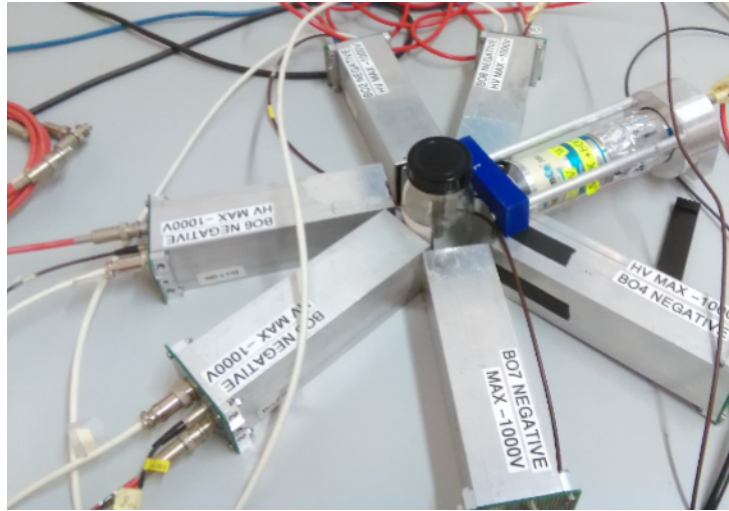


Fig. 4.36 Five assembled FAMU LaBr₃ custom detectors and a commercial one during the test phase before the integration. The three cable connections are visible at the bottom end of the aluminium profile.

(down to -1000 V) through a HV BNC connector. A Lemo cable is suited for the detector output (Fig. 4.36). The eight detectors were assembled and put in position around the gas target as shown in the 3D CAD in Fig. 4.37 (LaBr), in particular, two half star with 3 cm offset in between (along with the target longitudinal direction) were fitted according to the simulation in Fig. 4.38. The HV power supply, that regulates the PMT overall gain, of each detector was set in order to fully exploit the DAQ dynamic range of 0–0.5 V. In particular, the pulse height corresponding to the well known 662 keV ¹³⁷Cs γ -ray line, was set at 0.40 V thus, a total dynamic range in energy of 0– \approx 800 keV.

Due to the low pass filter, the output signal shows a rise time of 12 ns while the decay time is 25 ± 2 ns. In Fig. 4.39 the peak shape at the anode level and after the filter is shown. Calibrations showed good linearity across the energy range.

All the resolutions were calculated by digital filtering the signals with a shaping time of 100 ns (for further details on the filter, see section 4.9). Each detector has a slightly different energy resolution (R) and the average is $9.2\% \pm 0.6$ at 122 keV and $3.6\% \pm 0.3$ at 662 keV. The variability in the low energy peak, reflect the average crystal non-linearity in this energy region. R behaviour was found proportional to

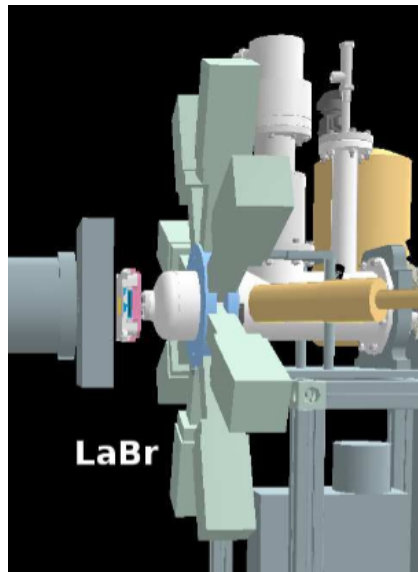


Fig. 4.37 3D CAD of the LaBr₃ star shaped detectors array fitted around the gas target [18].

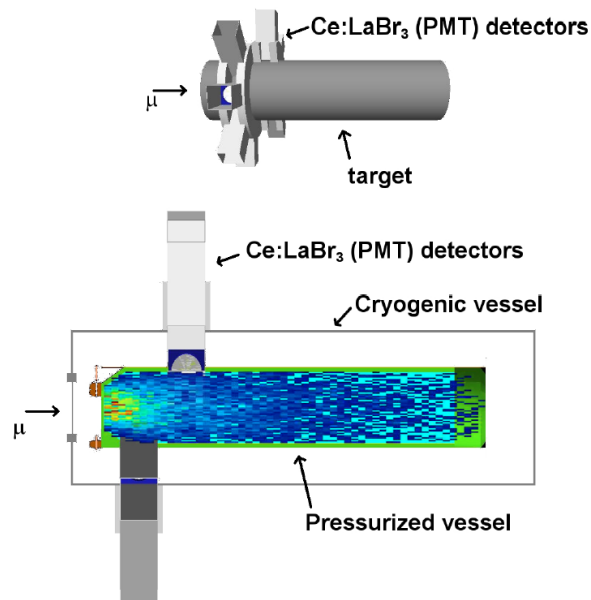


Fig. 4.38 Top: particular of the shifted half stars shape detector array around the gas target. Bottom: detectors positioning and muons stop simulation [18].

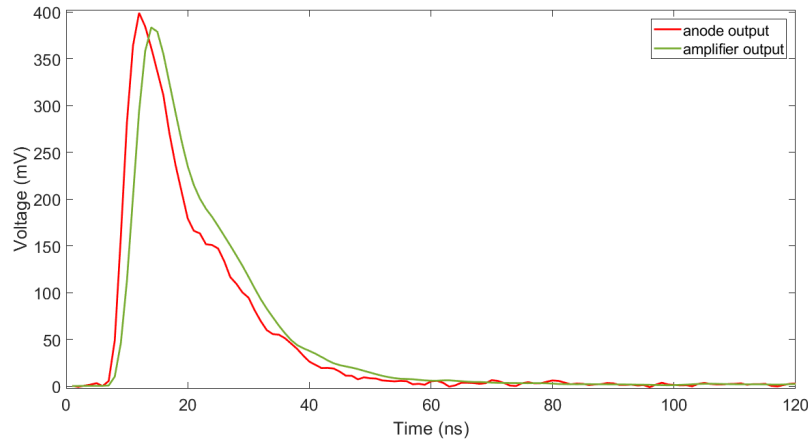


Fig. 4.39 ^{137}Cs peak as acquired at the anode level and after the 125 MHz active filter.

the inverse quadratic of the energy:

$$R = \frac{99}{\sqrt{E}}. \quad (4.11)$$

The best energy resolution was achieved on the detector called "LaBrBO3": 8.8% @ 122 keV and 3.5% @ 662 keV.

These resolutions are worse than the best results achieved in the literature (i.e. 2.6% @ 662 keV in [84]) because we focused on the high rate stability performances more than on the pure resolution.

To test the detector linearity and the overall performances in high rate situations, we took advantage of a 3 MBq uncollimated ^{137}Cs source. We measured the peak height and the energy resolution, varying the source–detector distance from 1 cm to 5 cm ($\approx 1 \text{ MHz} - 0.05 \text{ MHz}$ effective detector counts). During the procedure, the currents flowing in the two branches of the voltage divider (transistor and resistance) were monitored too. We didn't observe any interesting variation in the resistive current (that regulates the PMT gain thus, the peak height) and less than 3% in the transistor flowing one. Anyway, the peak height was not affected as the energy resolution.

During the measurements at RAL, the detectors behave almost like in the lab. We can compare the measured resolution for the muonic oxygen $\text{K}\alpha$ at 133 keV and the expected value from the equation 4.11, as overall performances figure of merit. We

found only small differences of about 2% with an average of 8.8% for the measured peak, while the expected is $\approx 8.6\%$.

4.7 X-rays detection system: High Purity Germanium

A companion high-resolution High purity Germanium detectors (HpGe) array is used in order to have an independent high-resolution X-ray monitoring.

HpGe is a solid state radiation detector. It is essentially a diode (p-n junction) in which the intrinsic (or depleted) region is sensitive to passing ionizing particles. A reverse biasing voltage (V) is applied to the junction in order to increase the physical dimension of the depleted region (d):

$$d = \sqrt{\frac{2\varepsilon V}{eN}}, \quad (4.12)$$

where e is the electric charge, ε the dielectric constant and N is the impurity deposited in the bulk germanium. At a fixed bias voltage (below the breakdown level), the dopant concentration defines thus the depletion depth. As the name suggests, HpGe detectors have very low impurity concentration, usually less than 10^{10} atoms/cm³, to be compared with the common silicon detectors impurity concentration of 10^{13-18} atoms/cm³. In order to detect high energy photons (hundreds of keV, a typical efficiency curve is shown in Fig. 4.40) the active depth must be at least of some millimetres. For example, applying a reverse voltage of 1000 V corresponds to a depleted region of 10 mm. Using coaxial structure (instead of the classic planar one) it is possible to increase the depleted area increasing the detector efficiency up to several MeV.

Germanium semiconductor has a small energy gap of only 0.7 eV, this is the energy needed to produce an electron-hole couple. The energy resolution is related to the poissonian statistical electron-hole couples production mechanism thus, this small gap permits the extreme energy resolution (up to 0.2% @ 662 keV). Because of such low band gap, these detectors must be cooled in order to reduce the thermal generation of charge carriers (thus, the reverse leakage current) to an acceptable level. Otherwise, leakage current induced noise destroys the energy resolution of the detector. Liquid nitrogen, which has a temperature of 77 K is the common cooling medium for such detectors.

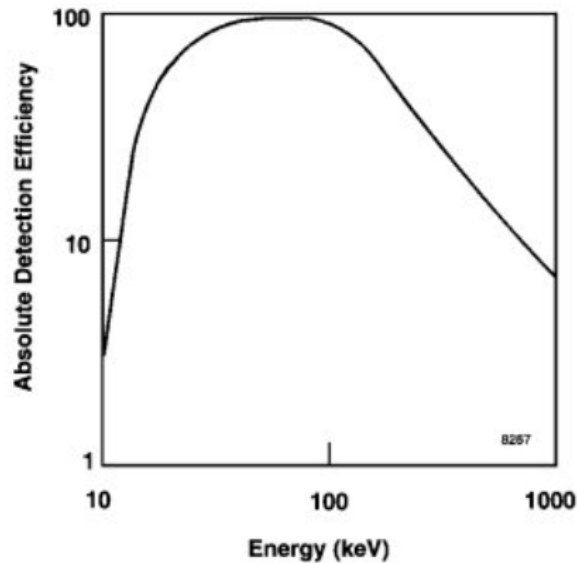


Fig. 4.40 ORTEC coaxial HpGe detector efficiency curve as function of the X-ray photon energy.

The charge pulse coming from the semiconductor ionization is integrated by a charge sensitive pre-amplifier. For each detected X-ray, the output is then a step pulse whose height is proportional to the X-ray deposited energy. Because of the charge integration, for each detected X-ray the output signal increases up to the limit of the pre-amplifier dynamic. To avoid that, a reset circuit is needed. There are two different kinds of pre-amplifiers which differ in the reset circuit implementation. In the continuous reset, a low frequency filtered part of the pre-amplifier output is sent, reversed, to the input. In this way, the high-frequency step is preserved while the subsequent flat part, due to the feedback subtraction, exponentially decays (with a decay constant of tenths of μs) to the baseline (Fig. 4.41).

There is another way to reset the signal, by using a transistor (instead of an RC network) in the feedback circuit. When the signal passes a certain threshold, a fixed voltage applied to the transistor base, put it in saturation. All the signal is then fed, reversed to the input, pushing quickly (some μs) the output signal down to the baseline (Fig. 4.42). When the reset is ongoing the system can't detect any signal.

The pre-amplifier output signal has a sharp rise time that depends on the detector dimension and usually is in the 100–400 ns interval. In most cases, the pre-amplifier feed a Gaussian shaping amplifier that filters the signal in order to increase the

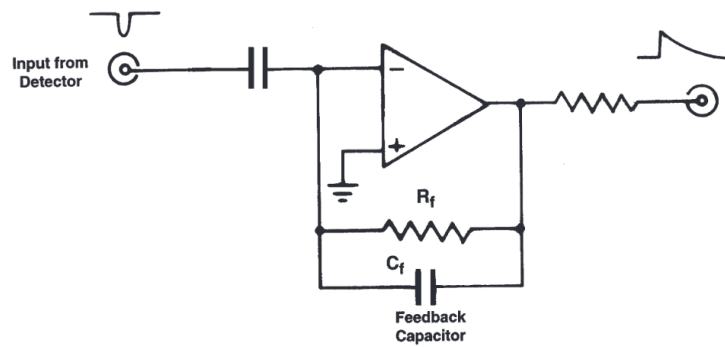


Fig. 4.41 Scheme of a continuous reset pre-amplifier with a $R_f C_f$ feedback network.

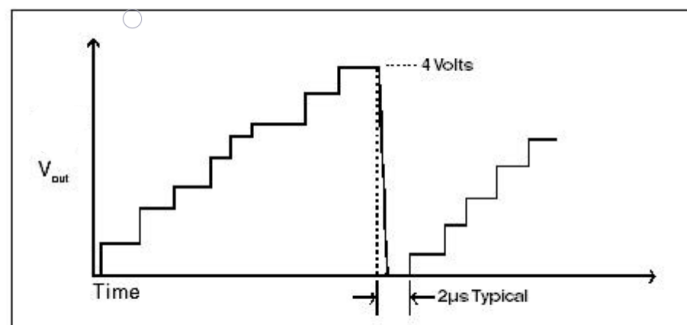


Fig. 4.42 Typical output of a transistor reset pre-amplifier (TRP). When the signal reaches 4 V, the transistor injects the output in the amplifier resulting in a fast return to the baseline.

signal to noise ratio (see paragraph "planned upgraded on-line data analysis" in section 4.9 for further details). The Gaussian output signal usually has a rise time of a few μs . A common limitation for the shaped signal in a high multiplicity environment is the pile-up effect. To avoid spurious peaks in the energy spectrum, a pile-up rejection algorithm eliminates these events from the final spectrum. It results in a decreased apparent, X-rays detected statistic. This is defined by the dead time concept. Dead time stands for the time interval in which the detector chain output is not reliable (due to pile-up, saturation, shaping amplifier integration etc...) so, not taken into account in the analysis.

For a shaped signal, the dead time, if no pile-up rejection algorithm is used, corresponds to the total Gaussian-shaped signal duration (from baseline to baseline). Due to the symmetric nature of the filter, the total duration is two times the peaking time that is 2.4 times the shaping one.

In the FAMU high rate condition, due to the long signal duration, it is likely to face signals pile-up condition. Moreover, these detectors are expensive (the price starts from tenths of kilo Euro) making hard to implement a full solid angle coverage HpGe array. That's why we decided to place them not so close to the target. In this way, they act as a high resolution, low statistics monitors. Nevertheless, by acquiring the pre-amplified signals and, thanks to a fast shaping amplifier we successfully extract timing information too.

In FAMU apparatus, four HPGe detectors are placed beyond the LaBr₃(Ce) crown: one ORTEC GLP (planar configuration), two ORTEC GEM-S (semi-planar configuration) and the last one is an ORTEC GMX Gamma-X (coaxial configuration). This last one and one of the GEM-S were made available by the RIKEN-RAL staff. The GLP excels in the soft X-rays energy region; the GEM-S model is suited for middle energies (10 keV–1 MeV) while the GMX use, is appropriate for high energy X-rays (up to 10 MeV).

All the detectors are followed by an ORTEC 672 spectroscopic amplifier. One of the GEM-S detectors feeds an Ortec 579 fast amplifier too.

The shaping time is respectively 2 μs for the ORTEC 672 and 200 ns for the 579 model for a total shaped signal duration of $\approx 9.6 \mu\text{s}$ and ≈ 960 ns respectively.

The on beam resolution we reached in the low energy region (up to ≈ 200 keV) with the GEM-S HPGe detector connected to both the shaping amplifiers and with the only pre-amplifier are shown in Table 4.1 and are referred to the two

transition	E(keV)	pre-amp		Ortec 672		Ortec 579	
		E(keV)	FWHM(keV)	E(keV)	FWHM(keV)	E(keV)	FWHM(keV)
Ni $4f \rightarrow 3d$	107	107	5.1 ± 0.4	107	2.4 ± 0.2	107.3	5.5 ± 0.1
O $2p \rightarrow 1s$	133.5	133.9	5.4 ± 0.5	133.4	2.7 ± 0.5	134.4	7.4 ± 0.5
O $3p \rightarrow 1s$	158.4	157.6	5.2 ± 0.4	157.5	3.5 ± 0.5	160	4.3 ± 0.3

Table 4.1 Characteristic muonic X-ray lines detected by the GEM-S HpGe during the 2016 data taking.

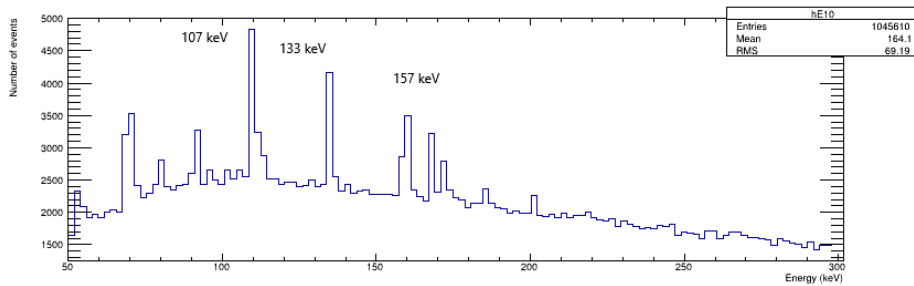


Fig. 4.43 On beam spectrum with GEM-S HpGe detector shaped with an Ortec 672 with $2\mu\text{s}$ of shaping time.

spectra in Fig. 4.43 and Fig. 4.41. It is possible to notice that as the shaping time increases the detector performance (energy resolution) increases too. Still, they are quite far from the best one achieved with low rate radioactive sources. In fact, the nominal resolution at 122 keV peak is on the order of 1% for $2\mu\text{s}$ Gaussian-shaped signal and 2.5% when coupled with the fast Ortec 579. This demonstrates that the detectors are not working in their foreseen conditions due to, not only the high rate but to the electronic noise in the signal (Fig. 4.45) too.

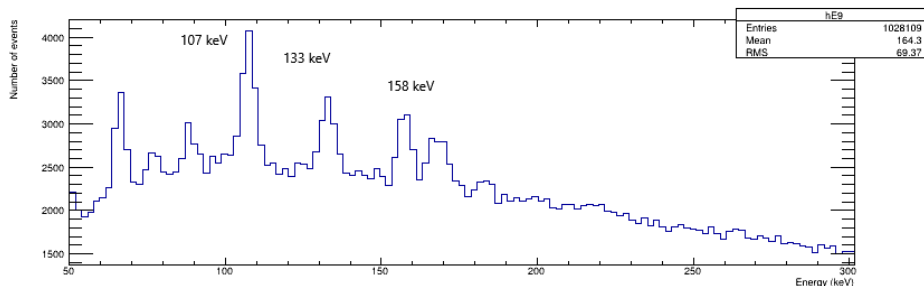


Fig. 4.44 On beam spectrum with GEM-S HpGe detector without any shaping. The pre-amplifier signal was used.

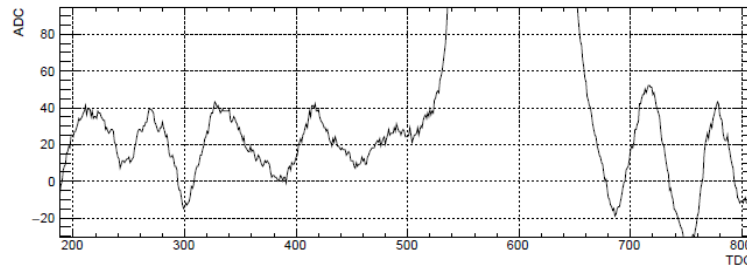


Fig. 4.45 Noise in the GEM-S fast amplified baseline signal [26].

4.8 Data acquisition and data handling

In order to handle the detectors signals and the temperature sensors, a custom data acquisition system was developed. The idea is to record the entire waveform of each detector/sensor, without any kind of data reduction or hardware processing, allowing an accurate and deeper off-line data analysis.

The system is based on different data acquisition VME modules built by CAEN s.p.a. with different settings, depending on the acquired detector. The acquired waveforms are then transmitted from the VME data bus, through a CAEN proprietary optical link (CONET), to an acquisition PC where they are stored as HBOOK format files. This process is made possible thanks to a CAEN V2718 VME PCI Optical Link Bridge (VME side) connected to a CAEN A2818 PCI controller card (computer side). The maximum data rate achievable is 80 MByte/s [36].

The eight fast $\text{LaBr}_3(\text{Ce})$ based detectors are acquired by a CAEN V1730 module. It is an 8 channels 14 bit 500 MSps digitiser board with a software selectable input dynamic range of 0.5 or 2 Vpp. The 4 HPGe detectors are acquired by a CAEN V1724 module that can acquire 4 channels at 100 MSps with 14 bit of resolution. The dynamic range is hardware fixed at 10 Vpp. The hodoscope, with its 64 channels, needs two CAEN V1742 32 channels each, 12 bit at 1 GSps modules.

All the data acquisition modules share the same trigger signal coming from the Cherenkov muons detector (described in section 4.1) but the time windows are different for each application.

For fast LaBr_3 detectors it is set at $10 \mu\text{s}$ while for the slower germanium detectors is $20 \mu\text{s}$ (in order to acquire the total shaped signal). The hodoscope fibres response is needed only during the beam pulses so a smaller time window of $1 \mu\text{s}$ is therefore sufficient. Moreover, thanks to the circular buffer architecture of each module,

Detector	LaBr ₃ (Ce)	HpGe	Hodoscope
CAEN model name	V1730	V1724	V1742 × 2
Channels n.	8	8	32+32
Resolution (bit)	14	14	12
Sampling rate (MSps) / time (ns)	500 / 2	100 / 10	1000 / 1
Dynamic range (Vpp)	0.5 - 2	10	1
Time window (μ s)	10	20	1

Table 4.2 Summary of the DAQ modules characteristics [36].

the pre and post-trigger time can be manually set. In Table 4.2, all the modules characteristics are summarized.

The Lakeshore temperature controller communicate the sensors reading through an Ethernet port to the acquisition PC.

The system is capable of continuously acquiring data at the beam frequency (nominally 50 Hz) for a total of ~ 200 GByte/day. Data are saved in HBOOK format file, containing 10000 events or beam triggers.

A series of automated scripts permits to:

- convert the HBOOK format PAW ntuples in ROOTple through the h2root command;
- create a row in the MySQL database (DB) with the measure conditions (such as beam momentum, target pressure and set temperature) and file infos;
- copy the converted files to a repository at the CNAF Tier1, via a Grid-FTP protocol;
- update the DB informations rising the "copied to CNAF" flag;
- start the FAMUAnalysis software to analyse the detectors waveform thanks to the "quicklook" application;
- produce figures such as energy and time spectra of each detector;
- copy all the figures in the Trieste INFN farm and upload on the FAMU dedicated web page for a remote view by the collaboration members;

- finally update the DB rising all the flags indicating the software tasks completion.

FAMUAnalysis is a C++ language written software suit that uses the ROOT toolkit. It contains all the applications needed for the FAMU data analysis. The next section is devoted to explaining the main characteristics of the suite.

Planned improvements to the LaBr₃ detectors DAQ

To fully exploit the LaBr₃ detector performances in terms of signal duration, a custom and faster data acquisition module was studied and designed. The idea is to increase the sampling rate up to 1 Giga sample per second with at least the same conversion resolution (14 bit) of the current DAQ; moreover a field programmable gate array device (FPGA), acting as digitized data receiver can easily perform digital shaping algorithm (fully described in the next section) permitting a real-time on-line quick look analysis with improved performances both in energy resolution and pile up reduction. If the tests we planned will confirm the validity of this new approach, data reduction is possible too.

To keep low the costs for this upgrade option we chose to use two different ADC channels operating at 500 Msps with a time-interleaved approach. This results in a cost reduction because of the simpler communication downstream the converter. As the conversion rate increase at 1 GHz, the common communication protocol is JESD204, a multi-gigabit serial data link. The amount of these multi-gigabit receivers, and their speed, mostly impacts on the final FPGA cost. By using instead, parallel low voltage differential signaling (LVDS) lines, it is possible to use low-end FPGA or, as we did, use a high-end FPGA chip to control and acquire multiple ADCs. By finely tuning the conversion clock phase of each ADC, more channels can be interleaved increasing the total sampling rate at cost of channels number.

The concept design is shown in Fig. 4.46. A set of 4 Analog Devices AD9684³, dual channel, 14bit operating at 500 Msps converters feeds the Xilinx Zynq Ultrascale+ FPGA chip hosted on a so called "system on module" or SOM, model XU-1 produced by Enclustra⁴. The SOM host all what the FPGA needs to work, from the power supply to the memories (4 GB of RAM and 16 GB of eMMC flash) and the

³ADC specifications web site: <https://www.analog.com/en/products/ad9684.html>

⁴Enclustra SOM specifications web site: <https://www.enclustra.com/en/products/system-on-chip-modules/mercury-xu1/>

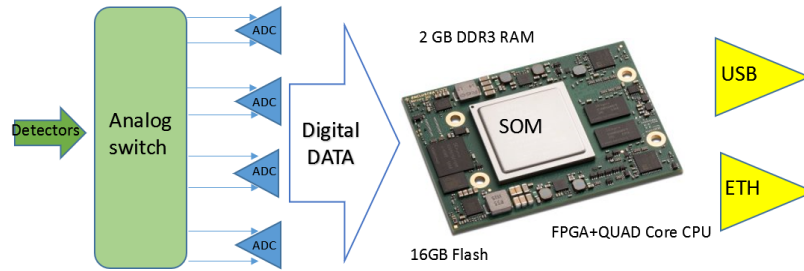


Fig. 4.46 Proposed DAQ upgrade schematic design.

physical layer chips (PHY) that permits the communication with the acquisition computer, in particular through Ethernet network or USB. Inside the FPGA chip, an ARM, quad core CPU coexists in the same package. This permits high level coding for the interfaces management.

In the analog part, a set of analog switches routing the detectors signals, permits to configure the DAQ board behaviour:

- 8 channels at 500 Msps;
- 4 channels at 1 Gsps;
- 2 channels at 2 Gsps;
- 1 channel at 4 Gsps.

We investigated the time interleaving method with a low resolution and not optimized proof of concept board. This board, called "GSPS", designed by the INFN electronic division of Bologna, is based on two Analog Devices AD9434⁵, single channel, 12 bit at 500 Msps ADCs operating in time interleaving mode. The converted data are transmitted via an FMC connector to a Digilent ZedBoard development board⁶ that hosts a Zynq 7020 Xilinx FPGA. Thanks to this demonstrator design we faced all the problems the interleaving system carries on. In fact, gain, offset and clock phase mismatches affect the final DAQ resolution. We can use the effective number of bit (ENOB), that is dependent on the ratio between a signal (S) and noise (N) plus the harmonic distortion (D) as figure of merit of the system

⁵ADC specifications web site: <https://www.analog.com/en/products/ad9434.html>

⁶Digilent ZedBoard web site: <https://www.xilinx.com/products/boards-and-kits/1-elhabt.html>

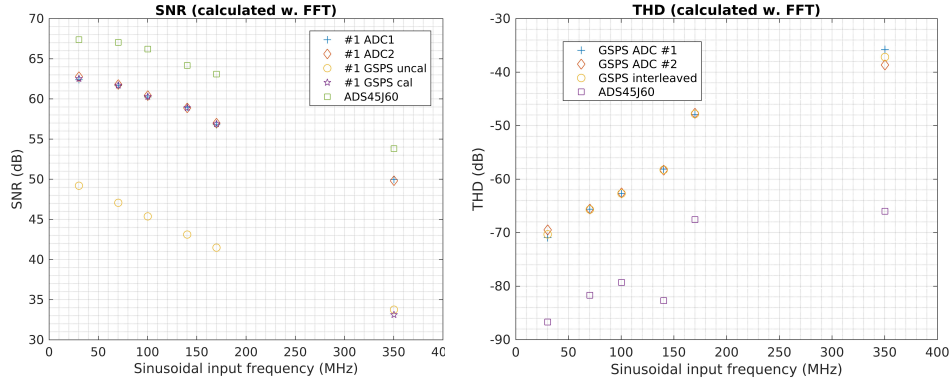


Fig. 4.47 Left panel. SNR of the single ADC and of the interleaved system. ADS45j60 is shown as reference. Right panel. THD of the single ADC and of the interleaved system. ADS45j60 is shown as reference [27].

performances [85]:

$$ENOB(dB) = \frac{20 \log\left(\frac{S}{N+D}\right) - 1.76}{6.02}, \quad (4.13)$$

where the first term of the numerator is called SINAD and can be expressed as a function of the Signal to noise ratio (SNR) and total harmonic distortion (THD):

$$\frac{N}{S+D} = \left[10^{-SNR/10} + 10^{-THD/10}\right]^{1/2}, \quad (4.14)$$

in which:

$$SNR = 20 \log\left(\frac{S}{N}\right) \quad (4.15)$$

$$THD = 20 \log\left(\frac{S}{D}\right) \quad (4.16)$$

These parameters are frequency dependent and by the difference between the single ADC case and the interleaved system, we can determine the concept precision and effectiveness. As shown in (Fig. 4.47) the SNR and THD of the interleaved system match perfectly with the single ADC solution. The resulting ENOB is above 9.5 from DC to 125 MHz. For higher frequencies the harmonic distortion of the differential amplifier that feeds the two ADCs becomes dominant and the ENOB fall below 8 at 200 MHz, reaching 5 at 350 MHz.

So far, we are putting parallel efforts both to test the single ADC–SOM–Ethernet

communication (thanks to two demonstration boards, one for the SOM, the other one for the ADC) and designing the motherboard that will host both the SOM and the analog part with the four, 2 channels ADC chips.

4.9 Data Analysis

In order to extract the physical quantities for the transfer rate measurements, the detectors' data must be treated by proper analysis tools. We developed a fast online data analysis to monitor the acquisition and intervene in case of any problem. The data are then properly processed by an off-line data analysis.

The data took as examples in the next sections are mainly from LaBr₃ detectors and the 2016 data taking.

4.9.1 On-line analysis

"Quicklook"

Right after the conversion the application "quicklook" in the FAMUAnalysis software performs a first fast analysis of the X-rays detectors signal, to give an overview of the time and energy spectra of the detectors.

The following algorithm is used to populate both the time and energy spectra:

- for each detector waveform, the software performs a numerical derivation (Fig. 4.48);
- each zero crossing of this derivative (which correspond to the peak maximum position) indicates a X-ray photon time of arrival;
- the X-ray energy is reconstructed by the difference between the peak height and the baseline mean;
- peaks within a certain duration (depending on the each detector peaking time) are considered piled-up, thus eliminated;
- saturation is recognised and eliminated too.

This algorithm is quite rough but fast, even though the final statistic is affected by the natural pile-up rejection, it permits to monitor the behaviour of the entire

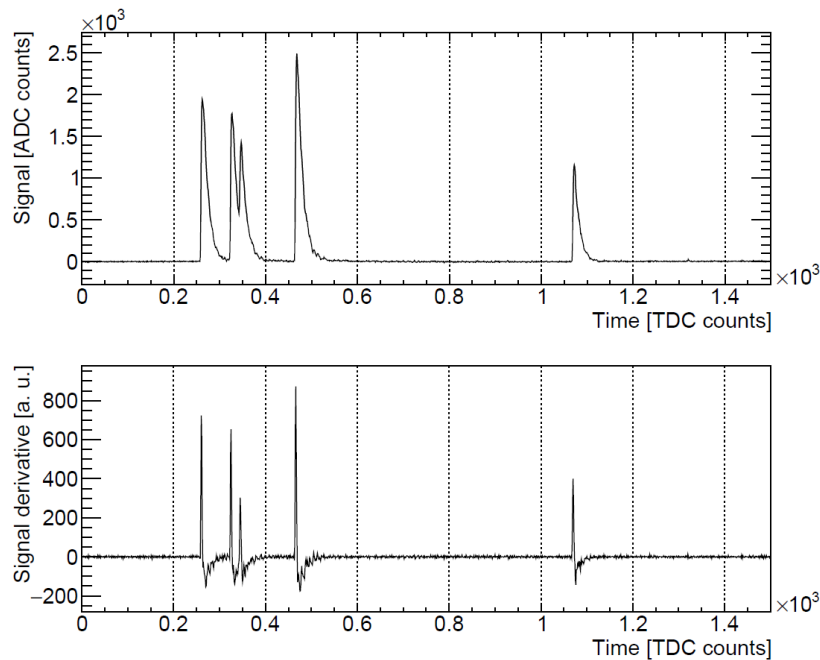


Fig. 4.48 Example of LaBr_3 waveform and the derivation made by the "quicklook" software [18].

system with a very small delay in a quasi-real-time way.

The quicklook software is also in charge of producing the 2D maps of the beam shape using the hodoscope signals.

A custom website hosts the updated "quicklook" spectra and 2D maps (as pictures) for a remote view. As an example, in Fig. 4.49 is shown the X-ray spectrum time evolution of one of the LaBr_3 detectors as it appears on the FAMU quicklook web page⁷.

Planned upgraded on-line data analysis

We studied a new method based on digital shaping to extract both the peak energy and the timing from the detectors waveforms. Digital shaping mimics the classic analog shaping amplifier but operating on the digital domain. Digital shaping has two main advantages in respect of the analog one: preserve all the information the signal carry on (because the raw data are stored for further off-line analysis) and

⁷<https://wwwusers.ts.infn.it/~mocchiut/FAMU/> the access is restricted to the collaboration members

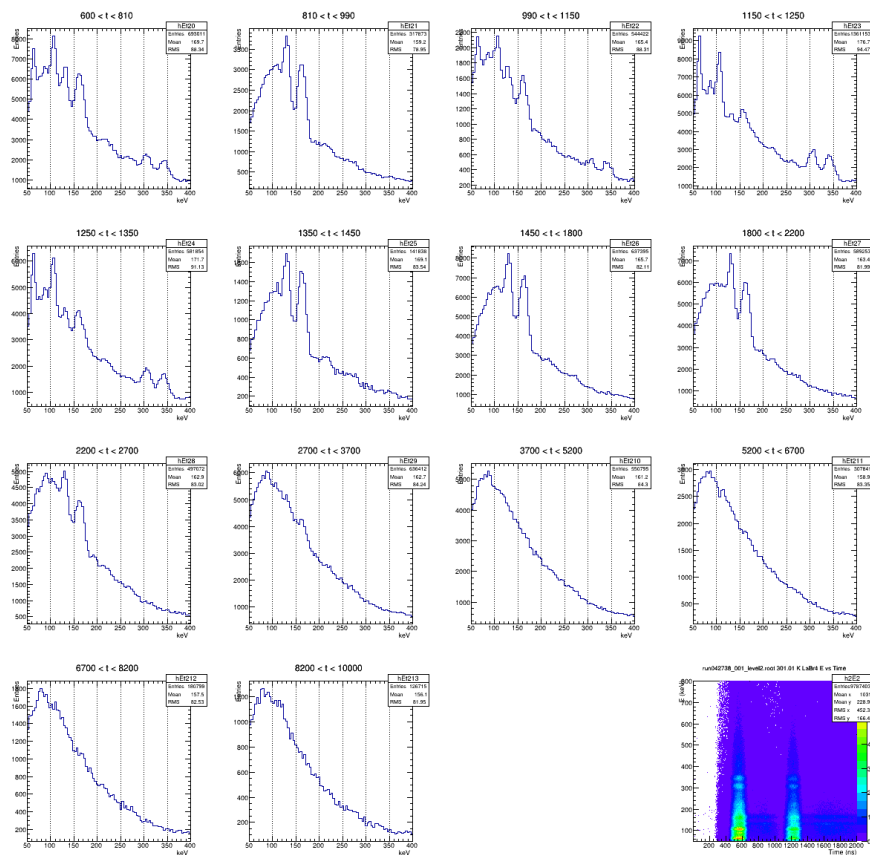


Fig. 4.49 Example of a single LaBr_3 detector waveform time evolution as shown in the FAMU quicklook web page. Each box reproduce the cumulated energy spectrum for different successive time cut. In the bottom left, a false colours 2D map of the time spectra in X (the double pulse muon beam time shape is clearly visible) and energy one in Y.

better performances in terms of pile-up rejection. Digital shaper, like the analog one, acts as a filter in the frequency domain, to reduce the noise thus, increasing the signal to noise ratio. It results in a better energy resolution with respect to the mere peak height.

We can model the detector electric output using three sources:

- the pure detector signal generated by the physical detected event (in our case the X-ray interaction with LaBr_3);
- a parallel noise source;
- a series noise source.

The idea, obviously, is to reduce the contribution of the last two sources without acting on the real signal.

In order to evaluate each contribution, the equivalent noise charge (ENC) value is used. It is defined as the measure of noise in the signal, at the detector level, expressed in charge units. It is mathematically defined as:

$$ENC^2 = C_T a \frac{A_1}{\tau} + kA_2 + bA_3 \tau, \quad (4.17)$$

where C_T is the capacitance seen by the first amplifier stage (the analog to digital converter in our case), τ is the shaping time that defines the output signal duration, a and b are respectively the series and parallel noise contribution while k depends on the so-called "flicker noise" that is proportional to the inverse of the frequency. The three A coefficients depend on the applied shaping filter. Different shaping filters have a different contribution to the noise Fig. 4.50. The indefinite cusp shape has demonstrated to have the best performance in terms of noise suppression [86] so it is used as a normalization factor to evaluate the other filters performance:

$$\frac{ENC_{(suboptimal)}^2}{ENC_{(cusp)}^2} = \sqrt{A_1 A_3}. \quad (4.18)$$

As its name suggests, this shaping has an indefinite impulse response. It implies that in case of multiple detected X-rays, the second, third and so on... pulses response is affected by the filtering process of the first one, this phenomenon is called tail pile-up . To solve this issue, other shapes are commonly used. In the analog domain,

the most common shaping is the Gaussian one while in the digital domain it is the triangular or trapezoidal (triangle is a specific trapezium without flat top). As shown in Fig. 4.50, triangular shaping guarantees the best ENC performance while the trapezoidal is preferred when the detector is affected by ballistic deficit [87]. An ENC decreasing of almost 10% is made possible by using digital triangular filtering instead of the analog Gaussian one. Moreover, this kind of digital filters have a finite response, i.e. its response is of finite duration, because it settles to zero in finite time, in particular for triangular shaping this duration is the rising time of the triangle itself. This significantly improves the performance of digital triangular filtering at high count rates, reducing pile-up and baseline shift. In other words, two consecutive signals can be easily reconstructed (no pile-up occurs) as long as they are separated by τ (shaping time).

The mathematical approach to the trapezoidal (or triangular) shaping is here explained. Given $f_{in}(t)$ an input discrete sampled signal (t sampling time), and convolving it with a proper transfer function $h_{tr}(t)$ we can obtain the triangular/-trapezoidal shaped output $f_{trpz}(t)$:

$$f_{trpz}(t) = f_{in}(t) * h_{tr}(t). \quad (4.19)$$

Applying the Z transform and the convolution theorem, the equation 4.19 becomes a sample dependent (z) function:

$$F_{trpz}(z) = F_{in}(z)H_{tr}(z), \quad (4.20)$$

thus:

$$H_{tr}(z) = \frac{F_{trpz}(z)}{F_{in}(z)}. \quad (4.21)$$

$f_{in}(t)$ is the detector output that can be simplistically defined as a fast rising and an exponential decay (with τ as decay time):

$$\begin{aligned} f_{in}(t) &= 0, & t < 0 \\ f_{in}(t) &= E \cdot e^{-\frac{t}{\tau}}, & t \geq 0, \end{aligned} \quad (4.22)$$

Shaping	$h(t)$ Funcion	A_2	$\sqrt{A_1 A_3}$	$\frac{A_2}{\sqrt{A_1 A_3}}$	A_1	A_3	$\sqrt{\frac{A_1}{A_3}}$		
1	indefinite cusp 	0.64 $(\frac{2}{\pi})$	1	0.64	1	1	1		
2	truncated cusp 	$k = \tau/\tau_c$	$k=1$	0.77	1.04	0.74	2.16	0.51	2.06
		$k=2$	0.70	1.01	0.69	1.31	0.78	1.30	
		$k=3$	0.67	1	0.67	1.10	0.91	1.10	
3	triangular 	0.88 $(\frac{4}{\pi} \ln 2)$	1.15 $(\frac{2}{\sqrt{3}})$	0.76	2	0.67 $(\frac{2}{3})$	1.73		
4	trapezoidal 	1.38	1.83	0.76	2	1.67	1.09		
5	piecewise parabolic 	1.15	1.43	0.80	2.67	0.77	1.86		
6	sinusoidal lobe 	1.22	1.57	0.78	2.47	1	1.57		
7	RC-CR 	1.18	1.85	0.64	1.85	1.85	1		
8	semigaussian (n = 4) 	1.04	1.35	0.77	0.51	3.58	0.38		
9	gaussian 	1	1.26	0.79	0.89	1.77	0.71		
10	clipped approximate integrator 	0.85	1.34	0.63	2.54	0.71	1.89		
11	bipolar triangular 	2	2.31	0.87	4	1.33	1.73		

Fig. 4.50 Shaping parameters useful in the ENC calculation (equation 4.17) [28].

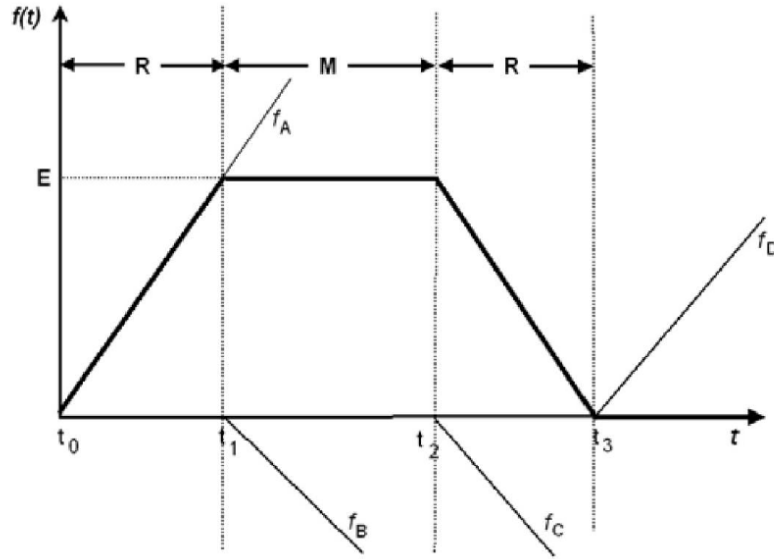


Fig. 4.51 Desired trapezoidal shaping output. It is a composition of four linear pulses $f_{A,B,C,D}(t)$. The time length of these pulses defines the shaping parameters R rise time and M flat top duration [29].

in which E is the signal amplitude. The Z transform of this function ($F_{in}(z)$) is:

$$F_{in}(z) = E \frac{z}{z - \beta} = E \frac{1}{1 - \beta^{-z}}, \quad (4.23)$$

where $\beta = e^{-t/\tau}$.

In Fig. 4.51 the desired trapezoidal output is shown and we can represent it as a sum of four linear pulses $f_{A,B,C,D}(t)$. The $t_{1,2,3}$ timing of the final shape can be expressed as function of the sampling time t , thus:

$$t_1 = Rt, \quad t_2 = (R + M)t, \quad t_3 = (R + M + R)t, \quad (4.24)$$

where Rt and Mt (shown in Fig. 4.51) are respectively the rising and flat top time. The first pulse may be expressed in the Z transform domain as:

$$f_A(t) = \frac{E}{t_1}t \rightarrow F_A(z) = \frac{E}{R} \frac{z}{(z-1)^2}. \quad (4.25)$$

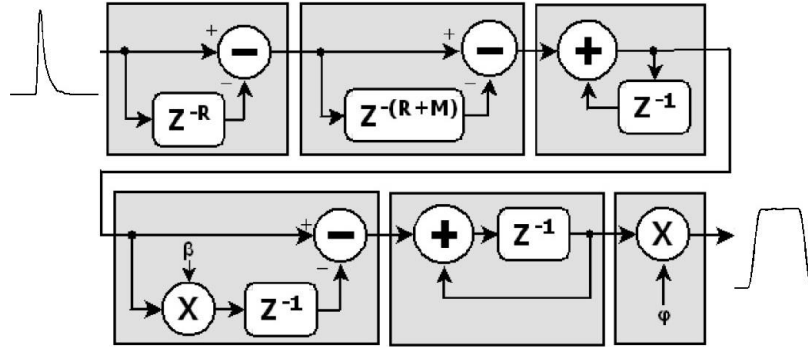


Fig. 4.52 Schematic view of the shaping algorithm blocks [29].

Due to the symmetrical shape, we can express the Z transform of the other linear pulses $f_{B,C,D}(t)$ as function of $F_A(z)$:

$$F_B(z) = -F_A z^{-R} \quad (4.26)$$

$$F_C(z) = -F_A z^{-(R+M)} \quad (4.27)$$

$$F_D(z) = F_A z^{-(R+M+R)}, \quad (4.28)$$

whose sum, in the Z transform domain is:

$$F_{tpz}(z) = \frac{E}{R} (1 - z^{-R} - z^{-(R+M)} + z^{-(R+M+R)}) \frac{z}{(1-z)^2}. \quad (4.29)$$

Using this last relation with the one in equation 4.23 in the ratio in equation 4.20 we can obtain the trapezoidal shaping transfer function:

$$H_{tr}(z) = (1 - z^{-R})(1 - z^{-(R+M)}) \frac{(1 - \beta z^{-1})}{1 - z^{-1}} \frac{z^{-1}}{1 - z^{-1}} \phi, \quad (4.30)$$

where ϕ is a normalization factor corresponding to $\frac{1}{R}$.

The numerator elements between parentheses in equation 4.30 represent three different finite impulse response (FIR) filters while the two denominator elements are accumulation that can be implemented as infinite impulse response (IIR) filters. The schematic representation of these filters is in Fig. 4.52. The z^{-X} terms are translated, in the time domain, as a delay of X time steps of the input signal. We tested two implementations in the MATLAB environment: using a recursive approach in SIMULINK, or thanks to the "filter" function that filters the input

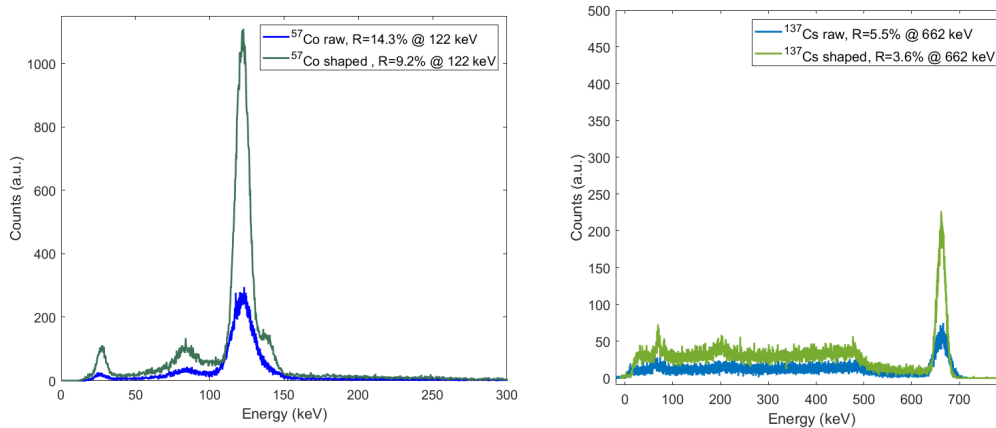


Fig. 4.53 (Left panel. ^{57}Co 122 keV peak resolution using the peak height (raw) and by using a 100 ns digital triangular filter. Right panel. ^{137}Cs 662 keV peak resolution using the peak height (raw) and by using a 100 ns digital triangular filter.

data using a rational transfer function defined by the numerator and denominator coefficients (such as equation 4.30).

Both methods give the same results but using the proprietary filter function results in a faster approach. Fig. 4.53 shows an example of how by using a 100 ns triangular shaping filter the resolution at the 122 keV and 662 keV improves of factor 1.5. In order to incorporate this filtering process in the "quicklook" software, we had to develop a C++ version that is going to be implemented and used in the next experimental runs. The delay function was implemented as follow:

```
void delay(double x[], double y[], int M)
{
  // Delay NBF-elements long x array by M elements
  // (i.e. left shift), zeroing initial elements
  for (int i = 0; i <= M; i++)
    {y[i] = 0.;
     x[i] = 0;}
  for (int i = M ; i<NBF; i++)
    {y[i] = x[i - M];}
}
```

Then the FIR or delay subtracter:

```
void differentiator(double x[], double y[], int M)
{
  // NBF-elements discrete difference
```

```

double d[NBF];
delay(x, d, M);
for (int i = 0; i<NBF; i++)
    {y[i] = x[i]- d[i];}
}

```

The accumulation part as IIR:

```

void iir(double x[], double y[],
         double b0, double b1, double a1)
{
    // First-order generic IIR filter
    double k[NBF];
    y[0] = b0*x[0];
    for (int i = 1; i < NBF; i++)
        {k[i]=b0*x[i]+b1*x[i-1];
         y[i] = k[i] - a1*y[i - 1];}
}

```

And finally the whole filter:

```

void trapz(double x[], double y[],
           double beta, int R, int M)
{
    // Trapezoidal filter
    // Initialisation of partial-result arrays
    double p1[NBF];
    double p2[NBF];
    double p3[NBF];
    double p4[NBF];
    // First two steps (FIRs)
    differentiator(x, p1, R);
    differentiator(p1, p2, (R + M));
    // Third and fourth steps (IIRs)
    double b0_1 = 0;
    double b1_1 = 1;
    double b0_2 = 1;
    double b1_2 = -beta;
    double a1 = -1;
}

```

```
iir(p2, p3, b0_2, b1_2, a1);
iir(p3, p4, b0_1, b1_1, a1);
// Renormalisation
for (int i = 0; i < NBF; i++){
    {y[i] = p4[i] / ((double)R);}
}
```

In the code, R is the rise time, M the flat top, β is defined by the signal exponential decay and NBF is the waveform samples number.

The zero cross of the signal derivative is used for the peak detection (as for the current "quicklook" code) thus, for the peak time of arrival. The filters parameters define the pile-up rejection window $(R + M)$.

This kind of algorithm can be easily implemented in hardware thanks to FPGA devices. The hardware implementation permits a real on-line analysis and possibly data reduction. In fact, if the performances will be as good as the off-line analysis (see next section) we can imagine having as DAQ output only the energy and time of arrival of each X-ray peak instead of the full waveform. By the final measurement start we are planning a set of tests to verify these assumptions and finally switch to the new faster DAQ.

4.9.2 Off-line analysis

Most of the analysis is made off-line by the data processing software, called FAMUAnalysis written in C++ making use of the ROOT toolkit. Three different kinds of analysis were developed to specifically deal with the fast LaBr₃ detectors or the slow high-resolution HpGe detectors. Still, most of the routines are in common with the two kind of detectors and the flow can be resumed as follow:

- for each detector and each time window (trigger), the waveform is extracted from the ROOT file;
- a detector dedicated routine recognises the X-rays in each waveform giving as output several values such as the peak height, time of arrival, distance between the previous peak and so on...
- each peak height is converted from ADC value to energy and the sample-time in time;
- all these data are stored in a single "level 2" (L2) root files. Each branch of this file contains all data relative to one detector. This file contains the temperature information too and other important metadata.

The calibration is made possible by the acquisitions of a set of ⁵⁷Co, ¹³³Ba and ¹³⁷Cs radioactive sources spectra. This procedure is made at the beginning and at end of each data taking, to evaluate possible variations in the system response.

The L2 output can be imagined as a matrix where all the information needed to extract the transfer rate, or more in general, to perform further phenomenological analysis are stored.

HpGe analysis routines

For the Ortec 672 shaped HpGe signals, where the waveform can be occupied mainly by only one X-ray peak due to the total peak duration ($\approx 9.6\mu\text{s}$ see section 4.7), only the first maximum (with respect to the computed baseline average) of the waveform is taken as a valid X-ray to avoid spectrum contamination by piled-up events. From these data, the software can draw only the X-rays energy spectrum. The routines related to the fast shaped and pre-amplified GEM-S HpGe detector

are similar to the "quicklook" routine. The main difference is in the energy reconstruction, in fact, it is measured by the difference between each local maximum and the previous local minimum in the waveform. In this way, piled-up events are recognised and their energy is roughly reconstructed.

On top of the peak height and time of arrival, the system automatically computes the time distance between two successive peaks and recognizes if the signal saturates the DAQ dynamic range. This is made by simply checking if the signal reaches the $2^{N_{bit}}$ ADC channels limit. The beginning and the end of the saturated signal is computed and with all the other data, stored in the corresponding matrix element of the L2 file.

From these data, the software can draw the energy and time spectra. By counting the saturated signals durations, it can estimate the timing detection efficiency of the whole acquisition window. Moreover, we can put some conditions in the time distance between two peaks, actuating cuts. This is particularly indicated when we need the best energy resolution but losing statistic. The detection efficiency is then recalculated and it is fundamental to make a proper dead time correction.

LaBr₃ analysis routines

The main detectors of the experiment are the fast LaBr₃ crystal based ones. Because of their positioning (very close to the maximum muons deposition), they face with most of the X-rays generated. This leads to a very high rate condition where multiple events are detected in a single waveform. For instance, in Fig. 4.54 shows a typical waveform where ten X-ray events are recorded in $\approx 5 \mu\text{s}$. This clearly shows that the majority of events, occurs in the first microsecond (prompt phase see chapter 3) and, despite the signal short duration, the pile-up condition still happens.

As shown in the section dedicated to LaBr₃ detection system (see section 4.6), the PMT output signal is only slightly filtered thus, electronic noise coming from the PMT itself and from the power supply still affects the signal. For this reason, and to totally disentangle piled-up events (thus reducing the dead time) we implemented an approach totally different from the previous ones.

The routine involved in the analysis of these data is based on a fitting algorithm. Each X-ray signal is fitted with a function representing the signal shape. The fitting shape was obtained by averaging ten thousand single X-ray photon peaks

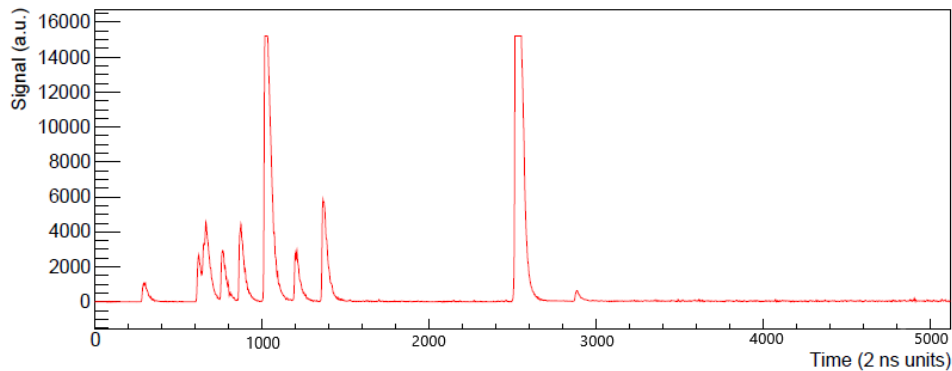


Fig. 4.54 Typical on-beam LaBr₃ waveform.

and it results in a sigmoid (for the rising part of the signal) followed by a landau distribution shape.

In the case of a pile-up, a sum of signal shapes is used in order to correctly estimate the energy of each detected X-ray (Fig. 4.55). Moreover, fitting the signals results in a decreased impact of high-frequency oscillations that affect the final energy resolution.

The fitting routine output consists of the pulse height, the degrees of freedom of the fitting and the reduced chi-squared ($\bar{\chi}^2$).

By the derivative zero crossing, the time of arrival and the distance between two successive peaks is computed too.

As for the previous case (fast HpGE), saturation in the signal are recognised and their duration saved in the L2 file. From the related branch in the L2 file, it is possible to draw the time and energy spectrum, compute several cuts based on the information carried out by the fitting routine or by the inter pulses time distance.

A typical time spectrum is shown in Fig. 4.56. Three different zones can be clearly distinguished:

- 1 Pre-trigger in the 0–400 ns interval. It is a low counting zone right before the muon beam arrival.
- 2 Prompt in the 400–1000 ns interval. It corresponds to the prompt phase described in section 3. The beam interacts with the target producing muonic atoms emitting characteristic X-rays. The two peaks correspond to the muon

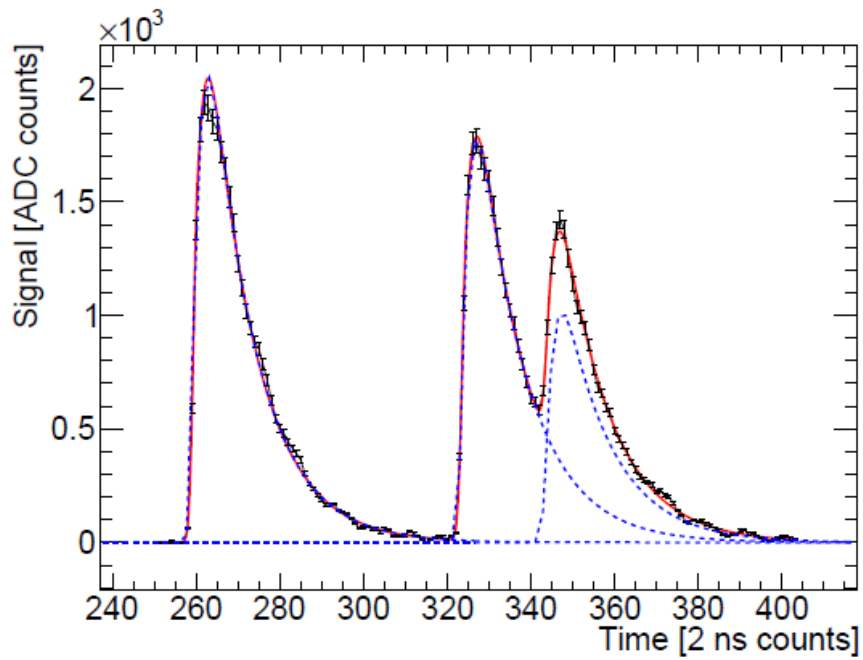


Fig. 4.55 Single pulse and piled-up pulses and the relative fit (red line). The pile up is successfully disentangled (blue dotted dash) [18].

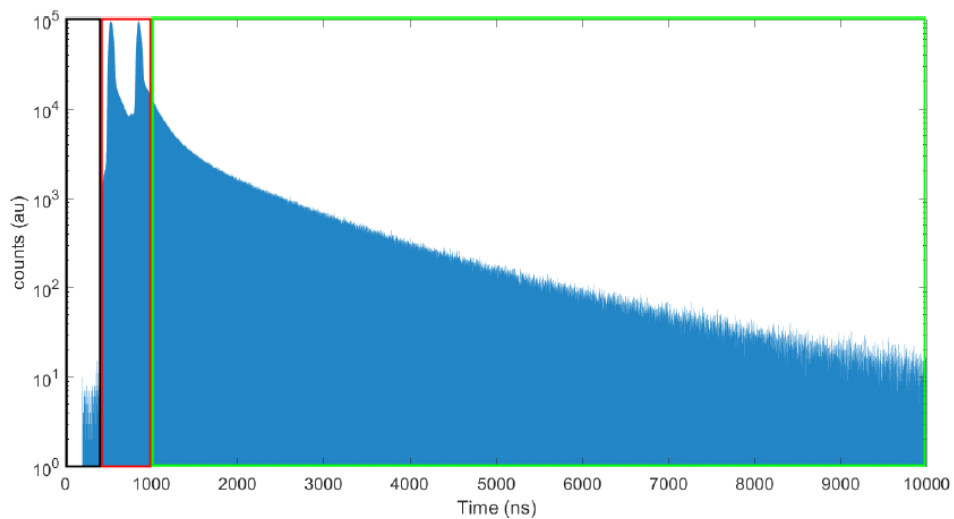


Fig. 4.56 Time spectrum of X-rays detected by LaBr₃ detector. Three zone can be identified: in the black box, the pre trigger with no counts. In the red box, the prompt zone where the beam interacts with the target and the beam time distribution appears evident. In the green box, the delay phase [18].

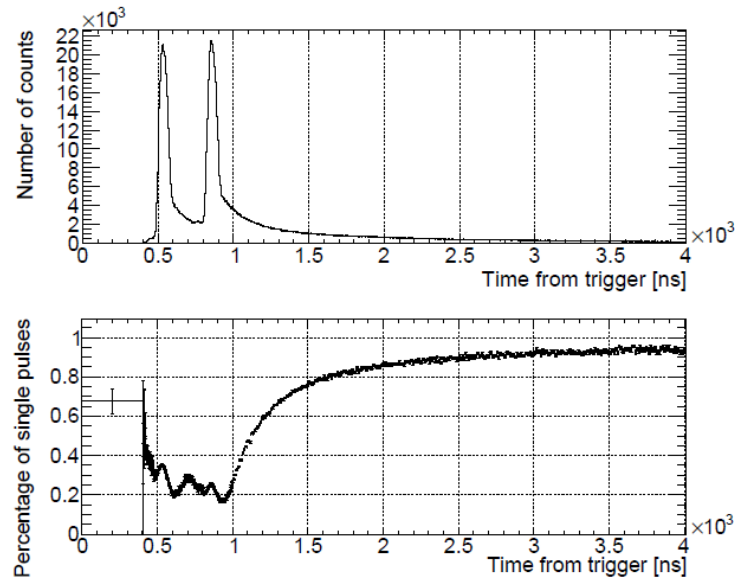


Fig. 4.57 Top panel: Time spectra of detected X-rays by LaBr₃ detector. Bottom panel: percentage of single pulses (single X-ray photon) versus time. [30].

arrival time and they have the same profile of the muon beam, i.e. 70 ns FWHM and separation of 320 ns, as shown in Fig. 4.3.

- 3 Delay in the 1000 ns – 10 μ s. In this part of the time spectrum, the emitted X-rays depends on the muon transfer.

While the most interesting zone for the FAMU purposes is the delayed one, during prompt the detectors have to face with multiple photons. In Fig. 4.57 is shown the probability to find only one X-ray photon with respect to the time distance from the trigger.

Data selection and dead time correction

In order to reliably measure the transfer rate, the detection efficiency has to be time-independent in the delayed phase. The detection efficiency over time depends on various factors and corresponds to the live time definition. As a first approximation, considering the pile-up rejection efficiency perfect, it is only due to signal time duration and possible saturation. Set the maximum detectable energy at 800 keV when a more energetic photon (or a charged particle) interacts with the detector it

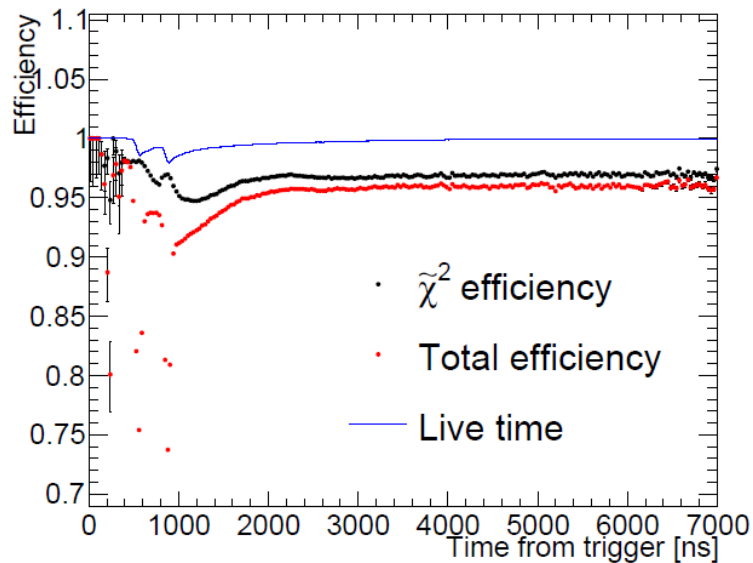


Fig. 4.58 In blue the efficiency curve versus time of LaBr₃ detectors due to saturate events only. In black, the resulting efficiency after imposing $\tilde{\chi}^2 < 100$ of the peaks fit. In red the total efficiency, the reader can notice that in the thermalized phase (above 1200 ns) it remain stable [30].

results in saturation. During the entire time in which the system is saturated, it isn't able to detect other photons thus, results in a reduction of live time (blue line in Fig. 4.58).

When 2 photons occur simultaneously (with a time distance below the signal rise time) is impossible to discern the two peaks, thanks to the 12 ns rise time, this condition is very unlikely for LaBr₃, simulations suggest.

By using selection rules on the signal, for instance imposing that the fit $\tilde{\chi}^2$ is less than a certain value (black line in Fig. 4.58), it results in an increase of the dead time. For our measurements with LaBr₃ detectors, we imposed a time distance between successive peaks of at least 30 ns, discarding all the others. This is reflected in a $\tilde{\chi}^2 < 100$ in the whole time range. The final live time is shown in red in Fig. 4.58 and it is in the 93%–96% range in the thermalized phase. Less than 2% of the total data are discarded by this selection [18]. As comparison, Fig. 4.59 shows the efficiency correction curve applied to the fast shaped HpGe detector by saturated events elimination and rise time correction.

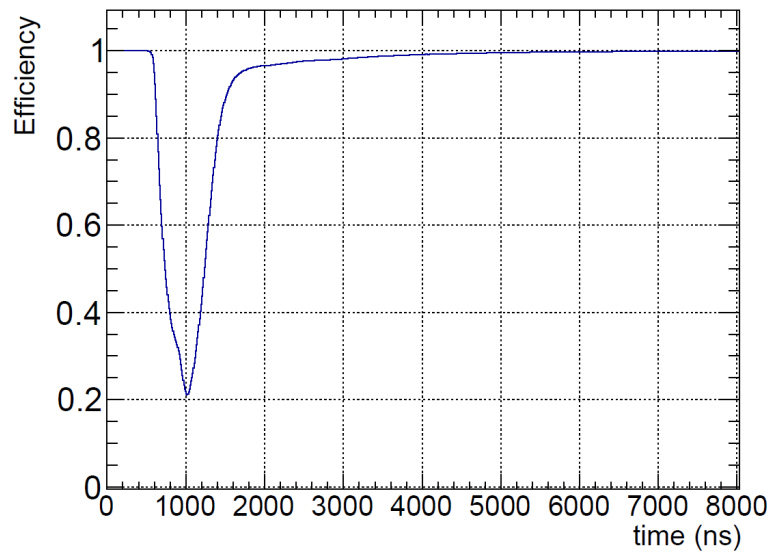


Fig. 4.59 Efficiency versus time for fast shaped HpGe detector. During the prompt phase, the efficiency drop down to 20% [26].

Final spectra and background subtraction

After the selection, the energy spectrum appears as shown in Fig. 4.60 where the muonic X-ray lines of nickel, oxygen, and aluminium are well identifiable. The 511 keV coming from the electron-positron annihilation is due to the environmental background and it is always present in our measurements. After 1200 ns from the beam trigger, the gas thermalizes and the spectrum changes. All the target vessel composing materials muonic lines disappear. Only the muonic oxygen k_α , k_β and k_γ (cluster together) remain visible (Fig. 4.61).

The spectra of all the detectors are merged together. Then the delayed part of the resulting spectrum is split into up to 20 bins (it depends on the overall statistics), from 1200 ns to 100000 ns.

To evaluate the amount of produced muonic oxygen, the integral of the relative k_α , k_β and k_γ must be calculated. The two peaks (k_α and k_β plus k_γ that are clustered together) must be isolated from the background photons, in order to properly integrate the counts above them. We evaluated the background by taking a set of low statistic measurements with pure hydrogen (in the 2017 data taking) inside the target and varying the temperature. The obtained spectra were smoothed with a Gaussian kernel filter (to avoid fluctuations due to the poor statistic as shown

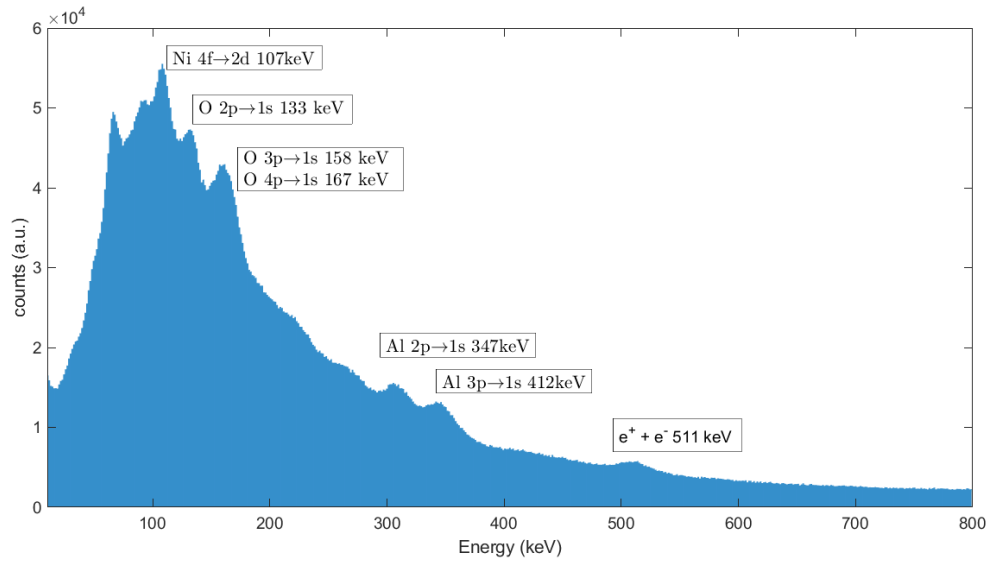


Fig. 4.60 Total spectrum, without time cut. All the prompt muonic lines due to the interaction between muons and the aluminium, nickel coated target vessel are visible.

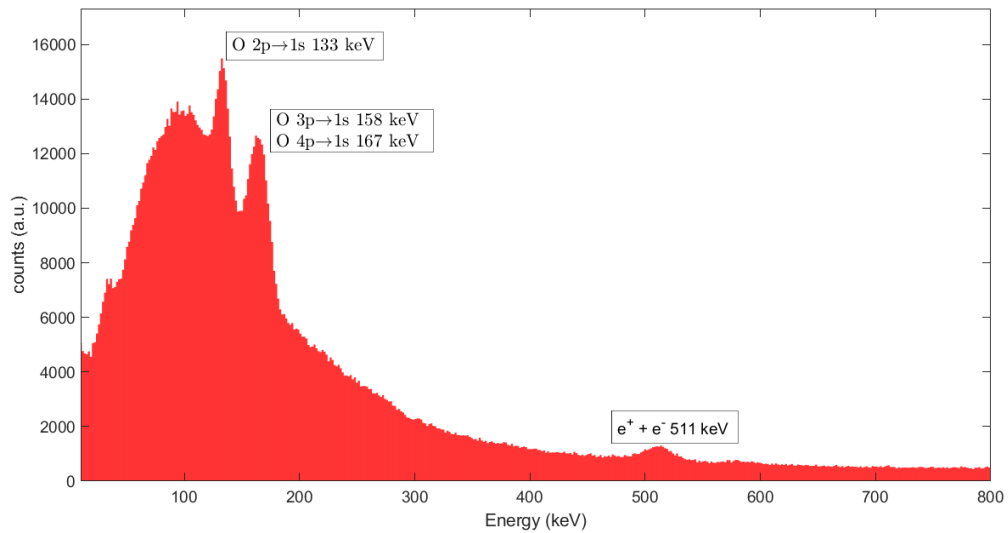


Fig. 4.61 Total delayed spectrum of muonic oxygen. The muonic oxygen k_α , k_β and k_γ (cluster together) appear well distinguished from the background.

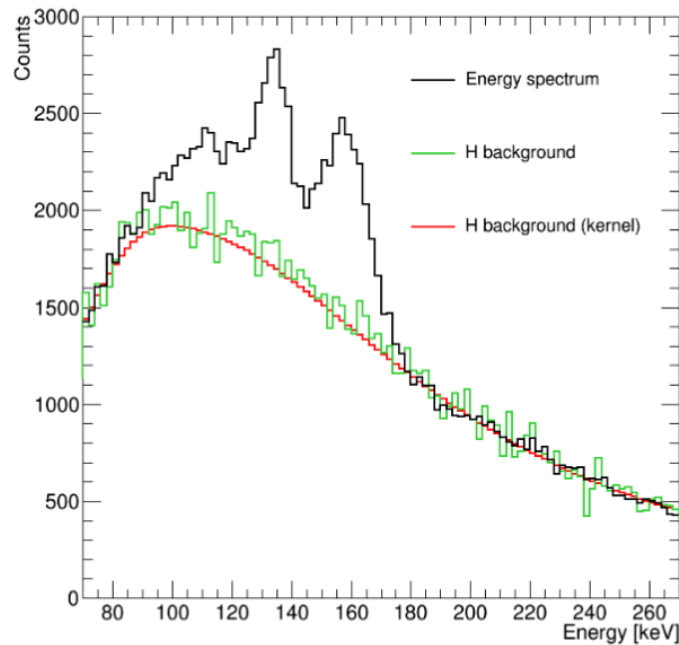


Fig. 4.62 In black a delayed spectrum of muonic oxygen X-rays. In green the pure hydrogen spectrum smoothed with a Gaussian kernel in red. This last one is considered background and is subtracted to the oxygen spectrum.

in Fig. 4.62).

In order to subtract the background to the 20 spectra (one for each time bin), it was normalized in the 200–400 keV region where no oxygen signal is expected.

After this procedure, for each time bin, the remaining muonic oxygen peaks are integrated. As shown in Fig. 4.63, where three different time bins are showed, even after the background subtraction, a small peak structure is still visible. This is probably due to the 120 keV ^{16}Ni γ -ray generated by the oxygen nuclear capture (see section 1.6).

In order to extract the transfer rate, we count the number of muonic oxygen X-rays over time. To do so, the integral of the resulting spectrum from the background subtraction is computed. The integration range we choose is 125–180 keV in order to avoid the low energy structure. The error associated with this subtraction procedure was evaluated time bin per time bin by changing the normalization energy range and the Gaussian kernel weights. These tests permitted us to estimate the effect of this systematic between 5% and 20% on the integrated signal spectrum (depending on the time bins statistic) [30].

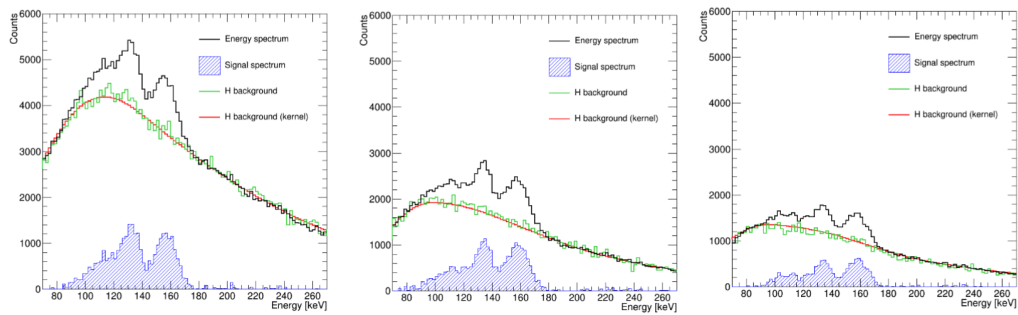


Fig. 4.63 Energy spectrum of three different delayed time bins. The results of the background subtraction shows the muonic X-ray lines and a small structure at low energy, probably due to nuclear capture processes.

Part III

Results and discussion

Chapter 5

Transfer rate to not thermalized gas mixtures: 2014 data

In 2014 we performed some preliminary test at Riken-RAL muon beam facility. The main goal of this test was the characterization of both the target and the X-ray detectors. Even though this was not devoted to the transfer rate mechanism study, the first attempts to calculate the transfer rate to CO₂, oxygen and argon will be shown.

The study was performed with a gas pressure of 38 bar at room temperature. With these conditions, the μp thermalizes in about 100 ns (see Fig. 3.3). With a CO₂ concentration of 4% (2% for argon), the muon transfer occurs at times well below 100 ns, thus, in an epithermal uncontrolled condition. The kinetic energy of muonic hydrogen during the muon transfer can be assumed to be distributed as a sum of the two Maxwell-Boltzman distributions: one corresponding to the gas temperature and the second one corresponds to the mean energy of 20 eV [31]. We were able to observe the muonic oxygen and argon X-ray lines (Fig. 5.1, Fig. 5.2).

The transfer mechanism is clearly shown by the comparison between the aluminium target prompt muonic X-ray lines and the oxygen (argon) ones. The first ones depend on the prompt interaction between the aluminium vessel (described in section 4.3.1) and the muon beam. The oxygen (argon) ones show a time delay of 5–10 ns in the emission time distribution, as shown in Fig. 5.3. The prompt aluminium signal from the target material (345 keV line) was chosen as a time reference.

Let's recall the equations 3.2, 3.4 and 3.7 in a more general formulation in

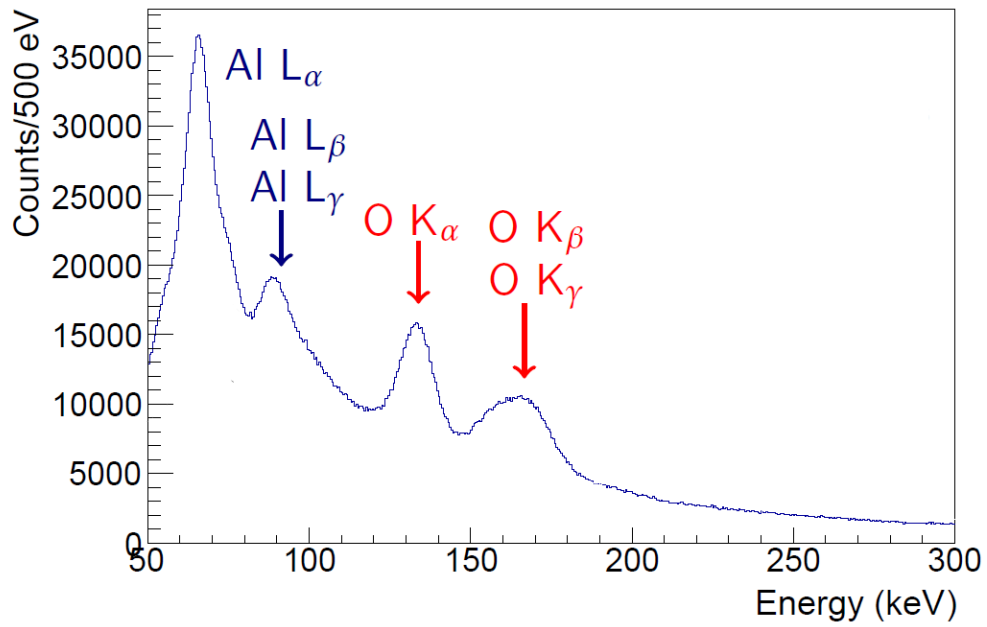


Fig. 5.1 2014 data taking, LaBr₃ mosaic H₂+CO₂(4%) spectrum.

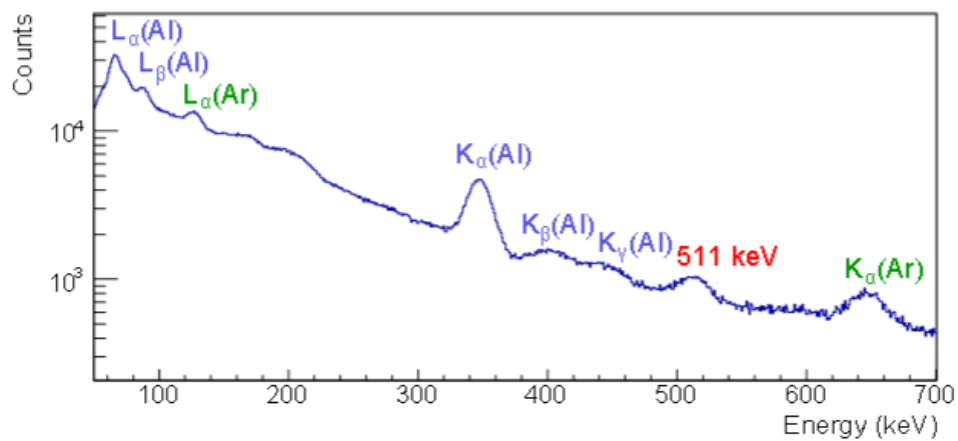


Fig. 5.2 2014 data taking, LaBr₃ mosaic H₂+Ar(2%) spectrum [17].

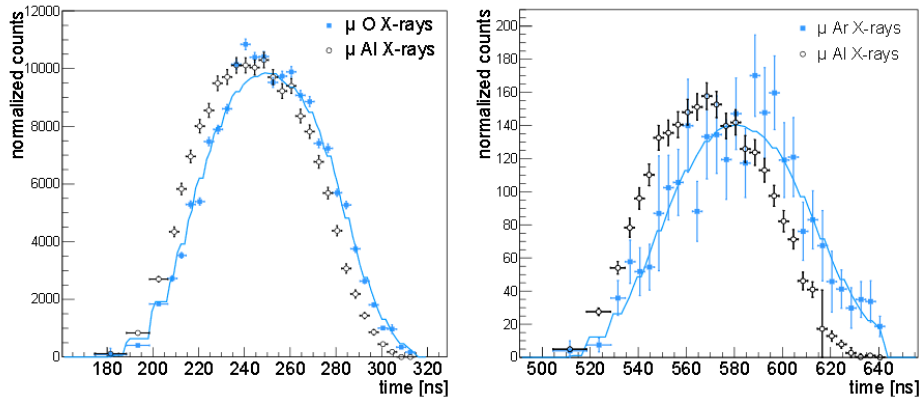


Fig. 5.3 Time distribution of aluminium and oxygen (on the left) or argon (on the right). A difference of $\approx 5-10$ ns is visible [31].

order to consider CO_2 and argon mixtures:

$$\lambda_{dis} = \lambda_0 + \phi(c_p \Lambda_{pp\mu} + c_d \Lambda_{pd} + c_{Z_1} \Lambda_{pZ_1} + c_{Z_2} \Lambda_{pZ_2} + \dots), \quad (5.1)$$

where the difference with respect to the equation 3.2 is in the last two more general terms. The equation 3.7 becomes:

$$dN_{pZ_i}(t) = c_{Z_i} \Lambda_{pZ_i} N_{\mu p}(0) e^{-\lambda_{dis} t} dt. \quad (5.2)$$

A fit of the CO_2 (oxygen and argon) X-rays time evolution can be performed by the numerical integration of this last equation and by substituting the various concentrations and disappearing rates present in Table 5.1, we can compute the transfer rate. The final results are:

- $\Lambda_{\text{CO}_2} = 405.3 \pm 1.5(\text{stat})_{-111}^{+255}(\text{sys})$;
- $\Lambda_{\text{O}} = 186.4 \pm 6.0(\text{stat})_{-52}^{+118}(\text{sys})$;
- $\Lambda_{\text{Ar}} = 289 \pm 18(\text{stat})_{-80}^{+181}(\text{sys})$.

The systematic uncertainties come from different contributions:

- 16% from the background subtraction technique;
- 2% from the temperature estimation;
- 3% from the concentration of the gas mixtures.

Transfer rate to	Gas mixture	Concentration	Free parameter	Fixed parameters
CO ₂	H ₂ + 4% CO ₂	$c_C \Lambda_{CO_2}$ $=c_C(\Lambda_{pC} + \Lambda_{pO})$	Λ_{pC_2}	$c_e=(9.5\pm 0.3)\times 10^{-4}$ $c_O=2c_C$ $c_{d(H_2+CO_2)}=(1.358\pm 0.001)\times 10^{-4}$ $c_p=1-c_C-c_O-c_{d(H_2+O_2)}$
Oxygen	H ₂ + 4% CO ₂	$c_C \Lambda_{pC} + c_O \Lambda_{pO}$	Λ_{pO}	$\Lambda_{pC}=(5.1\pm 1.2)\times 10^{-10} \text{ s}^{-1}$ $c_e=(9.5\pm 0.3)\times 10^{-4}$ $c_O=2c_C$ $c_{d(H_2+CO_2)}=(1.358\pm 0.001)\times 10^{-4}$ $c_p=1-c_C-c_O-c_{d(H_2+O_2)}$
Argon	H ₂ + 2% Ar	$c_{Ar} \Lambda_{pAr}$	Λ_{pAr}	$c_{Ar}=(5.1\pm 0.1)\times 10^{-4}$ $c_{d(H_2+Ar)}=(1.355\pm 0.001)\times 10^{-4}$ $c_p=1-c_{Ar}-c_{d(H_2+Ar)}$

Table 5.1 Values needed to compute the transfer rate. They come from multiple references such as [37] and [38], and [39]. For the deuterium concentration, we measured in laboratory the tested gas.

As described previously, our measurements were taken with not-thermalized μ ps. It implies a wide range of available energy distributions of which it is not possible to experimentally estimate an average [31]. This range is reported in the results figure as a horizontal "error bar". The systematic uncertainties are reported as shaded regions surrounding the resulting values (Fig. 5.4).

To summarize, we were able to measure the transfer rate from hydrogen to CO₂ and oxygen in a H₂+CO₂(4%) gas mixture, and to argon in a H₂+Ar(2%) mixture, in a not thermalized condition. The results are higher than previous measurements found in literature, due to a highly variable level of epithermicity and to the possible presence of a fraction of prompt component in the X-rays signal spectra. We can say that our values can be interpreted as upper limits to the transfer rate from hydrogen to these elements [31].

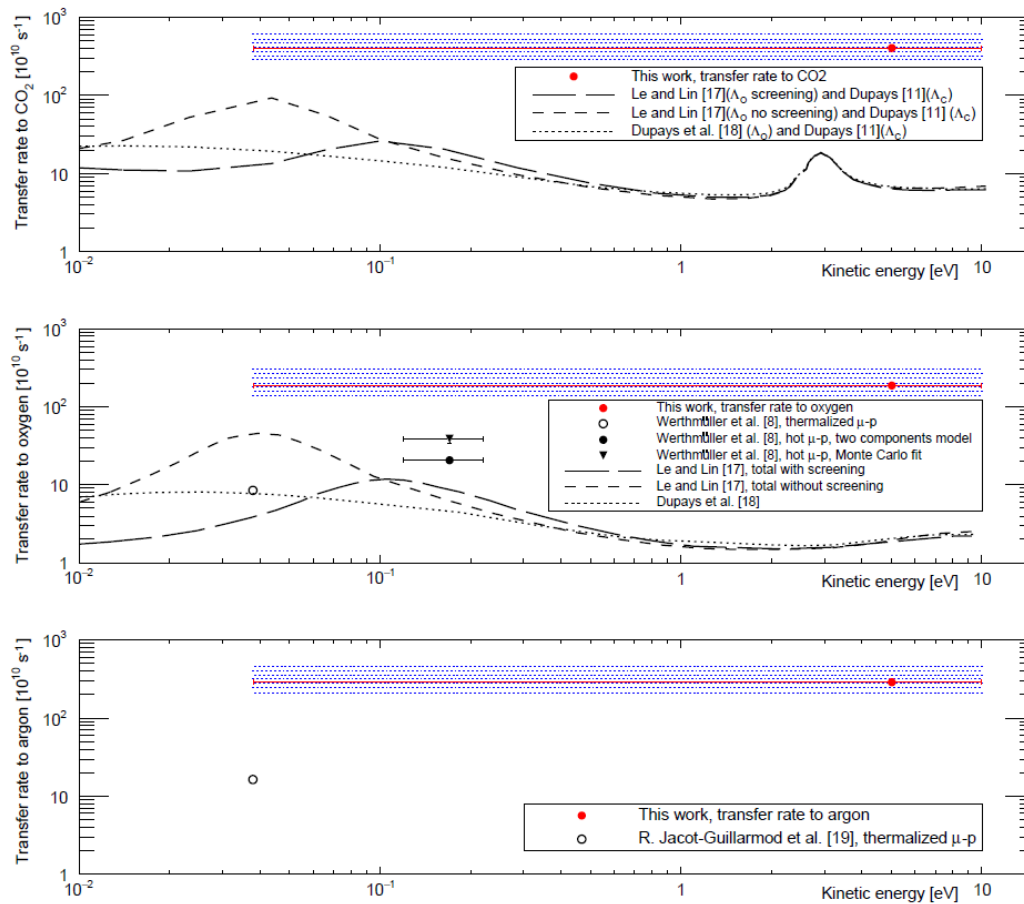


Fig. 5.4 Transfer rate measurement results in a non thermalized gas mixture, relative, from top to bottom, to CO₂, O₂ and Ar. The shaded region reflects the systematic uncertainties while the long horizontal error bar reflect the unknown μ p energy distribution. Comparison with data [5] and models [6], [32] in literature [31].

Chapter 6

Transfer rate to thermalized oxygen gas mixture: 2016 data

The first 2014 data taking was devoted to studying the setup performances during the measurement campaign. We faced multiple problems in the detection system reliability even though, after long data analysis, we were able to estimate an upper limit to the transfer rate in a high epithermicity gas condition.

In 2016, after the detectors and target upgrades, we performed a data taking campaign at RAL devoted to measuring the transfer rate from hydrogen to oxygen at various temperature and oxygen concentrations.

We performed 18 hours of acquisition at six different temperatures for the H_2+O_2 (0.3%) gas mixture and 9 hours, at three different temperatures for the H_2+O_2 (1%) gas mixture and 9 hours at three different temperatures for the H_2+O_2 (0.05%) gas mixture. The temperature steps in common are: 300 K, 273 K, and 240 K. For the first mixture, we also measured at a temperature of 200 K, 150 K and 100 K. For each temperature step, data were taken for 3 consecutive hours. A summary is in Table 6.1.

gas mixture (concentration)	p_{beam} (MeV/c)	temperature steps (K)	data taking	filling at
H_2O_2 (0.3%)	57	300/273/240/ 200/150/100	3 h/step	41 bar 300 K
H_2O_2 (0.05%)	57	300/273/240	3 h/step	41 bar 300 K
H_2O_2 (1%)	57	300/273/240	3 h/step	41 bar 300 K

Table 6.1 Summary of the 2016 data taking measurements at RIKEN-RAL (RB852).

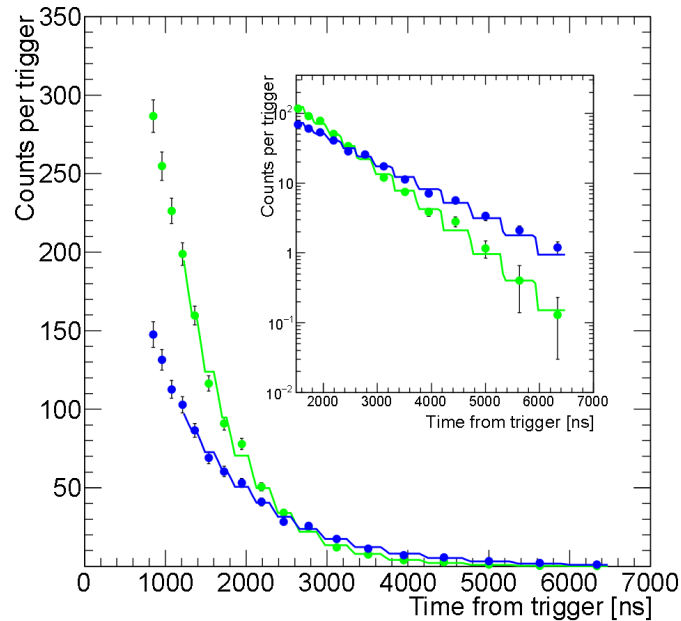


Fig. 6.1 Time dependence of the oxygen signal at 300 K (green) and 100 K (blue). The points represent the counts at each time bin below the k_α and $k_\beta+k_\gamma$ clustered peaks. The solid lines are the respective fit to the data following equation 3.7. In the inset, a zoom in logarithmic scale [30].

During the data taking the temperature was constantly monitored and saved.

The number of muonic oxygen X-rays is computed at each time bin after the gas thermalization in the delayed phase (see section 4.9.2 in particular Fig. 4.63 to help the visualization). A fit of the oxygen X-rays time evolution can be performed numerically integrating the equation 3.7 leaving as free parameter Λ_O thus, we are able to extract the muonic hydrogen to oxygen transfer rate.

In Fig. 6.1 is shown the number of muonic oxygen versus time for the 0.3% gas mixture at two different temperatures. Each step represents the number resulting from the counts below the oxygen peaks after the background subtraction for each time bin. Each vertical error bar, includes both statistical and background systematic errors summed quadratically. The green and blue solid lines indicate the transfer rate fit. The two temperatures slopes clearly show two different distributions, corresponding to different transfer rate.

We performed other consistency checks by, for instance, considering only the muonic oxygen k_α or the $k_\beta+k_\gamma$ cluster, without noticing significant changes but in

the associated error due to the poorer statistic.

The transfer rate error is evaluated by summing all the contributions. The most important is due to the gas mixture concentration. The gas supplier certifies a 3% of error in the gas mixture made by weight. To convert this in atomic concentration, needed in the equation 3.7, we need the gas pressure. However, the gas filling procedure was erroneously performed without a precise pressure reading. Thus, we associated a total 3% to the oxygen concentration contribution.

All the other error contributions are from the literature values of $\lambda_{pp\mu}$, λ_0 and λ_{pd} that are below 1%.

The results for the 0.3% mixture are shown in Fig. 6.2. For the only three upper temperatures for the 0.05% mixture in Fig. 6.3, and for the 1% mixture in Fig. 6.3. In the last two figures, the 0.3% results are shown for the intermediate temperature too. This was possible due to the time the target needs to be cooled down. During this time we kept acquiring data in the 0.3% gas mixture case and, the extracted transfer rate was fixed at the average temperature of the gas. This is reflected in bigger error bars.

It worth noting to notice that for the 0.05% oxygen concentration mixture, the resulting values are quite different from the others, moreover the error bars are far bigger. This is due to the small amount of oxygen itself. The number of muonic oxygen X-ray lines is proportional to the concentration of oxygen in the gas mixture. Thus, the resulting values reflect such low counts. To visualize it, see Fig. 6.5.

For the 0.3% mixture, we performed an in deep analysis with the fast amplified GEM-S HpGe detector and the result is shown in Fig. 6.6.

To summarize the information in the multiple graphs: we successfully extrapolated the transfer rate from muonic hydrogen to oxygen in three different concentrations of gas mixtures. The results agree inside the uncertainty limits at least for the 0.3% and 1% concentrations. Moreover using an independent and non-optimized kind of detection system (fast shaped HpGe GEM-S) we obtained consistent results. All these are in good agreement with the only measurement presents in the literature (ref [33]).

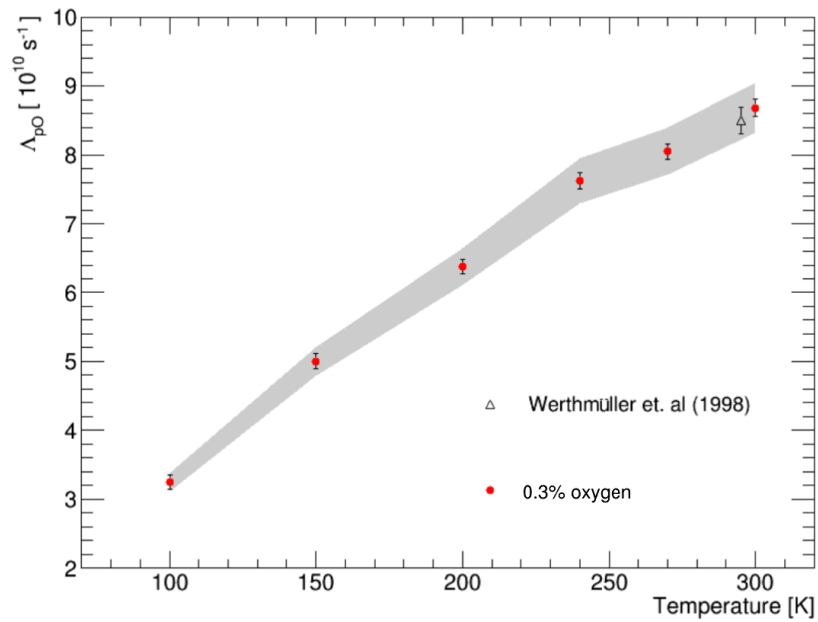


Fig. 6.2 Transfer rate measurement versus temperature obtained with LaBr_3 detectors and 0.3% oxygen concentration. The shaded region represents the systematic uncertainty. Empty small triangle is the measure from [33].

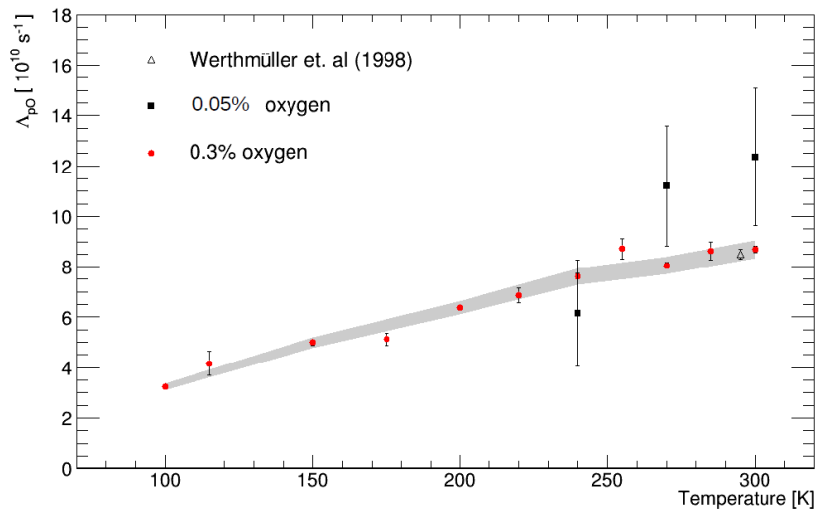


Fig. 6.3 Transfer rate measurement versus temperature obtained with LaBr_3 detectors and 0.3% oxygen concentration (red dots). The shaded region represents the systematic uncertainty. Empty small triangle is the measure from [33].

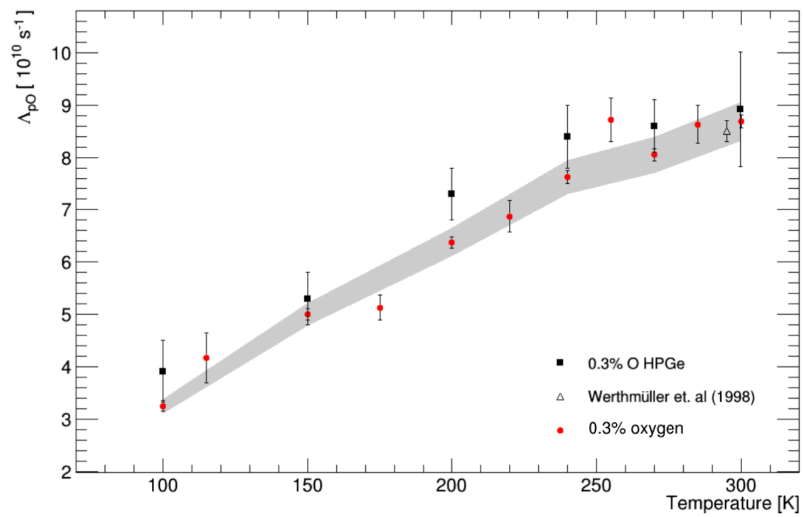


Fig. 6.6 Transfer rate measurement versus temperature obtained with fast amplified GEM-S Hpghe detector and 0.3% oxygen concentration (black dots). The red dots are from LaBr_3 and the shaded region represents the systematic uncertainty of this last results. Empty small triangle is the measure from [33].

Chapter 7

Comparison with the models and discussion

The transfer rate measurement is fundamental to define the operative conditions in terms of temperature and pressure, in which we want to perform the measurement of the hyperfine splitting of the muonic hydrogen at the ground state.

The models present in the literature are not in agreement (see Fig. 1.13 in section 1.7). In particular, in the low energy region (0.01–0.1 eV) where the epithermicity generated by the laser-induced spin-flip transition, can increment the transfer rate of the maximum possible value.

This increment is translated in a bigger difference in the muonic oxygen X-rays emission between the laser excited situation and without the spin-flip process. This leads to an increased sensitivity of the experimental technique.

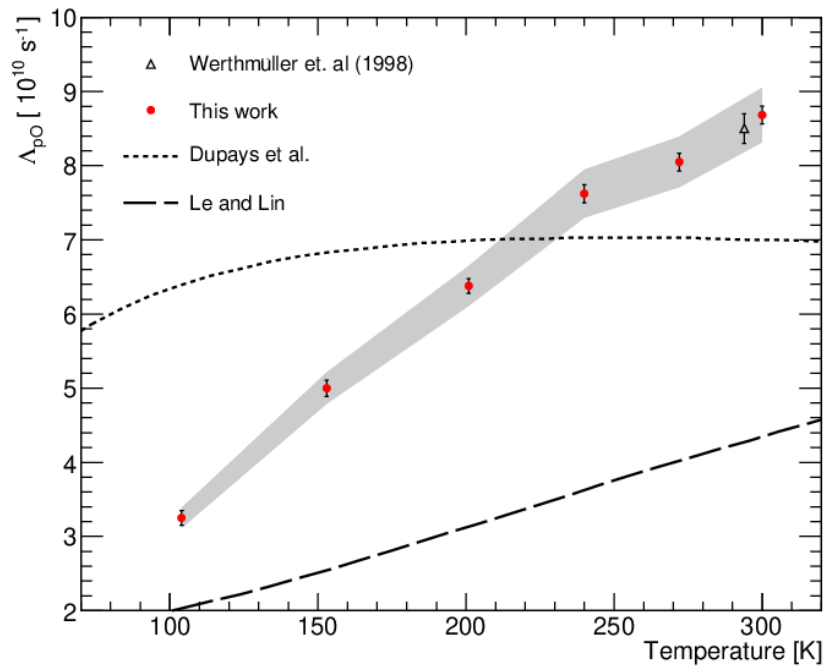


Fig. 7.1 Transfer rate versus temperature. Our results are in red while the only other measurement is from [33] in the empty triangle. The two models [6] and [32] present in literature are shown as well [34].

We choose to fit our results (shown in Fig. 7.1) with a parabola shape. The motivations behind this shape choice are: high degree polynomial fits are more sensitive to the unknown behaviour of the transfer rate at epithermal energies. Moreover, the parabola has smaller uncertainties and appears to be much more reliable [88]. The resulting fitting function for the oxygen transfer rate as function of the temperature is:

$$\lambda_{pO}(T) = p_1 + p_2T + p_3T^2, \quad (7.1)$$

with:

$$p_1 = (-1.3 \pm 0.4) \times 10^{10} s^{-1} \quad (7.2)$$

$$p_2 = (5.0 \pm 0.5) \times 10^8 s^{-1} K^{-1} \quad (7.3)$$

$$p_3 = (-5.5 \pm 1.2) \times 10^5 s^{-1} K^{-2}. \quad (7.4)$$

The chi squared results to be very good: $\chi^2 = 1.08$.

Using the Maxwell-Boltzmann relation from temperature to energy and fitting our results we can deduce the trend of the transfer rate with respect to energy Fig. 7.2.

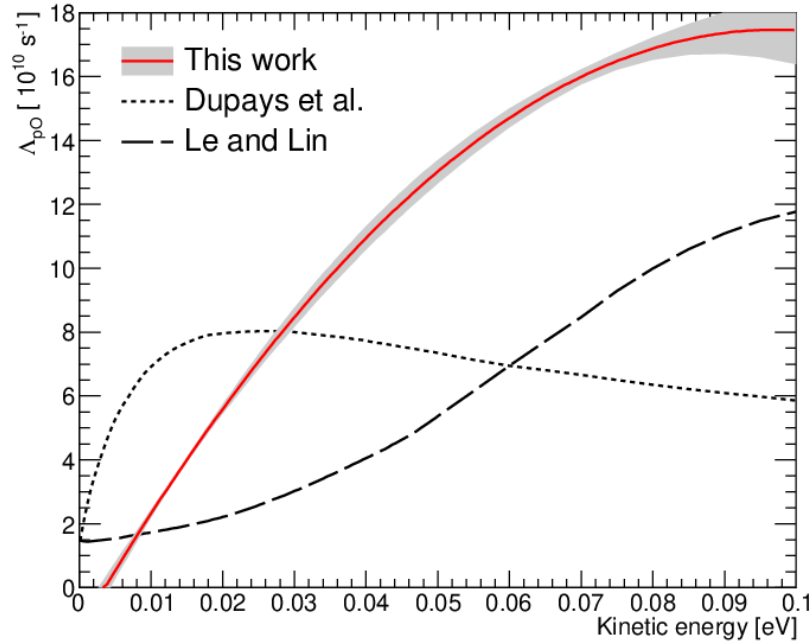


Fig. 7.2 Transfer rate versus energy. The parabola fitting of our results is shown in red while the dashed and dotted lines are respectively from [6] and [32] [34].

The transfer rate as function of energy $\lambda_{pO}(E)$ has the same parabolic shape:

$$\lambda_{pO}(E) = P_1 + P_2 T + P_3 T^2, \quad (7.5)$$

with:

$$P_1 = (-1.3 \pm 0.4) \times 10^{10} s^{-1} \quad (7.6)$$

$$P_2 = (3.8 \pm 0.4) \times 10^8 s^{-1} eV^{-1} \quad (7.7)$$

$$P_3 = (-2.0 \pm 0.4) \times 10^5 s^{-1} eV^{-2}. \quad (7.8)$$

By converting the energy into temperature, we can compare the Le and Len [6] and Dupays et al. [32] calculations with our results (Fig. 7.1).

It seems clear that at lower gas energies, the laser-induced effect is bigger. However, we have to take in mind the O_2 molecules critical point is at 54.33 K. In order to cool down the new target with liquid nitrogen (77 K) we plan to operate at 80 K. As shown in section 3, where the experimental strategy is described, our idea is to shoot the laser when the μ ps are fully thermalized. Reminding that the

thermalization process ends in t_0 (see equation 3.1) from the μp production we must increase the gas pressure to keep this time small. At lower times, the μp population is bigger thus, the laser light can interact with more μps . Again, to avoid oxygen condensation we choose to operate at a gas pressure of 80 bar.

Conclusions

The measurements of the Zemach radius with muonic hydrogen spectroscopy could give a hint to the proton radius puzzle solution. This measure will act as a precise QED test and, the solutions to the puzzle could involve beyond the Standard Model theories.

The FAMU collaboration proposed a measurement method based on a controlled transfer mechanism of μp to oxygen by the laser excitation of the hyperfine splitting of the muonic hydrogen at ground state.

This ambitious project involves various scientific fields, such as muon physics, X-ray detection systems, signals and data analysis, laser systems and so on ... we have to deeply understand and manage to perform the measurement.

So far, we successfully investigated the transfer mechanism without the hyperfine splitting excitation in order to fix the operative conditions for the final measurements.

In the meantime we fully developed and tested the X-ray detection system and off-line data analysis solving different problems we encountered during this whole period.

It worth nothing to add that the performance improvements from the two data takings (and successive analysis) are impressive and clearly shown by the comparison between Fig. 5.4 and Fig. 7.2.

In the next phases, the laser system will be integrated with the new custom target designed to host the optical cavity.

I'd like to add that, as a personal note, nevertheless the misfortune during the 2017 and 2018 data takings, we were capable (thanks to our ability) to distillate all the informations possible from what we had. I'd like to say thanks to the collaboration members, for the possibility I had to be involved not only on the X-rays detection system, but in all fields concerning the experiment too.

References

- [1] Kanetada Nagamine. *What are muons? What is muon science?* Cambridge University Press, 2003.
- [2] DONALD E. GROOM, NIKOLAI V. MOKHOV, and SERGEI I. STRIGANOV. Muon stopping power and range tables 10 mev–100 tev. *Atomic Data and Nuclear Data Tables*, 78(2):183 – 356, 2001.
- [3] D.F. Measday. The nuclear physics of muon capture. *Physics Reports*, 354(4):243 – 409, 2001.
- [4] Françoise Mulhauser and Hubert Schneuwly. Systematic study of muon transfer to sulphur dioxide. *Hyperfine Interactions*, 82(1):507–512, Mar 1993.
- [5] A. Werthmüller, A. Adamczak, R. Jacot-Guillarmod, F. Mulhauser, C. Piller, L. A. Schaller, L. Schellenberg, H. Schneuwly, Y. A. Thalmann, and S. Tresch. Transfer of negative muons from hydrogen to oxygen. *Hyperfine Interactions*, 103(1):147–155, Dec 1996.
- [6] Anh-Thu Le and C. D. Lin. Muon transfer from muonic hydrogen to atomic oxygen and nitrogen. *Phys. Rev. A*, 71:022507, Feb 2005.
- [7] Private communication with Andrzej Adamczak.
- [8] S Schmidt, M Willig, J Haack, R Horn, Andrzej Adamczak, Marwan Ahmed, F Amaro, Pedro Amaro, F Biraben, P Carvalho, Tzu-Ling Chen, Luis Fernandes, Thomas Graf, Mauro Guerra, Theodor Haensch, Malte Hildebrandt, Y C. Huang, Paul Indelicato, L Julien, and Randolph Pohl. The next generation of laser spectroscopy experiments using light muonic atoms. 08 2018.
- [9] Randolph Pohl, Aldo Antognini, François Nez, Fernando D. Amaro, François Biraben, João M. R. Cardoso, Daniel S. Covita, Andreas Dax, Satish Dhawan, Luis M. P. Fernandes, Adolf Giesen, Thomas Graf, Theodor W. Hänsch, Paul Indelicato, Lucile Julien, Cheng-Yang Kao, Paul Knowles, Eric-Olivier Le Bigot, Yi-Wei Liu, José A. M. Lopes, Livia Ludhova, Cristina M. B. Monteiro, Françoise Mulhauser, Tobias Nebel, Paul Rabinowitz, Joaquim M. F. dos Santos, Lukas A. Schaller, Karsten Schuhmann, Catherine Schwob, David Taqqu, João F. C. A. Veloso, and Franz Kottmann. The size of the proton. *Nature*, 466:213 EP –, Jul 2010.

- [10] J. J. Krauth, K. Schuhmann, M. Abdou Ahmed, F. D. Amaro, P. Amaro, F. Biraben, J. M. R. Cardoso, M. L. Carvalho, D. S. Covita, A. Dax, S. Dhawan, M. Diepold, L. M. P. Fernandes, B. Franke, S. Galtier, A. Giesen, A. L. Gouvea, J. Götzfried, T. Graf, M. Guerra, J. Haack, T. W. Hänsch, M. Hildebrandt, P. Indelicato, L. Julien, K. Kirch, A. Knecht, P. Knowles, F. Kottmann, E.-O. Le Bigot, Y.-W. Liu, J. A. M. Lopes, L. Ludhova, J. Machado, C. M. B. Monteiro, F. Mulhauser, T. Nebel, F. Nez, P. Rabinowitz, E. Rapisarda, J. M. F. dos Santos, J. P. Santos, L. A. Schaller, C. Schwob, C. I. Szabo, D. Taqqu, J. F. C. A. Veloso, A. Voss, B. Weichelt, M. Willig, R. Pohl, and A. Antognini. The proton radius puzzle. *ArXiv e-prints*, June 2017.
- [11] D. Guffanti. The famu experiment: Measurement of muonic atoms spectra.
- [12] Dimitar Bakalov, Andrzej Adamczak, Mihail Stoilov, and Andrea Vacchi. Theoretical and computational study of the energy dependence of the muon transfer rate from hydrogen to higher-z gases. *Physics Letters A*, 379(3):151 – 156, 2015.
- [13] Isis neutron and muon source website. <https://stfc.ukri.org/research/our-science-facilities/isis-neutron-and-muon-source/>.
- [14] K. Nagamine, T. Matsuzaki, K. Ishida, I. Watanabe, R. Kadono, G. H. Eaton, H. J. Jones, G. Thomas, and W. G. Williams. Construction of riken-ral muon facility at isis and advanced μ sr. *Hyperfine Interactions*, 87(1):1091–1098, Dec 1994.
- [15] M. Bonesini, R. Bertoni, F. Chignoli, R. Mazza, T. Cervi, A. de Bari, A. Menegolli, M.C. Prata, M. Rossella, L. Tortora, R. Carbone, E. Mocchiutti, A. Vacchi, E. Vallazza, and G. Zampa. The construction of the fiber-sipm beam monitor system of the r484 and r582 experiments at the riken-ral muon facility. *Journal of Instrumentation*, 12(03):C03035, 2017.
- [16] M. Bonesini, R. Benocci, R. Bertoni, R. Mazza, A. deBari, A. Menegolli, M.C. Prata, M. Rossella, L. Tortora, E. Mocchiutti, A. Vacchi, and E. Vallazza. The upgraded beam monitor system of the famu experiment at riken-ral. *Nuclear Instruments and Methods in Physics Research Section A: Accelerators, Spectrometers, Detectors and Associated Equipment*, 2018.
- [17] A. Adamczak et al. Steps towards the hyperfine splitting measurement of the muonic hydrogen ground state: pulsed muon beam and detection system characterization. *JINST*, 11(05):P05007, 2016.
- [18] The FAMU collaboration. The layout of the famu (r582) experiment at ral to study the muon transfer rate from hydrogen to other gases in the epithermal range.
- [19] Private communication with Lyubomir Stoychev and Humberto Cabrera Morales.

- [20] G Bizarri and Pieter Dorenbos. Charge carrier and exciton dynamics in labr3:ce3+ scintillators: Experiment and model. 75:184302–184302, 05 2007.
- [21] Efficiency calculation for selected scintillator. <https://www.crystals.saint-gobain.com/sites/imdf.crystals.com/files/documents/efficiency-calculations.pdf>.
- [22] Radiation Protection and Environment web site. <http://www.rpe.org.in/>.
- [23] Ivan V. Khodyuk, Mikhail S. Alekhin, Johan T.M. de Haas, and Pieter Dorenbos. Improved scintillation proportionality and energy resolution of labr3:ce at 80k. *Nuclear Instruments and Methods in Physics Research Section A: Accelerators, Spectrometers, Detectors and Associated Equipment*, 642(1):75 – 77, 2011.
- [24] Suyama, Motohiro and Nakamura, Kimitsugu. Recent progress of photocathodes for pmts, 02 2010.
- [25] Photomultiplier tubes: basics and applications. third edition. https://www.hamamatsu.com/resources/pdf/etd/PMT_handbook_v3aE.pdf.
- [26] E. Furlanetto. Measurement of the muon transfer rate $\mu_p + z \rightarrow \mu z + p$ with the famu experiment.
- [27] R. Travaglini et al. A 1 GS/s sampling digitizer designed with interleaved architecture (GSPS) for the LaBr3 detectors of the FAMU experiment.
- [28] E. Gatti, P.F. Manfredi, M. Sampietro, and V. Speziali. Suboptimal filtering of $1/f$ -noise in detector charge measurements. *Nuclear Instruments and Methods in Physics Research Section A: Accelerators, Spectrometers, Detectors and Associated Equipment*, 297(3):467 – 478, 1990.
- [29] Tomasz Krakowski Zbigniew Guzik. Algorithms for digital γ -ray spectroscopy. *NUKLEONIKA*, 58(2):333 – 338, 2013.
- [30] E. Mocchiutti et al. FAMU: study of the energy dependent transfer rate $\Lambda_{\mu p \rightarrow \mu O}$. 2018.
- [31] Emiliano Mocchiutti et al. First FAMU observation of muon transfer from μp atoms to higher-Z elements. *JINST*, 13(02):P02019, 2018.
- [32] Arnaud Dupays, Bruno Lepetit, J. Alberto Beswick, Carlo Rizzo, and Dimitar Bakalov. Nonzero total-angular-momentum three-body dynamics using hyperspherical elliptic coordinates: Application to muon transfer from muonic hydrogen to atomic oxygen and neon. *Phys. Rev. A*, 69:062501, Jun 2004.
- [33] A. Werthmüller, A. Adamczak, R. Jacot-Guillarmod, F. Mulhauser, L.A. Schaller, L. Schellenberg, H. Schneuwly, Y.-A. Thalmann, and S. Tresch. Energy dependence of the charge exchange reaction from muonic hydrogen to oxygen. *Hyperfine Interactions*, 116(1):1–16, Mar 1998.

- [34] FAMU internal communications to be published soon.
- [35] A. Dupays, A. Beswick, B. Lepetit, C. Rizzo, and D. Bakalov. Proton Zemach radius from measurements of the hyperfine splitting of hydrogen and muonic hydrogen. *Physical Review A*, 68(5):052503, November 2003.
- [36] Caen s.p.a. website. <http://www.caen.it/>.
- [37] V. A. Andreev, T. I. Banks, R. M. Carey, T. A. Case, S. M. Clayton, K. M. Crowe, J. Deutsch, J. Egger, S. J. Freedman, V. A. Ganzha, T. Gorringer, F. E. Gray, D. W. Hertzog, M. Hildebrandt, P. Kammel, B. Kiburg, S. Knaack, P. A. Kravtsov, A. G. Krivshich, B. Lauss, K. R. Lynch, E. M. Maev, O. E. Maev, F. Mulhauser, C. Petitjean, G. E. Petrov, R. Prieels, G. N. Schapkin, G. G. Semenchuk, M. A. Soroka, V. Tishchenko, A. A. Vasilyev, A. A. Vorobyov, M. E. Vznuzdaev, and P. Winter. Measurement of the formation rate of muonic hydrogen molecules. *Phys. Rev. C*, 91:055502, May 2015.
- [38] T. Suzuki, D. F. Measday, and J. P. Roalsvig. Total nuclear capture rates for negative muons. *Phys. Rev. C*, 35:2212–2224, Jun 1987.
- [39] Cesare Chiccoli, Y S Melezhik, Paolo Pasini, L I Ponomarev, Wozniakd , and Vladimir Korobov. The atlas of the cross-sections of mesic atomic processes. part iii: The processes $p\mu + (d,t)$, $d\mu + (p,t)$, $t\mu + (p,d)$. 7:87–153, 08 1992.
- [40] T. P. Gorringer and D. W. Hertzog. Precision Muon Physics. *Prog. Part. Nucl. Phys.*, 84:73–123, 2015.
- [41] Jeffrey M. Berryman, André de Gouvêa, Kevin J. Kelly, and Andrew Kobach. Lepton-number-violating searches for muon to positron conversion. *Phys. Rev.*, D95(11):115010, 2017.
- [42] I. Beltrami et al. New Precision Measurements of the Muonic 3-*D* (5/2) - 2*p* (3/2) X-ray Transition in ^{24}Mg and ^{28}Si : Vacuum Polarization Test and Search for Muon - Hadron Interactions Beyond QED. *Nucl. Phys.*, A451:679–700, 1986.
- [43] W. Liu, M. G. Boshier, S. Dhawan, O. van Dyck, P. Egan, X. Fei, M. Grosse Perdekamp, V. W. Hughes, M. Janousch, K. Jungmann, D. Kawall, F. G. Mariam, C. Pillai, R. Prigl, G. zu Putlitz, I. Reinhard, W. Schwarz, P. A. Thompson, and K. A. Woodle. High precision measurements of the ground state hyperfine structure interval of muonium and of the muon magnetic moment. *Phys. Rev. Lett.*, 82:711–714, Jan 1999.
- [44] Peter J. Mohr, Barry N. Taylor, and David B. Newell. CODATA recommended values of the fundamental physical constants: 2010. *Rev. Mod. Phys.*, 84:1527–1605, Nov 2012.

- [45] V. Tishchenko, S. Battu, R. M. Carey, D. B. Chitwood, J. Crnkovic, P. T. Debevec, S. Dhamija, W. Earle, A. Gafarov, K. Giovanetti, T. P. Gorringer, F. E. Gray, Z. Hartwig, D. W. Hertzog, B. Johnson, P. Kammel, B. Kiburg, S. Kizilgul, J. Kunkle, B. Lauss, I. Logashenko, K. R. Lynch, R. McNabb, J. P. Miller, F. Mulhauser, C. J. G. Onderwater, Q. Peng, J. Phillips, S. Rath, B. L. Roberts, D. M. Webber, P. Winter, and B. Wolfe. Detailed report of the mulan measurement of the positive muon lifetime and determination of the fermi constant. *Phys. Rev. D*, 87:052003, Mar 2013.
- [46] V. A. Andreev, T. I. Banks, R. M. Carey, T. A. Case, S. M. Clayton, K. M. Crowe, J. Deutsch, J. Egger, S. J. Freedman, V. A. Ganzha, T. Gorringer, F. E. Gray, D. W. Hertzog, M. Hildebrandt, P. Kammel, B. Kiburg, S. Knaack, P. A. Kravtsov, A. G. Krivshich, B. Lauss, K. R. Lynch, E. M. Maev, O. E. Maev, F. Mulhauser, C. Petitjean, G. E. Petrov, R. Prieels, G. N. Schapkin, G. G. Semenchuk, M. A. Soroka, V. Tishchenko, A. A. Vasilyev, A. A. Vorobyov, M. E. Vznuzdaev, and P. Winter. Measurement of muon capture on the proton to 1determination of the pseudoscalar coupling g_P . *Phys. Rev. Lett.*, 110:012504, Jan 2013.
- [47] K.A. Olive and Particle Data Group. Review of particle physics. *Chinese Physics C*, 38(9):090001, 2014.
- [48] P. H. Fowler and D. H. Perkins. The Possibility of Therapeutic Applications of Beams of Negative π -Mesons. *Nature*, 189:524–528, February 1961.
- [49] V. R. Akylas and P. Vogel. Cascade depolarization of the negative muons. *Hyperfine Interactions*, 3(1):77–85, Jan 1977.
- [50] E. Fermi and E. Teller. The capture of negative mesotrons in matter. *Phys. Rev.*, 72:399–408, Sep 1947.
- [51] Robert W Huff. Decay rate of bound muons. *Annals of Physics*, 16(2):288 – 317, 1961.
- [52] I M Blair, H Muirhead, T Woodhead, and J N Woulds. The effect of atomic binding on the decay rate of negative muons. *Proceedings of the Physical Society*, 80(4):938, 1962.
- [53] H. Primakoff. Theory of muon capture. *Rev. Mod. Phys.*, 31:802–822, 1959.
- [54] B. Goulard, G. Goulard, and H. Primakoff. Relativistic corrections in the theory of muon capture. *Phys. Rev.*, 133:B186–B190, Jan 1964.
- [55] R.C. Cohen, S. Devons, and A.D. Kanaris. Muon capture in oxygen. *Nuclear Physics*, 57:255 – 270, 1964.
- [56] L. Schellenberg, A. Adamczak, R. Jacot-Guillarmod, F. Mulhauser, C. Piller, L. A. Schaller, H. Schneuwly, Y. A. Thalmann, S. Tresch, and A. Werthmüller. Muon transfer to light atoms. *Hyperfine Interactions*, 101(1):215–220, Dec 1996.

- [57] A. Adamczak, D. Bakalov, K. Bakalova, E. Polacco, and C. Rizzo. On the use of a $\text{H}_2\text{-O}_2$ gas target in muonic hydrogen atom hyperfine splitting experiments. *Hyperfine Interactions*, 136(1):1–7, Mar 2001.
- [58] H. Nishino et al. Search for Proton Decay via $p \rightarrow e + \pi^0$ and $p \rightarrow \mu + \pi^0$ in a Large Water Cherenkov Detector. *Phys. Rev. Lett.*, 102:141801, 2009.
- [59] S. N. Ahmed et al. Constraints on nucleon decay via 'invisible' modes from the Sudbury Neutrino Observatory. *Phys. Rev. Lett.*, 92:102004, 2004.
- [60] Gerald A. Miller. Non-Spherical Shapes of the Proton: Existence, Measurement and Computation. *Nucl. Phys. News*, 18:12–16, 2008.
- [61] E. E. Chambers and R. Hofstadter. Structure of the proton. *Phys. Rev.*, 103:1454–1463, Sep 1956.
- [62] Aldo Antognini. The lamb shift experiment in muonic hydrogen. December 2005.
- [63] A. Antognini. Muonic atoms and the nuclear structure. *ArXiv e-prints*, December 2015.
- [64] A. C. Zemach. Proton structure and the hyperfine shift in hydrogen. *Phys. Rev.*, 104:1771–1781, Dec 1956.
- [65] J. C. Bernauer, P. Achenbach, C. Ayerbe Gayoso, R. Böhm, D. Bosnar, L. Debenjak, M. O. Distler, L. Doria, A. Esser, H. Fonvieille, J. M. Friedrich, J. Friedrich, M. Gómez Rodríguez de la Paz, M. Makek, H. Merkel, D. G. Middleton, U. Müller, L. Nungesser, J. Pochodzalla, M. Potokar, S. Sánchez Majos, B. S. Schlimme, S. Širca, Th. Walcher, and M. Weinriefer. High-precision determination of the electric and magnetic form factors of the proton. *Phys. Rev. Lett.*, 105:242001, Dec 2010.
- [66] X. Zhan et al. High-Precision Measurement of the Proton Elastic Form Factor Ratio $\mu_p G_E/G_M$ at low Q^2 . *Phys. Lett.*, B705:59–64, 2011.
- [67] M. A. Belushkin, H.-W. Hammer, and Ulf-G. Meißner. Dispersion analysis of the nucleon form factors including meson continua. *Phys. Rev. C*, 75:035202, Mar 2007.
- [68] I. T. Lorenz, H. W. Hammer, and Ulf-G. Meißner. The size of the proton: Closing in on the radius puzzle. *The European Physical Journal A*, 48(11):151, Nov 2012.
- [69] Randolph Pohl, Herbert Daniel, F. Joachim Hartmann, Peter Hauser, Franz Kottmann, Valery E. Markushin, Markus Mühlbauer, Claude Petitjean, Wolfgang Schott, David Taqqu, and Peter Wojciechowski-Grosshauser. Observation of long-lived muonic hydrogen in the $2s$ state. *Phys. Rev. Lett.*, 97:193402, Nov 2006.

- [70] Aldo Antognini, François Nez, Karsten Schuhmann, Fernando D. Amaro, François Biraben, João M. R. Cardoso, Daniel S. Covita, Andreas Dax, Satish Dhawan, Marc Diepold, Luis M. P. Fernandes, Adolf Giesen, Andrea L. Gouvea, Thomas Graf, Theodor W. Hänsch, Paul Indelicato, Lucile Julien, Cheng-Yang Kao, Paul Knowles, Franz Kottmann, Eric-Olivier Le Bigot, Yi-Wei Liu, José A. M. Lopes, Livia Ludhova, Cristina M. B. Monteiro, Françoise Mulhauser, Tobias Nebel, Paul Rabinowitz, Joaquim M. F. dos Santos, Lukas A. Schaller, Catherine Schwob, David Taqqu, João F. C. A. Veloso, Jan Vogelsang, and Randolph Pohl. Proton structure from the measurement of 2s-2p transition frequencies of muonic hydrogen. *Science*, 339(6118):417–420, 2013.
- [71] A. Adamczak, C. Chiccoli, V.I. Korobov, V.S. Melezhik, P. Pasini, L.I. Ponomarev, and J. Wozniak. Muon transfer rates in hydrogen isotope mesic atom collisions. *Physics Letters B*, 285(4):319 – 324, 1992.
- [72] Andrzej Adamczak, Dimitar Bakalov, Lyubomir Stoychev, and Andrea Vacchi. Hyperfine spectroscopy of muonic hydrogen and the psi lamb shift experiment. *Nuclear Instruments and Methods in Physics Research Section B: Beam Interactions with Materials and Atoms*, 281:72 – 76, 2012.
- [73] T. Matsuzaki, K. Ishida, K. Nagamine, I. Watanabe, G.H. Eaton, and W.G. Williams. The riken-ral pulsed muon facility. *Nuclear Instruments and Methods in Physics Research Section A: Accelerators, Spectrometers, Detectors and Associated Equipment*, 465(2):365 – 383, 2001.
- [74] C. Patrignani et al. Review of Particle Physics. *Chin. Phys.*, C40(10):100001, 2016.
- [75] Marvin J Weber. Inorganic scintillators: today and tomorrow. *Journal of Luminescence*, 100(1):35 – 45, 2002.
- [76] E. V. D. van Loef, P. Dorenbos, C. W. E. van Eijk, K. Krämer, and H. U. Güdel. High-energy-resolution scintillator: Ce³⁺ activated labr₃. *Applied Physics Letters*, 79(10):1573–1575, 2001.
- [77] M. S. Alekhin, J. T. M. de Haas, I. V. Khodyuk, K. W. Krämer, P. R. Menge, V. Ouspenski, and P. Dorenbos. Improvement of γ -ray energy resolution of labr₃:ce³⁺ scintillation detectors by sr²⁺ and ca²⁺ co-doping. *Applied Physics Letters*, 102(16):161915, 2013.
- [78] B.D. Milbrath, B.J. Choate, J.E. Fast, Richard Kouzes, and J.E. Schweppe. Comparison of labr/sub 3/:ce and nai(tl) scintillators for radio-isotope identification devices, 11 2005.
- [79] C. Fiorini, A. Gola, M. Zanchi, A. Longoni, P. Lechner, H. Soltau, and L. Struder. Gamma-ray spectroscopy with labr/sub 3/:ce scintillator readout by a silicon drift detector. In *IEEE Nuclear Science Symposium Conference Record, 2005*, volume 1, pages 230–234, Oct 2005.

- [80] S. Tokar, I. E. Chirikov-Zorin, I. Sykora, and M. Pikna. Single Photoelectron Spectra Analysis for the Metal Dynode Photomultiplier. 1999.
- [81] R11265U SERIES/H11934 SERIES, Hamamatsu PMT DATASHEET. https://www.hamamatsu.com/resources/pdf/etd/R11265U_H11934_TPMH1336E.pdf.
- [82] G. Baldazzi, A. Vacchi, C. Labanti, G. Morgante, F. Fuschino, L.P. Rignanese, P.L. Rossi, E. Mocchiutti, N. Zampa, G. Zampa, A. Rachevski, E. Vallazza, I. D'Antone, M. Zuffa, S. Meneghini, A. Margotti, and M. Furini. The labr 3 (ce) based detection system for the famu experiment. *Journal of Instrumentation*, 12(03):C03067, 2017.
- [83] Jirong Cang, Tao Xue, Ming Zeng, Zhi Zeng, Hao Ma, Jianping Cheng, and Yinong Liu. Optimal Design of Waveform Digitisers for Both Energy Resolution and Pulse Shape Discrimination. *Nucl. Instrum. Meth.*, A888:96–102, 2018.
- [84] Lanthanum Bromide product page. <https://www.crystals.saint-gobain.com/products/standard-and-enhanced-lanthanum-bromide>.
- [85] Walt Kester. Understand SINAD, ENOB, SNR, THD, THD + N, and SFDR so You Don't Get Lost in the Noise Floor. <https://www.analog.com/media/en/training-seminars/tutorials/MT-003.pdf>, 2009.
- [86] Valentin T. Jordanov and Glenn F. Knoll. Digital synthesis of pulse shapes in real time for high resolution radiation spectroscopy. 345:337–345, 06 1994.
- [87] G. AnilKumar, S. L. Sharma, D. C. Biswas, and R. K. Choudhury. Elimination of ballistic deficits for ionization chamber pulses by using trapezoidal pulse shaper. In *2006 IEEE Nuclear Science Symposium Conference Record*, volume 2, pages 1044–1047, Oct 2006.
- [88] Private communication with Dimitar Bakalov.